

QUANTUM DOTS AND ANDREEV REFLECTIONS IN GRAPHENE

QUANTUM DOTS AND ANDREEV REFLECTIONS IN GRAPHENE

Proefschrift

ter verkrijging van de graad van doctor
aan de Technische Universiteit Delft,
op gezag van de Rector Magnificus prof. ir. K. C. A. M. Luyben,
voorzitter van het College voor Promoties,
in het openbaar te verdedigen
op woensdag 22 september 2010 om 10:00 uur

door

Xing Lan LIU

doctorandus in de natuurkunde
geboren te Gansu, China.

Dit proefschrift is goedgekeurd door de promotor:

Prof. dr. ir. L. M. K. Vandersypen

Samenstelling van de promotiecommissie:

Rector Magnificus	voorzitter
Prof. dr. ir. L. M. K. Vandersypen	Technische Universiteit Delft, promotor
Prof. dr. V. I. Falko	Lancaster University
Prof. dr. ir. A. Morpurgo	University of Geneva
Prof. dr. ir. B. J. van Wees	Rijksuniversiteit Groningen
Prof. dr. ir. J. C. Maan	Radboud University Nijmegen
Prof. dr. ir. T. M. Klapwijk	Technische Universiteit Delft
Dr. Y. M. Blanter	Technische Universiteit Delft
Prof. dr. ir. J. E. Mooij	Technische Universiteit Delft (reservelid)



Keywords: nano-devices, graphene, mesoscopic physics, quantum dots, double quantum dots, Andreev reflection, quantum Hall effect

Printed by: Gildeprint Drukkerijen, Enschede, The Netherlands

Cover design: Kateryna Naumova, <http://naumova.net/>

Copyright © 2010 by X. L. Liu

Casimir PhD Series, Delft-Leiden, 2010-20

ISBN 978-90-8593-084-6

An electronic version of this dissertation is available at
<http://repository.tudelft.nl/>.

Preface

By the end of my Master's thesis in University of Groningen in 2006, I was convinced that I wanted to do a PhD working on cold atoms. However, Marius Costache, who was at that moment a PhD student in Groningen, urged me to apply also to the quantum transport group (QT) in Delft. So I did. During my interview in Delft, QT people impressed me for being exceptionally smart and at the same time extremely comfortable. It immediately occurred to me then that it doesn't matter too much what kind of system a research group is working on, but it is more interesting to be able to work with good people. I am grateful to my supervisor Lieven Vandersypen who decided to give me the opportunity to work on my thesis in QT.

The subject of my PhD thesis is to study graphene. When I started my PhD in 2006, it was a freshly discovered wonder material whose fame was just on the rise. There existed only three experimental papers on graphene at that moment, and every week a few theoretical papers would appear on the arXiv. Later on the number of papers increased rather quickly, as more and more research groups joined the race. Thanks to these collective efforts, more and more properties of this new material were quickly revealed. With the new knowledge that we have now, several old publications turn out to be presenting some interpretations which are rather naïve. These include some of our own work. I apologize that while writing this thesis, time didn't allow me to update all our "old" results with the new insight.

On the other hand, to make mistakes and then to correct for them are perhaps the natural course for learning. It is very interesting for me to be able to actually experience it fully within the short four years of time during my PhD. Especially, I'm grateful that I experienced it together with many other people from the graphene team in Delft. First, I would like to thank my PhD supervisor Lieven Vandersypen for giving me the opportunity, and for being the most listening supervisor ever. Your lectures on quantum information are also very well tailored and illuminating. I wish all scientists would teach quantum mechanics as good as you did. I'm also lucky to have the chance to work closely with Alberto Morpurgo during the first two years of my PhD, and with Teun Klappwijk during the last year of my PhD. Alberto impresses as well as depresses me for be-

ing always able to come up with simple explanations to our used-to-be-puzzling data. The thing is that, once Alberto pointed it out, the explanations will appear to be simply straightforward and I couldn't help wondering why I didn't see it. Although, surely it needs years of preparation in order to gain such an ability, I'm glad that I probably have learned a tiny bit in the end. Teun is almost an encyclopedia for superconductivity in practical materials. Thanks a lot for your help with my thesis, and for being always extremely patient, tolerant, and considerate during all our discussions.

In the beginning of my PhD, I had the luxury to be introduced to the clean-room by Pablo *de Hero*, who went to the cleanroom nearly everyday even during the last few days of his stay in QT. Pablo, I still remember my genuine panic when you were leaving QT after the first two-month of my stay. And you said, it will be fine. And you were right. Curious enough, whenever I'm at the wetbench, working or training others, I still hear you talking, "take the bottle with two hands", for instance. Hubert, thanks for introducing me to QT and for your help with the "diamond". Jeroen, congratulations with your very nice thesis. You know, you "scooped" me with the thesis title :) Dominique, I enjoyed very much our time together in the lab and I also learned really a lot from you. Do you still remember your "wine-bottle" flake? I'm also very happy to have had the chance to guide and to learn from two excellent BEP students Bart and Bas during the first two years of my PhD.

After Alberto's group moved to Geneva, Stijn, Amelia, and Victor joined the graphene team in Delft. Amelia, I'm feeling really lucky to have met you. Among many other things, you "glued" the graphene people together and made us into a team as soon as you joined! I'm sorry about the weather in Delft. I sincerely wish you best of luck with everything (and I'm sure that you will have it, since "chance favors the prepared mind"). Stijn, you are forever patient, relaxed, and helpful... a truly amazing person. Looking forward to hearing about your bilayer dots! And Victor, although you just started your PhD, you already have a wealth of research experience with many people. Hope one day you will really have a ride in Kostya's sports car ;) Many students also made indispensable contributions to the team, Dorothée, Tungky, Angelo, Chris, Maaïke, and Annemarie. Special thanks to Dorothée and Chris. Dorothee, it was a pleasure to know you. With work, you strike me with your ambition and determination. Outside work, I enjoyed the beers and billiards, too. Chris, thanks a lot for your help with everything! In your way, you made it very comfortable for people around you. Best of luck with your thesis! Special thanks to Anton Akhmerov for many inspiring ideas as well as for being forever patient and helpful with my many stupid questions.

I'm in debt to the wires and tubes team, Floris *Freetibet Fighter*, Georg, Juriaan, Stevan *Nijntje*, Maarten, Sergey, Gary, Han, and many others. Thanks a lot for your helps, especially during my g1 period. Floris, apart from the well known bluntness, you are very helpful too. Thanks for teaching me many little tricks on measuring diamonds and writing papers. Also I appreciate it that you frankly told me to be worried long time ago. It took me more than one year to get to be worried though. Juriaan and Han, thanks

for your help with the Heliox! Juriaan, I'm still in doubt, perhaps you actually indeed knocked your finger to straight with a hammer... Georg, in reply to your comments on Chinese food, you are welcome and I don't like it so much either :) Gary, thanks for the discussions about physics, fabrications, as well as other stuffs. Also thank you and Susan for the parties in Dublin! Sergey, it is fun working with you, although a bit too short. I'm curious how it is possible to integrate in one person all the qualities such as funny, modest, smart, considerate, helpful, comfortable... Stevan, "how is it going" :) let's say that you seem to have the most balanced character ever, and have some sort of composure that I would never achieve even if I would spend all my lifetime pursuing it. So I won't I think. Maarten, it is a happy story to share an office with you for four years. Lately my level of digesting jokes has degraded significantly. Thomas, you are one of the few experimentalists who value the solving of integrals. Lars, I enjoyed very much our time at Nijenrode. Maarten vW, I'm very impressed by your thesis and the defence. Best wishes for the future! Gijs and Toeno, you laid foundations for the envious and fun diamonds team, perhaps the only team in QT that can possibly compete with our graphene team.

I'm grateful to many other QT members as well. Hans and Leo, thanks for making QT how it is. One can perhaps always argue whether it's a good thing or a bad thing, but I enjoyed it very much. So thanks. Of course every QT-er contributes it, but you choose the QT-ers. Kees, I felt rather "thrilled" to met you, the author of my favourite text book, *Mesoscopic Physics, an Introduction*. Val, thanks for organizing the collaboration with Ethan and for your kind accommodation in the beginning of my PhD. Ad, best of luck with the superconducting wires! Enough is said by everybody about Raymond's importance in QT and his magic power. I wonder how you could survive all the compliments and remain modest. Many thanks for your help! Bram, being perhaps the only openly cynical person in QT, actually brings some humanity and warmth around I think. Thanks for your help with nearly everything. I'm especially grateful to your comments "be yourself". Remco, how did you know that I studied German at school? (No, I didn't.) Guten tag and auf wiedersehen! Angèle and Yuki, thanks for your ceaseless efforts in making our life easy in QT, as well as in the Netherlands.

I also spent quite a lot of time in the MED lab during my PhD. Many thanks to Edgar, Samir, Christian, Andreas, and Menno for making it so much fun! Edgar, also thanks for showing me how to cool down a fridge... Samir, the last week in Dimes was fun :) Menno, thanks also for your help with \LaTeX !

One thing that I enjoyed very much of my PhD is to be able to actually make something. This wouldn't have happened without the constant support from everybody working in the cleanroom, Arnold, Anja, Marco, Roel, Marc and many others. Marco, what motivates you to be a workaholic? And Marc, once you pulled out from the top of your head a dry-etching recipe and it immediately worked for my devices! Thanks a lot.

Many people helped me directly with the writing, discussions, and printing of this thesis and propositions. Floris, Fabian, Chris, Stijn, Umberto, Amelia, Victor, Pol, Thomas,

Juriaan, Jeroen, Wolfgang, Liz, Elissa, and many others, thanks a lot for your time! And special thanks to Katya for designing the awesome, extravagant cover!

During my PhD, I had the chance to attend many conferences and to visit a few other labs. Special thanks to Klaus Ensslin for giving me the opportunity to visit his lab. Many thanks to Françoise, Susanne, Johannes and Stephan for the excellent time in the yearly graphene conferences and for the hospitality in Zürich. It is great to have you as competitors! I am grateful to Philip Kim and his group for showing me the lab and the inspiring discussions as well.

I owe my gratitude to the friends from the nano-science group in University of Groningen, who planted the idea of being a physicist in me :) Anne, thanks for being nearly always positive and encouraging. I'm happy that you can be my paranymph. Bram, I still remember the fun and frustration in the optics lab with you. Congratulations with your nice paper! Michiel, I heard you are the master of all lasers in the lab? Auke and Ponky, best wishes for finishing your thesis as well.

Despite the distance, I'm glad to be able to keep up with some friends from the school time as well. Li Na, Zhao Ying, and Zhang Jie, I really miss the time we spent together in the dormitory. Hope we could meet again all four of us together... Rao Jie and Sun Yue-Kui, it was fun to meet you again on the flight, as well as in the Netherlands and in China. I'm sorry for my cowardly giving up of academia though... Niu Wen Jie, really happy to be in touch with you again. Hope to see you soon in Shang-Hai!

Delft is not only a great place for work, I also enjoyed living here. With Xu Qiang, Xiao-Li, Chen Ping, Li Zhen, Gao Bo, Huang Zhuang-Xiong, CK, Xie Hang-Xing, and Song Bo, I enjoyed the evenings we spent together going to the many Chinese restaurants. Thanks to Katja, Iwijn, Christine, Edgar, Liz, Jan, Juan and many others for the many "Wednesday diners" and the drinks in Klooster afterwards. I had a good time with the Friday-afternoon soccer team, Ewan, Marco, Georg, Floor, Tomoko, Pol, Yvonne, and many others. I know I don't really play football, but it feels great after running around the field for two hours :) With the "skippl", Stijn, Basia, Alina, Fabian, Salvo, Floris, and Hannes, I enjoyed very much our ski trip and the numerous après-ski parties together. Basia, I think I have seen a real you after the vodkas :) Alina, we know each other for almost as long as I'm in the Netherlands. Thanks for your enthusiasm and warmth. Salvo, you brought so much fun to us during your very short stay in QT. Looking forward to seeing you all again for our upcoming Sicily trip.

Special thanks to my housemates, Pol, Umberto, and Katja / Hannes, from the *pluk*-house to *pluh*-house. Going through four years and one month together, I really don't know what to say here. In 2006 when I just moved to Delft, I guess I was just glad to have found a shelter, and god how much it is beyond a shelter! Pol, I'm impressed by your enthusiasm and perseverance. Umberto, it took me at least half a year to get to know you. It is amazing how much we are alike and unlike. Yet, you are an incredibly open and honest person, which makes you a truly valuable friend. Katja, many thanks for introducing me to life in QT and in Delft. You are probably the most responsible and

reliable person in the house. Hannes, it was fun to have you in the house! I still feel that we didn't have enough chances to talk and still wish to have the serious conversation about China with you. I also enjoyed the company of many temporary housemates, Iwijn, Christo, Andres, Greg, and Lukas.

Finally, the magnificent climbing team, Lucio, Lucie, Hannes, Floris, Moïra, Giuseppe, Valentine, Lihn, and Edward. Floris, thanks for introducing me to climbing. I think it helped a lot in supporting me through the last few months of stressful multi-tasking. With Lucio, Floris, and Wolfgang, I also had lots of fun with our conversations about nonsense, in which, I believe, lies the true meaning of life ;) Btw, Wolfgang, are you not part of the climbing team? Moïra, you are the most caring person I ever knew. I enjoyed so much of everything. Thanks for being my paranymph as well!

I would like to thank my parents and brother. 爸爸妈妈，感谢你们辛辛苦苦抚养我长大，以及对我无条件的支持。很对不起我这么多年来一直在外。治治，谢谢你代我照顾爸妈。

Special thanks to Maxim, for showing me the entire world, and going through it together with me.

Xing Lan Liu,

柳星兰

August 2010, Delft

Contents

1	Introduction	1
1.1	What's special about graphene	2
1.2	Outline of this thesis	3
	References	4
2	Theoretical aspects	7
2.1	Bandstructure of graphene	7
2.1.1	Tight binding approach for monolayer graphene	7
2.1.2	The Dirac equation for monolayer graphene	10
2.1.3	The band structure of bilayer graphene	12
2.2	Landau levels and quantum Hall effect in graphene	14
2.2.1	Monolayer graphene	14
2.2.2	Bilayer graphene	15
2.3	Graphene nanoribbons	16
2.3.1	Band structure of graphene nanoribbons with perfect edges	16
2.3.2	Effect of edge roughness on graphene nanoribbons	18
2.4	Quantum dots	19
2.4.1	The constant interaction model of a single quantum dot	19
2.4.2	Double quantum dots	23
2.5	Andreev reflection in the quantum Hall regime	25
2.5.1	Andreev reflection	25
2.5.2	Andreev reflection in high magnetic field	27
	References	29
3	Fabrication	35
3.1	Fabricating graphene with mechanical exfoliation	35
3.2	Graphene nanoribbon	39
3.3	Top gates	41
	References	43

4	Gate induced insulating state in bilayer graphene devices	45
4.1	Introduction	46
4.2	The low-energy bandstructure of single- and bilayer graphene	46
4.3	Fabrication of double-gated graphene devices	48
4.4	Characterization of single-layer and bilayer graphene devices	49
4.5	Transport in the insulating regime	51
4.6	Conclusions and discussion	55
	References	56
5	Coulomb blockade in top-gated graphene nanoribbons	59
5.1	Background and introduction	60
5.2	Device fabrication and characterizations	61
5.3	Coulomb blockade in the npn regime	63
5.4	Coulomb blockade in the $pp'p$ regime	67
5.5	Multiple dots behaviour	70
5.6	Coulomb blockade within the transport gap	71
5.7	Conclusions	73
5.8	Additional information	73
5.8.1	Estimate level spacing	73
5.8.2	Statistics of peak spacings	75
5.8.3	Coulomb staircase	76
	References	76
6	Gate-defined graphene double quantum dot and excited state spectroscopy	81
6.1	Motivations and introduction	82
6.2	Device fabrications and measurement setup	82
6.3	Characterization of the top gates	83
6.4	Top-gated double quantum dot in a graphene nanoribbon	85
6.5	Resonant transport through excited states of the double quantum dot	87
6.6	Tuning the inter-dot coupling and the effects of disorder	89
6.7	Form a single dot along the graphene nanoribbon	91
6.8	Conclusions	92
6.9	Additional information	93
6.9.1	Charge stability diagram of the double dot in different configurations	93
6.9.2	Estimates of the level spacing	94
	References	95
7	Quantum Hall effect in graphene Josephson junctions	99
7.1	Introduction	100
7.2	Fabrication and device characterization	101
7.3	Josephson junctions in graphene	104
7.4	Two terminal quantum Hall effect in the presence of superconductors	106

7.5	Quantum Hall fluctuations	109
7.6	Summary and outlook	113
	References	113
8	Conclusions and outlook	119
8.1	Current status	119
8.1.1	Band gap engineering and quantum dots on graphene	119
8.1.2	Andreev reflections and quantum Hall effect on graphene	120
8.2	Future experiments	120
8.2.1	Improving the mobility	120
8.2.2	Quantum dots in bilayer graphene	121
8.2.3	Cooper pair detection using spin valves	121
8.2.4	Hybrid systems of graphene nanoribbon and nanowires	122
	References	124
	Appendix	127
A	Useful numbers and relations in graphene	127
B	Estimate of level spacing in graphene dots	129
	References	130
C	A cleaning recipe for Si/SiO₂ wafers	131
	Summary	133
	Samenvatting	135
	Curriculum Vitae	137
	List of Publications	139

Chapter 1

Introduction

*If you can look into the seeds of time,
and say which grain will grow and which will not,
speak then to me.*

Shakespeare, MacBeth

Graphene is a single atomic layer of graphite. It was commonly referred to as the building block of other carbon allotropes such as carbon nanotube and graphite, before it became a subject itself. Graphene was not known to exist in an isolated form until 2004-2005 when two research groups reported transport measurements on graphene [1–3]. Graphene is "discovered" much later than the other carbon allotropes perhaps because the melting point of two dimensional (2D) solids is theoretically predicted to be at zero temperature according to thermodynamics. (The average vibration amplitude diverges logarithmically at any finite temperature for a 2D crystal, whereas it is convergent at any temperature for the 3D case [4].)

Nevertheless, graphene was proven to exist after all, on substrate [5], or free-standing [6]. It remains a mystery for me how some physicist would one day come up with an idea of working on producing a material that is not supposed to exist. In any case, it is a brilliant idea now that it turns out to be possible, thanks to the courage and perseverance of the pioneers.

Ever since its birth in a laboratory, graphene has attracted considerable attention world wide, especially within the scientific community. The interests in this new material are perhaps partially induced by its readiness in production, but are mostly due to various truly unique properties of graphene, as discussed extensively in many reviews (e.g. ref. [7]). Below we focus on some of its electronic properties.

1.1 What's special about graphene

Two of the most extraordinary properties of graphene are its absolute two-dimensionality and its Dirac particles. The conducting electrons moving in the honeycomb lattice of graphene are described by the Dirac equation [8, 9] rather than the usual Schrödinger's equation. As a result, many well known effects in the field of solid state physics are expected to be modified [7].

One such example is the unconventional *half-integer* quantum Hall effect in graphene, which is experimentally verified immediately after its discovery [2, 3]. In a perpendicular magnetic field, electrons in conventional two-dimensional electron gas (2DEG) systems are quantized in equidistant Landau levels, leading to the celebrated the quantum Hall effect [10]. The Dirac electrons in graphene are also quantized in Landau levels when subjected to a perpendicular magnetic field. However, the Landau levels are not equally spaced, but follow a square root dependence on the magnetic field. Most interesting of all, there is a zero energy Landau level. As a result, the Hall conductance in graphene is quantized in values that are half-integer multiples of $4e^2/h$, i.e. $\pm 2e^2/h$, $\pm 6e^2/h$, $\pm 10e^2/h$, etc. Remarkably, quantum Hall effect is observed in graphene even at room temperature [11].

Another consequence of the Dirac equation is the Klein tunneling, where an electron can tunnel through a high potential barrier with nearly 100% probability [12]. This prediction is also experimentally verified using devices with $p-n$ junctions in graphene [13, 14].

Two-dimensional electronic systems are of great interest to many researchers. Conventional 2DEG systems typically consist of electrons confined in a potential well of a few nanometers thick such that the motions in the third dimension are quantized. The electrons behave as two-dimensional at low temperatures where only one electronic sub-band is occupied.

The electrons in graphene are however naturally two-dimensional, and remain so at room temperature or even higher. This remarkable two-dimensionality is very appealing. One interesting experiment that makes use of the thinness of graphene is perhaps the observation of the Zeeman splitting in graphene from the measurements on universal conductance fluctuations [15]. In addition to potential new physics, the two-dimensionality also allows one to conveniently build more complex device architectures on graphene, in contrast to one-dimensional systems. For instance, an elegant design of a single electron transistor on graphene has been demonstrated, where the central island, the source / drain contacts, and several control gates are all made of graphene [16].

In addition, many properties which make carbon nanotubes special are also present in graphene. It is therefore natural to follow the footsteps of the research works on nanotubes in searching for novel physics as well as applications. For instance, the spin coherence time in carbon nanotubes or graphene is expected to be much longer

than that in GaAs 2DEG systems, due to the absence of hyperfine interaction and s / spin-orbit interactions, making both materials promising candidates for building spin-qubits [17, 18].

Thanks to such unique properties, many research groups world wide have dived into the study of graphene since its discovery. In the field of mesoscopic physics for instance, many phenomena have already been reproduced in this new material within a very short time span thanks to the collective efforts. The examples include the quantum Hall effect as already mentioned earlier, weak localization [19], universal conductance fluctuations [15, 20], Aharonov Bohm effect [21, 22], Josephson effects [20, 23], and Coulomb blockade [16].

Along the way, more convenient aspects of graphene are revealed. For example, graphene is friendly to many imaging techniques [24–26] as it is usually lying directly on a surface and is readily accessible. Being a highly conductive material that is extremely thin, graphene is also an attractive candidate for applications that require transparent and flexible electrodes [27]. This list continues.

In summary, several special properties of the new material graphene as well as the related new physics or applications are reviewed. Graphene has genuinely generated a hype since its birth in a laboratory, and will continue to inspire new ideas, from the perspective of both the fundamental research and applications.

1.2 Outline of this thesis

The experiments that are described in this thesis are all performed on graphene. Chapter 2 describes the theoretical background that is most relevant to the contents of this thesis.

In chapter 3, I summarize several major nano-fabrication techniques used in making the devices described in this thesis. The contents focus on general concerns of each technique rather than the detailed fabrication recipes.

The main focus of the experimental work described in this thesis is on device applications. Graphene is a promising material for many purposes, but the main challenge in this respect is that it has zero band gap. We research on two ways of band gap engineering in graphene.

First, in bilayer graphene, we expect a band gap if the top and bottom layers are at a different potential. In chapter 4, we use a top gate and a back gate to create the asymmetric potential for the top and bottom layers of a bilayer graphene sample. We observe insulating behavior of the conductance in the bilayer device at nonzero perpendicular electric fields. The observed gap is however very small, limited by the small electric field that we can apply in our devices, as well as localized mid-gap states in the gap.

Second, an energy gap is expected in graphene nanoribbons. A nanoribbon is a quasi one-dimensional system etched into the 2D graphene sheet, where the confinement opens a band gap. Then quantum dots are defined on the nano-ribbons by local

gates. In such devices, we could form a single quantum dot (chapter 5) and a double quantum dot (chapter 6) using local top gates. The device properties are severely limited by strong disorder.

We then proceed to a third experiment that is more focused on the fundamental aspects, where we wish to study Andreev reflections in the quantum Hall regime in graphene. Graphene makes good electric contact to some superconducting materials thanks to the absence of the band gap and thereby Schottky barrier. At the same time, graphene shows quantum Hall effect. In chapter 7, we combine these two advantages and fabricated Josephson junctions on graphene using a high H_{c2} superconductor as the contacts. We further study the quantum Hall effect in these graphene Josephson junction devices.

References

- [1] K. S. Novoselov, A. K. Geim, S. V. Morozov, D. Jiang, Y. Zhang, S. V. Dubonos, I. V. Grigorieva, and A. A. Firsov, *Electric Field Effect in Atomically Thin Carbon Films*, *Science* **306**, 666 (2004).
- [2] K. S. Novoselov, A. K. Geim, S. V. Morozov, D. Jiang, M. I. Katsnelson, I. V. Grigorieva, S. V. Dubonos, and A. A. Firsov, *Two-dimensional gas of massless Dirac fermions in graphene*, *Nature* **438**, 197 (2005), ISSN 0028-0836.
- [3] Y. Zhang, Y.-W. Tan, H. L. Stormer, and P. Kim, *Experimental observation of the quantum Hall effect and Berry's phase in graphene*, *Nature* **438**, 201 (2005), ISSN 0028-0836.
- [4] D. Khomskii, *Quantum theory of solids* (2004-2005), lecture notes.
- [5] A. K. Geim and K. S. Novoselov, *The rise of graphene*, *Nature Materials* **6**, 183 (2007), ISSN 1476-1122.
- [6] M. H. Gass, U. Bangert, A. L. Bleloch, P. Wang, R. R. Nair, and A. K. Geim, *Free-standing graphene at atomic resolution*, *Nature Nanotechnology* **3**, 676 (2008), ISSN 1748-3387.
- [7] A. K. Geim, *Graphene: Status and Prospects*, *Science* **324**, 1530 (2009).
- [8] P. R. Wallace, *The Band Theory of Graphite*, *Physical Review Online Archive (Prola)* **71**, 622 (1947).
- [9] A. H. Castro Neto, F. Guinea, N. M. R. Peres, K. S. Novoselov, and A. K. Geim, *The electronic properties of graphene*, *Reviews of Modern Physics* **81**, 109 (2009).

-
- [10] Klitzing, G. Dorda, and M. Pepper, *New Method for High-Accuracy Determination of the Fine-Structure Constant Based on Quantized Hall Resistance*, Physical Review Letters **45**, 494 (1980).
- [11] K. S. Novoselov, Z. Jiang, Y. Zhang, S. V. Morozov, H. L. Stormer, U. Zeitler, J. C. Maan, G. S. Boebinger, P. Kim, and A. K. Geim, *Room-Temperature Quantum Hall Effect in Graphene*, Science **315**, 1379 (2007).
- [12] M. I. Katsnelson, K. S. Novoselov, and A. K. Geim, *Chiral tunnelling and the Klein paradox in graphene*, Nature Physics **2**, 620 (2006), ISSN 1745-2473.
- [13] N. Stander, B. Huard, and D. G. Gordon, *Evidence for Klein Tunneling in Graphene $p-n$ Junctions*, Physical Review Letters **102**, 026807 (2009).
- [14] A. F. Young and P. Kim, *Quantum interference and Klein tunnelling in graphene heterojunctions*, Nature Physics **5**, 222 (2009), ISSN 1745-2473.
- [15] M. B. Lundberg and J. A. Folk, *Spin-resolved quantum interference in graphene*, Nature Physics **5**, 894 (2009), ISSN 1745-2473.
- [16] C. Stampfer, J. Güttinger, F. Molitor, D. Graf, T. Ihn, and K. Ensslin, *Tunable Coulomb blockade in nanostructured graphene*, Appl. Phys. Lett. **92**, 012102 (2008).
- [17] B. Trauzettel, D. V. Bulaev, D. Loss, and G. Burkard, *Spin qubits in graphene quantum dots*, Nature Physics **3**, 192 (2007), ISSN 1745-2473.
- [18] J. Fischer, B. Trauzettel, and D. Loss, *Hyperfine interaction and electron-spin decoherence in graphene and carbon nanotube quantum dots*, Physical Review B **80**, 155401 (2009).
- [19] D. Graf, F. Molitor, T. Ihn, and K. Ensslin, *Phase-coherent transport measured in a side-gated mesoscopic graphite wire*, Physical Review B **75**, 245429 (2007).
- [20] H. B. Heersche, P. Jarillo-Herrero, J. B. Oostinga, L. M. K. Vandersypen, and A. F. Morpurgo, *Bipolar supercurrent in graphene*, Nature **446**, 56 (2007), ISSN 0028-0836.
- [21] S. Russo, J. B. Oostinga, D. Wehenkel, H. B. Heersche, S. S. Sobhani, L. M. K. Vandersypen, and A. F. Morpurgo, *Observation of Aharonov-Bohm conductance oscillations in a graphene ring*, Physical Review B **77**, 085413 (2008).
- [22] M. Huefner, F. Molitor, A. Jacobsen, A. Pioda, C. Stampfer, K. Ensslin, and T. Ihn, *The Aharonov-Bohm effect in a side-gated graphene ring*, New Journal of Physics **12**, 043054 (2010), ISSN 1367-2630.

- [23] X. Du, I. Skachko, and E. Y. Andrei, *Josephson current and multiple Andreev reflections in graphene SNS junctions*, Physical Review B **77**, 184507 (2008).
- [24] J. Martin, N. Akerman, G. Ulbricht, T. Lohmann, J. H. Smet, K. von Klitzing, and A. Yacoby, *Observation of electron-hole puddles in graphene using a scanning single-electron transistor*, Nature Physics **4**, 144 (2007), ISSN 1745-2473.
- [25] J. Martin, N. Akerman, G. Ulbricht, T. Lohmann, K. von Klitzing, J. H. Smet, and A. Yacoby, *The nature of localization in graphene under quantum Hall conditions*, Nature Physics **5**, 669 (2009), ISSN 1745-2473.
- [26] S. Schnez, J. Güttinger, M. Huefner, C. Stampfer, K. Ensslin, and T. Ihn, *Imaging Localized States in Graphene Nanostructures* (2010), [arXiv:1005.2024](https://arxiv.org/abs/1005.2024).
- [27] X. Wang, L. Zhi, and K. Mullen, *Transparent, Conductive Graphene Electrodes for Dye-Sensitized Solar Cells*, Nano Letters **8**, 323 (2008).

Chapter 2

Theoretical aspects

2.1 Bandstructure of graphene

Theoretical work on the band structure of graphene dates back to perhaps year 1946 with P. R. Wallace's work [1], motivated by understanding the properties of graphite. With the discovery of carbon nanotubes [2], followed by the discovery of graphene [3, 4], it continued to receive much attention for decades. In this section we outline briefly the calculation of the band structure of graphene using a nearest neighbour tight-binding approach. The result covers some of the most important properties of graphene. The calculation itself is also a very nice exercise, as a result of the relative simple lattice structure of graphene: 2D, only carbon atoms, only one atomic orbit p_z is needed, etc. It's also more interesting comparing to the trivial case of a 1D atom chain.

Graphene contains a honeycomb lattice of carbon atoms (Fig. 2.1). Each carbon atom has four valence electrons, three of which occupy the three sp^2 hybridization orbitals and form three σ bonds with the three neighbouring carbon atoms. These electrons have very low energy (corresponding to high bond strength) and are localized. They don't contribute to transport. The fourth electron occupies the p_z orbital which is perpendicular to the graphene plane. It overlaps with neighbouring p_z electrons to form π bonds. The p_z electrons have higher energy than the electrons that form the σ bonds, and are delocalized over the entire lattice. They contribute to electronic transport. Below we calculate the band structure considering only these p_z electrons.

2.1.1 Tight binding approach for monolayer graphene

The lattice structure of monolayer graphene is shown in Fig. 2.1. It has a hexagonal lattice as indicated by the lattice vectors \vec{a}_1 and \vec{a}_2 , and there are two atoms per unit cell,

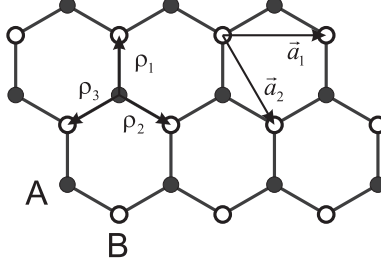


Figure 2.1: Illustration of graphene lattice. The filled and open circles represent the A and B sublattices, respectively. \vec{a}_1 and \vec{a}_2 represent the lattice vectors. The three $\vec{\rho}$ vectors connect one atom to its three nearest neighbouring lattice sites.

A and B . Following numerous earlier works [1, 5, 6], below we summarize the main reasoning and result of the tight-binding calculation for the band structure of monolayer graphene.

The tight binding Hamiltonian with only nearest neighbour hopping can be written as

$$H = -t \sum_{\langle jk \rangle} |j\rangle \langle k|$$

where $t > 0$ is the hopping amplitude, $|j\rangle$ ($|k\rangle$) is an atomic wavefunction centered around atomic sites \vec{r}_j (\vec{r}_k), and $\sum_{\langle jk \rangle}$ sums over all neighbouring sites j and k . The minus sign is because an electron lowers its energy by hopping to neighbouring sites. From the lattice structure of graphene (Fig. 2.1) we note that all atoms from the A sublattice have B atoms as their nearest neighbour. In graphene the hopping integral $t = 3.1$ eV [5].

The solution of this Hamiltonian is a Bloch wave and can be written in terms of sublattice A and B as [1, 6],

$$|\Psi_k\rangle = b_1 \sum_{n \in A} \exp(ik \cdot \vec{R}_n) |n\rangle_A + b_2 \sum_{n \in B} \exp(ik \cdot \vec{R}_n) |n\rangle_B$$

where \vec{R}_n represent lattice vectors, $|n\rangle_A$ ($|n\rangle_B$) are atomic wave functions of A (B) atoms, and \sum_n sums over the entire A or B sublattice.

To solve for the eigenvalues, we project $|\Psi_k\rangle$ to two wavefunctions $|l\rangle_A$ and $|l\rangle_B$ and obtain:

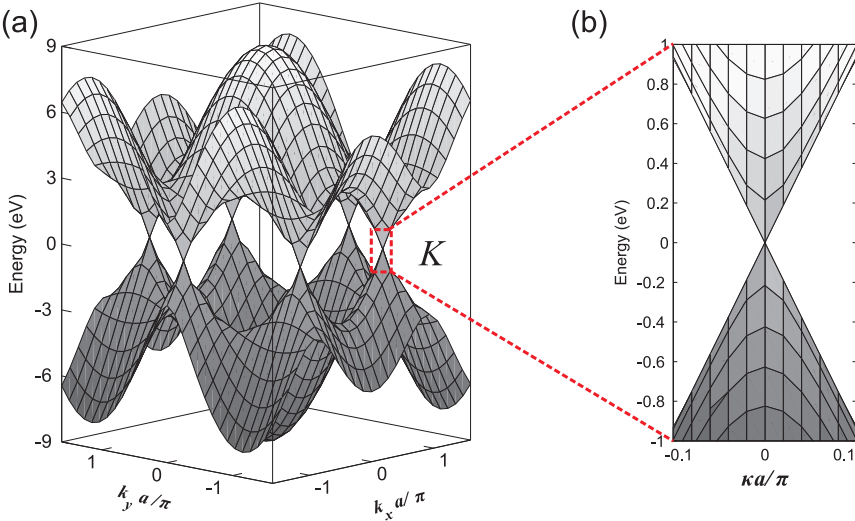


Figure 2.2: (a) The dispersion relation of graphene calculated using nearest neighbour tight binding model (eqn. 2.1). The nearest neighbour hopping integral t is taken to be 3 eV to generate this plot. (b) Zoom in to the low energy part of the dispersion reveals linear relation, as described by eqn. 2.3.

$$\begin{aligned}
 A \langle l | H | \Psi_k \rangle &= -t b_2 \sum_{j=1}^3 \exp(-i k \cdot \rho_j) = b_1 E_k \\
 B \langle l | H | \Psi_k \rangle &= -t b_1 \sum_{j=1}^3 \exp(i k \cdot \rho_j) = b_2 E_k
 \end{aligned}$$

where $\vec{\rho}_i$ are vectors that connect one lattice site to its three neighbouring lattice sites as indicated in Fig. 2.1. The energy dispersion E_k is obtained after eliminating b_1 and b_2 ,

$$E_k = \pm t \left| \sum_{j=1}^3 \exp(i k \cdot \rho_j) \right| \quad (2.1)$$

Fig. 2.2a plots eqn. 2.1. As a result of the two atoms per unit cell, there are two bands, the conduction band and the valence band. The conduction band and valence band touch at six points in the reciprocal lattice, which are commonly referred to as the K points. From Fig. 2.3 we see that the K points coincide with the boundary of the 1st Brillouin zone. Fermi energy lies exactly at the K points for undoped graphene since each atom contributes one electron. The Fermi surface of graphene consists thus of only six points, and we find that graphene is a zero band-gap semiconductor.

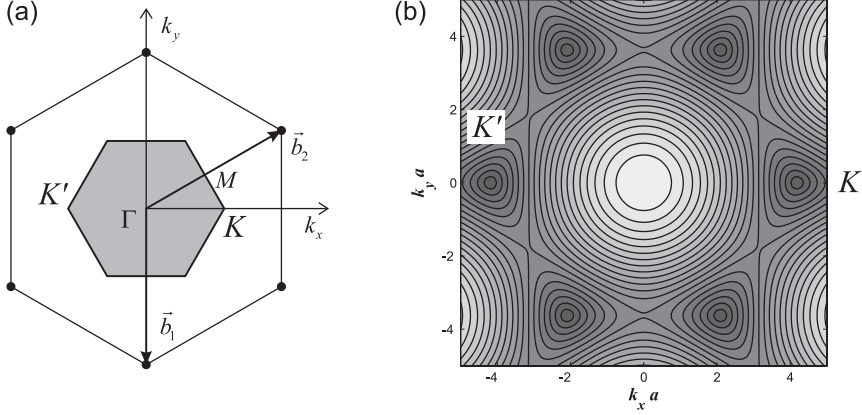


Figure 2.3: (a) Reciprocal lattice of single layer graphene. $\vec{b}_{1,2}$ are reciprocal lattice vectors. The shaded area represents the 1st Brillouin zone. The K and K' points are labeled on the graph. The Γ point (center of the first Brillouin zone) and the M point (center of an edge of the first Brillouin zone) are also labeled. (b) A contour plot representation of Fig. 2.2(a). The K and K' points are also labeled on the graph.

The six points at the Fermi surface are not independent, since every next nearest neighbouring points are related to each other by a reciprocal lattice vector \vec{b} . It thus reduces to only two independent K points: K and $K' = -K$ as indicated in Fig. 2.3a and Fig. 2.3b. The two independent K points or valleys are sometimes referred to as the *iso-spin*. The K and K' points are degenerate, because they are related to each other by time reversal symmetry. This is often referred to as the valley degeneracy.

Another important degeneracy is the electron hole degeneracy at each K point. This is due to the 120° rotation symmetry of graphene lattice [6].

2.1.2 The Dirac equation for monolayer graphene

Most transport properties of a semiconductor or metal are dominated by electrons with an energy around the Fermi level. The dispersion relation of graphene (eqn. 2.1) obtained in the previous subsection can be expanded around one K point (use, for instance, the coordinates $K = (4\pi/3a)\hat{x}$), using

$$\vec{k} = \vec{K} + \vec{\kappa}.$$

Neglecting the second and higher order terms, we obtain the *Dirac equation* for small κ (and small energy):

$$\hbar v_F \vec{\kappa} \cdot \vec{\sigma} |\psi\rangle = \varepsilon |\psi\rangle \quad (2.2)$$

where $v_F \approx 1 \times 10^6$ m/s is the Fermi velocity and $\vec{\sigma}$ are the Pauli matrices. The eigen

values of the Dirac equation are:

$$\varepsilon = \pm \hbar v_F |\kappa| \quad (2.3)$$

The eigen vectors of the Dirac equation 2.2 are linear combinations of the eigen vectors of Pauli matrices σ_x and σ_y . The wave vector $|\psi\rangle = (\psi_A, \psi_B)$ is thus called *pseudo-spin*. These eigen vectors are:

$$|\psi_\kappa\rangle_\pm = \begin{pmatrix} \mp e^{-i\beta/2} \\ e^{i\beta/2} \end{pmatrix}$$

for the K point and

$$|\psi_{\kappa'}\rangle_\pm = \begin{pmatrix} \pm e^{i\beta/2} \\ e^{-i\beta/2} \end{pmatrix}$$

for the K' point, where β is the angle between $\vec{\kappa}$ and \vec{x} axis (i.e. $e^{i\beta} = (\kappa_x + i\kappa_y)/|\kappa|$). Notice that pseudo-spin "up" (down) corresponds to both electrons of the unit cell occupy only the A (B) site, leaving the B (A) site empty. Following eqn. 2.2, we see that the direction of the pseudo-spin is either parallel ($\varepsilon > 0$, for electrons) or anti-parallel ($\varepsilon < 0$, for holes) to the direction of motion $\vec{\kappa}$. For this reason, electrons in graphene are often called "chiral" [7, 8]. Similar to real spin, when β change by 2π , the wavefunctions of the pseudo-spins $|\psi_\kappa\rangle$ reverse sign indicating a phase of π (Berry's phase).

One important implication of the pseudo-spin is the suppression of back-scattering. This can be illustrated after calculating the overlap integrals of different pseudo-spins:

$$\begin{aligned} \pm \langle \psi_{-\kappa} | \psi_\kappa \rangle_\pm &= 0 \\ \pm \langle \psi_{-\kappa'} | \psi_{\kappa'} \rangle_\pm &= 0 \end{aligned}$$

i.e. the elastic scattering processes that flips pseudo-spin (equivalent to scattering from κ to $-\kappa$ state) have zero probability within the same valley. This is the reason for ballistic transport in the one-dimensional metallic carbon nanotubes [9]. Graphene is however not ballistic because scattering can happen in 2D and large angle scattering probabilities are non-zero.

The Dirac equation is extremely important as it is frequently used in calculating the properties of graphene, instead of the tight-binding expression, not only because of its simplicity, but also because it is sufficient in most occasions (exceptions include Andreev reflection [10], scattering at lattice defects, etc.). This is because the scattering process from K to K' (inter-valley scattering) requires change of momentum on the order of the reciprocal lattice vector and is difficult. In other words, short range scatterers on the order of real lattice spacing a are required, which are rare.

Since the wavefunction of electrons on graphene is a two-component spinor, many interesting new physical properties are predicted and / or observed in graphene. The examples include Klein tunneling [11, 12], specular Andreev reflection [8, 13] (see also Section 2.5.1), and quantum Hall effect [4, 14–16] (see also Section 2.2).

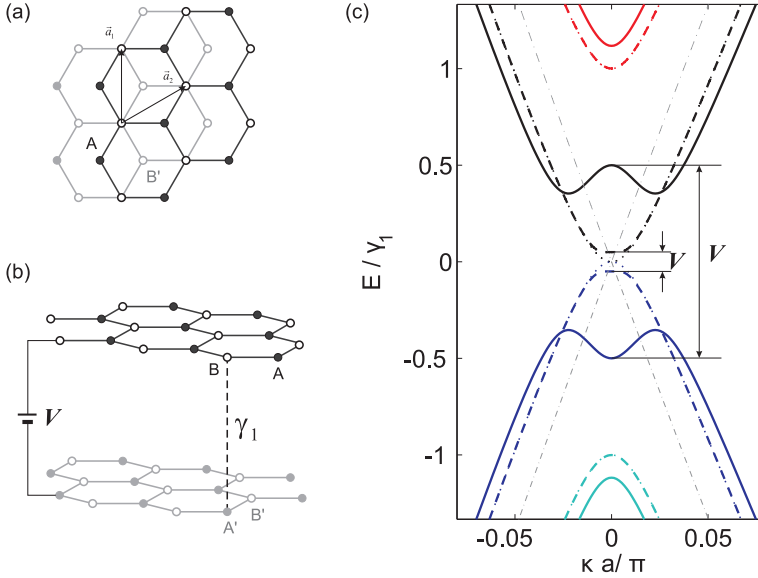


Figure 2.4: Illustrations of the lattice structure of bilayer graphene: (a) top view; and (b) 3D view. The black (gray) filled and open circles represent the A (A') and B (B') sublattices on the top (bottom) layer, respectively. The lattice sites B sit exactly on top of A' lattice sites for Bernal stacking, and the overlapping integral between these two sites is denoted as γ_1 as indicated. V indicates the bias applied between the top and bottom layers. (c) The band structure of bilayer graphene around the K point calculated using $\gamma_1 = 0.1 t$, $V = \gamma_1$ (solid lines), $V = 0.1 \gamma_1$ (dashed lines), and $V = 0$ (thin dotted lines). For comparison, the band structure of a single layer graphene around the K point is also shown on the same plot with the gray thin dash dotted line.

2.1.3 The band structure of bilayer graphene

Fig. 2.4(a) and (b) show the lattice structure of bilayer graphene with Bernal stacking. Bilayer graphene (BLG) has the same hexagonal lattice as monolayer graphene with lattice vectors \vec{a}_1 and \vec{a}_2 , but there are now four atoms per unit cell, A , B from top layer and A' , B' from bottom layer. As a result, the dispersion of BLG contains four bands. The lattice sites B sit exactly on top of A' lattice sites and are the nearest neighbours across the two layers. The overlapping integral between these two sites is denoted as γ_1 following the conventions of graphite. $\gamma_1 \approx 0.1 t \approx 0.3$ eV [17]. Around the K points, the pairs $A' - B$ repel each other and form the two higher energy bands. These higher energy bands are at around 300 meV (γ_1 as show in Fig. 2.4c) away from zero energy and can be safely neglected for low energy transport properties. Electrons hop between the two sites $A - B'$ via the $A' - B$ dimer and form the two lower energy bands (the direct overlap integral between $A - B'$ sites γ_3 is much smaller and is neglected) [14]. The two-component spinor for BLG is formed by wavefunctions of A and B' sublattices. Notice that the two sublattices for BLG are on two separate layers.

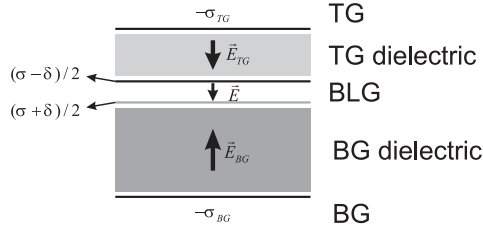


Figure 2.5: Illustration of the potential difference between the top and bottom layer of BLG induced by doping with a top gate and a back gate.

The dispersion relation for BLG is described by [14, 17, 18]:

$$E_{\pm}^2(p) = v_F^2 p^2 + \gamma_1^2/2 + V^2/4 \pm \sqrt{\gamma_1^4/4 + (\gamma_1^2 + V^2)v_F^2 p^2} \quad (2.4)$$

where the + sign gives the higher energy bands and the – sign gives the lower energy bands. V is the on-site potential difference between the two sublattices A and B' .

Fig. 2.4c shows the calculated band structure of BLG around one K point based on Eq. 2.4. When bias V is zero (the top and bottom layers are symmetric), the spectrum is parabolic, and the conduction and valence bands are degenerate at the K points. The effective mass of symmetric BLG is $m^* = \gamma_1/2v_F^2 \approx 0.03m_0$ [14].

Asymmetric gap in bilayer graphene

The degeneracy between the conduction and valence band at the K points can be lifted if the symmetry between the A and B' lattice sites are broken. As the A and B' lattice sites are sitting on two layers, the symmetry can be broken by creating a potential difference V between the two layers. Fig. 2.4c also show the spectra for a finite potential difference V . Here the spectra deviate slightly from the parabolic dispersion relation and show a Mexican-hat-like structure. At exactly the K points, the electron and hole states are separated by V . But the band gap $E_g = \sqrt{V^2\gamma_1^2/(V^2 + \gamma_1^2)}$ is slightly smaller than V for $V \ll \gamma_1$.

The potential difference between the two layers can be generated by doping the bilayer as shown both theoretically [18] and experimentally [17, 19, 20]. Below we discuss the mechanism of doping induced asymmetry based on the setup used in ref. [20] where the BLG is sandwiched between a back gate (BG) and a top gate (TG). The results can be generalized for other experimental setups used in literature.

A gate voltage V_G induces charge carriers on graphene and the charge density is $\sigma_G = C_G V_G$ where C_G is the gate capacitance per unit volume. For a device with a top gate at voltage V_{TG} and a back gate at voltage V_{BG} as illustrated by Fig. 2.5, the total charge density σ induced on the BLG is $\sigma = \sigma_{TG} + \sigma_{BG}$. For experimental setups other than the double-gated structure, σ is still equal to the total density induced on

BLG. Assume that the charge carriers are distributed between the two layers in such a way that the charge density on the bottom layer is $(\sigma + \delta)/2$ and the charge density on the top layer is $(\sigma - \delta)/2$. The difference in the charge density δ is due to screening. $\delta = 0$ for the case of zero screening. In refs. [17, 18], the value for δ is calculated self-consistently.

Since the electric field above a plane with uniform charge density σ is $\sigma/(2\epsilon)$ [21], the electric field through the bilayer is $\vec{E} = -(\sigma_{TG} - \sigma_{BG} + \delta)/(2\epsilon_0\epsilon_g)$ where ϵ_g is the dielectric constant of BLG. And the potential difference $V = \vec{E}c_0$ where $c_0 = 3.4 \text{ \AA}$ is the spacing between the two layers (value taken from graphite).

2.2 Landau levels and quantum Hall effect in graphene

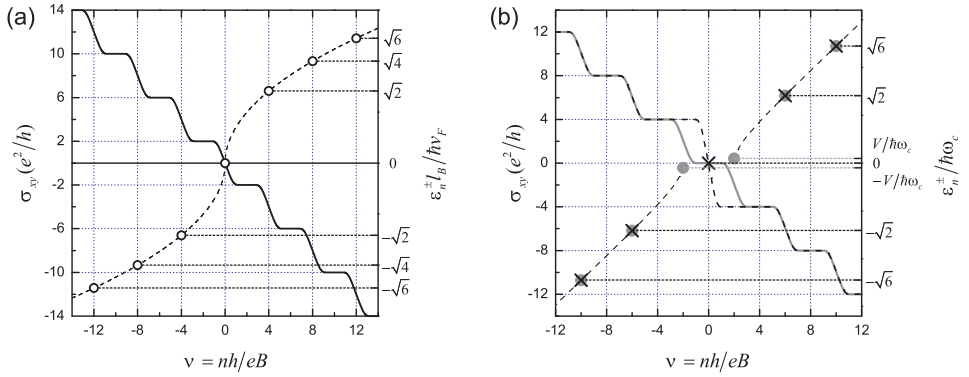


Figure 2.6: Quantum Hall effect and Landau levels in monolayer graphene and bilayer graphene. The horizontal axis is the filling factor ν which is equal to the carrier density n in the units of eB/h . (a) The solid black line plots Hall conductivity σ_{xy} in units of e^2/h . The positions of the Landau levels ϵ_n^\pm for $n = 0, 1, 2, 3$ are indicated by the circles. (b) Hall conductivity σ_{xy} for symmetric, gapless BLG (black dashed line) and for asymmetric, gapped BLG (gray solid line) in units of e^2/h . The positions of the Landau levels ϵ_n^\pm for $n = 0, 1, 2, 3$ are also shown for both gapless BLG (\times symbols) and gapped BLG (gray filled circles).

The Landau level ladder of monolayer and bilayer graphene are derived using either the full tight-binding Hamiltonian of the Dirac equation in the literature [14, 22]. The predictions have been verified by experiments [4, 15, 23]. Below we summarize the main results based on the literature.

2.2.1 Monolayer graphene

The Landau levels in monolayer graphene follow a square root dependence on the Landau level index n , in contrast to the case of 2DEG where the Landau levels follow an

equidistant ladder. They are described by [14, 22]:

$$\varepsilon_n^\pm = \pm \hbar v_F \sqrt{2|n|} / l_B \quad (2.5)$$

where the Landau level indices $n = 0, 1, 2, \dots$, the + and – signs are for electron and hole bands, respectively, and $l_B = \sqrt{\hbar/eB}$ is the magnetic length. The positions of the first few Landau levels are indicated in Fig. 2.6a.

Despite the fact the Landau levels scale with \sqrt{n} instead of n , they are still solutions of a harmonic oscillator. The Landau level degeneracy g is still proportional to the number of flux quanta $\Phi_0 = h/e$ per unit area, i.e. $g = f eB/h$ where f accounts for spin and orbital degeneracy and is equal to 4 for graphene because both spin and valley are doubly degenerate. It is only a function of the magnetic field and is independent on the dispersion relations of the materials.

However the occurrence zero energy Landau level ε_0 is truly peculiar [24]. The corresponding wavefunction of the zero energy Landau level is formed by orbitals on only the sublattice A (i. e. pseudo-spin up) for the K point and on only the sublattice B (i. e. pseudo-spin down) for the K' point. In other words, for the zero energy Landau level, the pseudo-spin is aligned with the iso-spin.

The quantized Hall conductivity σ_{xy} is directly related to the Landau level quantization in the integer quantum Hall regime. In the presence of disorder, Landau levels are broadened and localized states are available between the neighboring Landau levels. The centers of the broadened Landau levels are still occupied by the extended states. When the Fermi level of the system is in between two Landau levels, the longitudinal conductivity σ_{xx} and resistivity ρ_{xx} both vanish and the Hall conductivity is a constant that is a multiple of e^2/h . Here the edge states carry current and the bulk is insulating [25]. When the Fermi level of the system is in the center of a Landau level, due to the large degeneracy, scattering is possible and the longitudinal resistivity ρ_{xx} is finite, and the Hall conductivity σ_{xy} jumps to the next quantized value. The step height of the jump is equal to $f e^2/h$ where f is the number of states per flux quantum in the quantum Hall regime, or the orbital and l or spin degeneracy. Fig. 2.6a also shows the Hall conductivity for monolayer graphene. Notice that σ_{xy} makes a jump at zero density due to the presence of the zero energy Landau level. As the degeneracy of each Landau level is $4eB/h$ ($f = 4$ for graphene due to the two fold valley degeneracy and two fold spin degeneracy), the step size of each jump is $4e^2/h$.

2.2.2 Bilayer graphene

For symmetric, gapless BLG, the Landau level sequence at low energy can be approximated as [14]:

$$\varepsilon_n^\pm = \pm \hbar \omega_c \sqrt{n(n-1)} \quad (2.6)$$

where $n = 0, 1, 2, \dots$ are the Landau level indices, the + and – signs are for electron and hole bands, respectively, and $\omega_c = eB/m^*$ is the cyclotron frequency of BLG. Symmetric

BLG has also a zero energy Landau level. The corresponding wavefunction of the zero energy Landau level for BLG is formed by orbitals on only the sublattice B' from the bottom layer for the K valley and on only the sublattice A from the top layer for the K' valley [14]. Notice that for both $n = 0$ and $n = 1$, $\varepsilon_n^\pm = 0$, so the degeneracy of the zero energy Landau level for symmetric, gapless BLG is $8eB/h$. For Landau levels with $n > 1$, the degeneracies are $4eB/h$.

The Hall conductivity σ_{xy} for symmetric, gapless BLG is similar to that of monolayer graphene, and shows quantized values at $\pm 4e^2/h$, $\pm 8e^2/h$, $\pm 12e^2/h$, ... as shown in Fig. 2.6b by the black dashed line. Notice the unusual large jump of $8e^2/h$ for the zero energy Landau level due to the large degeneracy of this level. The corresponding Landau level positions are also shown in Fig. 2.6b by the \times symbols.

For asymmetric, gapped BLG with potential difference V between the top and bottom layers, the zero energy Landau level split into two levels at $\varepsilon_{0,1}^\pm = \pm V$ as indicated by the gray filled circles in Fig. 2.6b. The $\varepsilon_{0,1}^+ = V$ states are formed by orbitals on only sublattice A that are on the K' valley, and the $\varepsilon_{0,1}^- = -V$ states are formed by orbitals on only sublattice B' that are on the K valley.

The change in Landau level spectrum gives rise to different plateau values for σ_{xy} . For gapped BLG, a plateau can emerge at $\sigma_{xy} = 0$ if the gap is large enough, as indicated by the gray solid line in Fig. 2.6b. Notice that the quantum Hall effect thus provides a tool to probe the existence of the gap for BLG as demonstrated experimentally in ref. [17].

2.3 Graphene nanoribbons

Tight-binding theory and first principle calculations predicts a band gap in the energy spectra of graphene nanoribbons. Experiments show a "transport gap" that is much larger than the predicted band gap. Further theory takes into account disorder on the edges and predicts suppressed conductance even in the absence of a spectral gap. Below we first summarize the results from calculations based on ideal GNR with atomic smooth edges, followed by theoretical predictions for ribbons with rough edges.

2.3.1 Band structure of graphene nanoribbons with perfect edges

Fig. 2.7a depicts part of the atomic lattice of a graphene nanoribbon (GNR). The ribbon is called a zigzag ribbon if the piece extends to infinity along the x direction, and is called an armchair ribbon if it extends to infinity along the y direction. The spectrum of a perfect GNR depends strongly on the type of edge as well as on the width of the ribbon w .

For GNRs with armchair edges, the allowed values for κ_x are $n\pi/w - K$ [22, 26–28] where $n = 0, 1, \dots, 2w/a - 1$, a is the lattice constant. One can obtain the spectrum simply by "slicing" the 2D tight-binding dispersion of graphene obtained in section 2.1

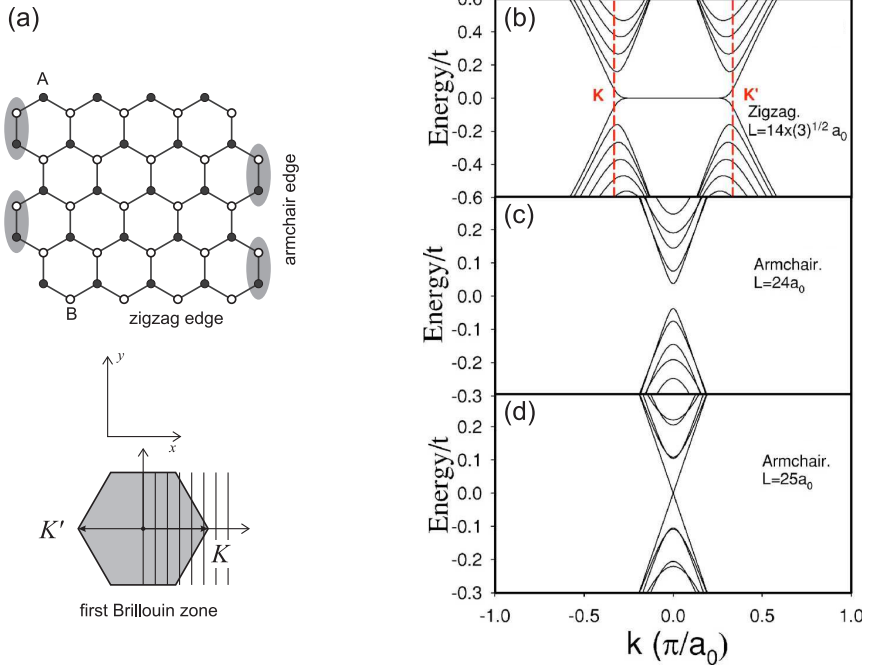


Figure 2.7: (a) Atomic lattice of a graphene nanoribbon with armchair or zigzag edge. The black and white atoms represent A and B sublattice. The gray ellipses indicate the possible formation dimers along armchair edges as described in the text. The orientation of the first Brillouin zone is also shown. (b-d) The calculated spectrum for graphene nanoribbons with zigzag edge (b), armchair edges with 24 rows of atoms (c) and armchair edges with 25 rows of atoms (d). The ribbon width is 6 nm for all three plots. The horizontal axis is k_x for (b) and k_y for (c, d). Figure taken from ref. [26].

for each allowed κ_x value. Fig. 2.7a illustrates the allowed κ_x values for a ribbon with width $w = 4a$. An armchair ribbon can be metallic if w/a is a multiple of 3 when some slices can go through the K points. As an example, the spectrum of a ribbon with width $w = 24a$ is shown in Fig. 2.7d (taken from ref. [26]). An armchair ribbon is semiconducting if w/a is not a multiple of 3 where no slices cuts through the K points. For semiconducting armchair ribbons, the size of the band gap is inversely proportional to the width of the ribbon:

$$E_g = 2\hbar v_F \pi / w \quad (2.7)$$

This relation predicts, for example, a band gap of 200 meV for a 20 nm wide ribbon.

Further theoretical studies notice that the two neighboring atoms (indicated by the ellipses in Fig. 2.7a) sitting on the edge of an armchair ribbon have one spare electron each and might lower its energy by forming a dimer [29]. With this perturbation taken into account, the resulting spectra show energy gaps for all armchair ribbons [29].

The spectra for GNRs with zigzag edges can be obtained from the tight-binding dispersion in a similar way as that of an armchair ribbon, except that a zigzag ribbon has two localized edge states originated from the A and B sublattices respectively. The edge states are shown in Fig. 2.7b. They have zero energy and are dispersiveless [22, 26–28]. Further theory that includes the spin degree of freedom predicts that the two edges of a zigzag ribbon will be spin polarized (magnetized) with opposite sign. The resulting spectrum shows an energy gap as well [29].

For a GNR with arbitrary boundaries (partially zigzag and partially armchair), theoretical studies find that the zigzag character dominates and the resulting spectrum is gapless. [30].

2.3.2 Effect of edge roughness on graphene nanoribbons

Experimentally, a transport gap has indeed been observed in GNR devices [31–33]. It is called a transport gap in the sense that low energy transport is suppressed in the gapped region. Several experimental observations however deviate from most theoretical expectations described in the previous section. For example, the measured gap size is independent on the crystallographic orientation of the ribbon in contrast to theoretical expectations (see also section 2.3). Further experimental work reveals other properties of the transport gap observed in common laboratory ribbons that differ from a clean band gap, including: (1) conductance peaks that resemble Coulomb blockade inside the gap [34–38]; (2) temperature dependence of the conductance beyond simple activated transport behavior [39, 40]; (3) an increase in conductance and a decrease in gap size with increasing perpendicular magnetic field [40]; (4) a decrease in gap size upon annealing [38].

To explain the diverse experimental results, several theories suggest that the observed transport gap can be induced by disorder from the substrate / environment, or by the atomically rough edges of the experimental GNR systems. There are mainly three

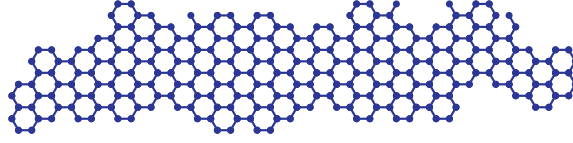


Figure 2.8: Schematic illustration of the lattice structure of a GNR with rough edges.

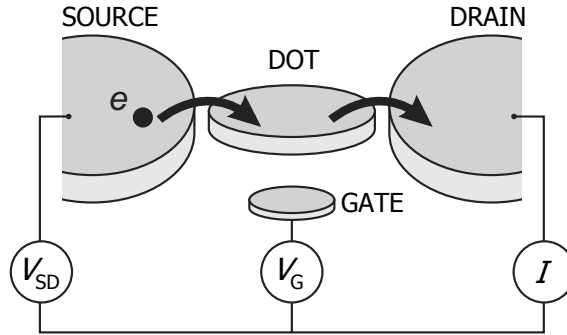


Figure 2.9: Schematic picture of a quantum dot. The dot is connected to the source and drain contacts via two tunnel barriers. A gate couples capacitively to the electrons on the dot, which allows their energy levels to be controlled. The current I through the device can be measured as a function of the applied bias and gate voltage. Figure from ref. [48].

possible mechanisms: charged impurities scattering due mainly to the substrate or device processing [37, 41], Anderson localization due to scattering at the edges [42–47], and Coulomb blockade due to the finite size [29]. These are plausible mechanisms for most laboratory ribbons as described also in chapter 3 of this thesis. Fig. 2.8 schematically illustrates one imagined scenario of the ribbon edge on an atomic scale.

2.4 Quantum dots

2.4.1 The constant interaction model of a single quantum dot

A quantum dot consists of a very small island (the "dot") that is weakly coupled to the environment, such that the charges on the island no longer behave like a continuous variable. A quantum dot device allows one to control the number of charge carriers (electrons or holes). Extensive studies of various quantum dot systems have been carried out during the past few decades as reviewed in refs. [49–51].

An example of a quantum dot device is schematically illustrated in Fig. 2.9. In this case the dot is capacitively coupled to a gate, and is separated from the two reservoirs (the source and drain) by two tunnel barriers. By measuring the current due to the

transport of electrons (holes) through the dot, one can map out the charge stability diagram of the dot, which is often successfully interpreted based on the *constant interaction* model. In this section, we briefly summarize the main results of the constant interaction model following refs. [49–51].

The constant interaction model assumes that (1) the interactions among electrons on the dot and the interactions between the electrons on the dot and the environment can be described by a constant capacitance C ; and (2) the single particle energy level spacing is independent of the number of electrons on the dot. For the example described in Fig. 2.9, the total capacitance C is the sum of the capacitances between the dot and the source C_s , the drain C_d , and the gate C_G , i.e. $C = C_s + C_d + C_G$. Here all capacitance values are determined by the geometry and size of each capacitor.

For a dot with N electrons in the ground state, with voltages V_s , V_d , and V_G applied to the source, drain, and gate respectively, the total energy $F(N)$ of the N electrons includes contributions from both the electrostatic energy and the electronic energy levels,

$$F(N) = \frac{[-eN + C_s V_s + C_d V_d + C_G V_G]^2}{2C} + \sum_{n=1}^N E_n,$$

where the first term is the electrostatic energy and E_n represent the single particle energy levels.

The electrochemical potential $\mu(N) = dF(N)/dN$ is found to be,

$$\mu(N) = F(N) - F(N-1) = \left(N - \frac{1}{2}\right) E_c - \frac{E_c}{e} (C_s V_s + C_d V_d + C_G V_G) + E_N, \quad (2.8)$$

where $E_c = e^2/C$ is the charging energy of the dot. We see that the electrochemical potential of the dot can be adjusted by the voltage on the gate, the source and the drain electrodes via the capacitive couplings.

The difference between the chemical potentials of two successive charge states is call the addition energy E_a and is,

$$E_a(N) = \mu(N+1) - \mu(N) = E_c + \delta E$$

where $\delta E = E_{N+1} - E_N$ is the difference between the $N+1$ th and the N th energy levels, and is zero if the two energy levels are degenerate. The spacing between two charge states therefore includes two contributions, the charging energy E_c from the electrostatic energy and the electronic level spacing δE from confinement. Notice that the electrochemical potential of a quantum dot is not continuous, and a minimal energy $E_c = e^2/C$ is required to add an additional electron to the dot. When the size of the dot is small, the total capacitance is also small, and the charging energy is large. Below we show that at low temperature $T \ll E_c$, stable voltage configurations can be found where the number of electrons on the dot is fixed. We consider the situation where the

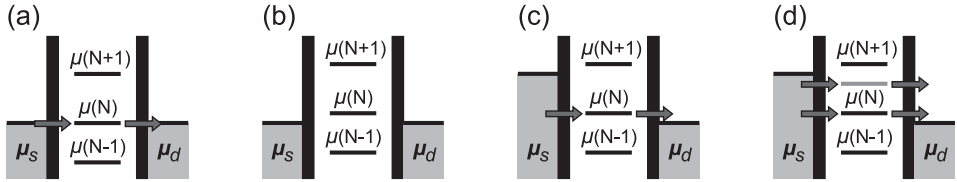


Figure 2.10: Schematic diagrams of the electrochemical potentials of the quantum dot for different electron numbers and gate and bias voltages. (a, b) Coulomb blockade for the low bias regime. (a) When the chemical potentials of the source (μ_s) and drain (μ_d) are aligned with the dot electrochemical potential of N electron ground state $\mu(N)$, current can flow through the quantum dot device via the path indicated by the gray arrows. (b) When no electrochemical potential on the dot is within the bias window, no current can flow and the number of electrons on the dot is fixed to $N-1$. (c, d) High bias regime. (c) With increasing bias window, the N electron ground state becomes an available path again and current can flow through the dot again. (d) In the high bias regime, transport through excited states (gray line) can also take place when the excited states are within the bias window. An electron can now tunnel through the dot via two possible paths. Note however that only one of them can be used at a time, due to Coulomb blockade.

drain electrode is connected to the ground (which is the case for all our measurements), i.e. $V_d = 0$.

Low-bias regime

First we consider the situation where an infinitesimally small voltage is applied between the source and the drain electrodes, as illustrated in Fig. 2.10a and 2.10b. When the electrochemical potential for N electrons is aligned with the chemical potential of the source μ_s and the drain μ_d ($\mu_s \approx \mu_d$), a current can flow through the quantum dot device (Fig. 2.10a), and the number of electrons on the dot alternates between N and $N-1$. The amount of current is determined by the tunneling rates of the two tunnel barriers Γ_s and Γ_d , as well as the temperature of the system. When one decreases the voltage on the gate, $\mu(N)$ increases and is no longer aligned with μ_s and μ_d . Now the electronic transport is blocked and no current can flow through the dot and the number of electrons on the dot is fixed to $N-1$ (Fig. 2.10b). This is called the *Coulomb blockade*. Fig. 2.11a shows current through a quantum dot as a function of the gate voltage. We see that the current oscillates between zero and a peak value with increasing gate voltage, as electrons are added to the dot one by one. Following eq. 2.8, the spacing between the two neighbouring peaks is $\Delta V_G = E_a/\alpha$ where $\alpha \equiv eC_G/C$ is often referred to as the α -factor which converts the addition energy to a gate voltage. When the level spacing δE is small compared to the charging energy E_c , the peak spacing is approximately $\Delta V_G \approx e/C_G$.

High bias regime and excited states

The Coulomb blockade can be lifted not only by the gate voltage, but also by the source drain bias. For instance for the situation described in Fig. 2.10b where the number of electrons is fixed to $N-1$ on the dot and the current through the dot is zero, if

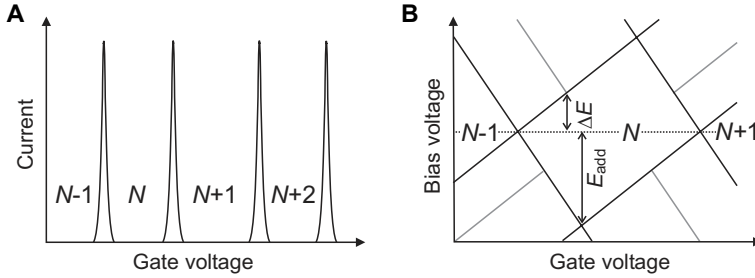


Figure 2.11: (a) At low bias, the discrete energy levels in the quantum dot give rise to spikes in the current, when a chemical potential is in the bias window. The gate voltage controls the number of electrons on the dot. (b) Sweeping both bias and gate voltage, the characteristic Coulomb diamonds can be seen. Inside the diamond region the number of electrons on the dot is fixed and no current can flow. Outside the diamond current can flow through either the dot ground state or excited states. Multiple electron tunneling occurs at even higher bias, when the edges corresponding to $N-1$ and $N+1$ have crossed. The onset of an extra tunnel path is marked by a change in current through the dot along a line. From these lines, the energy spectrum of the dot can directly be extracted. The slanted letters in the figure correspond to the alignment of chemical potentials in Fig. 2.10a-d

one increase the chemical potential of the source electrode μ_s by decreasing V_s , then at some V_s value, the dot level $\mu(N)$ will be within the bias window again and transport is allowed again (see Fig. 2.10c). The condition for nonzero current can be written as $0 < \mu(N) < -eV_s$ for negative V_s , and $0 > \mu(N) > -eV_s$ for positive V_s . Inserting eq. 2.8 to the two conditions, the results can be plotted on the V_G - V_s plane as shown in Fig. 2.11b with the black solid lines. Within the diamond shaped regions on the V_G - V_s plane, the number of charges on the dot is fixed as indicated on the graph. Between two diamonds with charges N and $N+1$, the number of charges fluctuates between N and $N+1$. Along the two solid lines that define this region, the dot electrochemical potential $\mu(N)$ is aligned with μ_s (with slope $C_G/(C-C_s)$) and μ_d (with slope $-C_G/C_s$) respectively. And the tip of the diamond is a direct measure of the addition energy. Such a plot as shown in Fig. 2.11b is often referred to as the stability diagram. In an electric transport measurement, one can directly map out the stability diagram by monitoring the current through the device, as current is zero within the diamonds and nonzero otherwise.

The analysis above consider only transitions between ground states. In the high bias regime, transport through a quantum dot device can also take place via an excited state. Fig. 2.10d illustrates one example, where both the ground state $\mu(N)$ (black line) and an excited state (gray line) are within the bias window. There are then two paths available for an electron to tunnel through the dot. In general, this will lead to a change in current through the device. In an measurement as in Fig. 2.11b, transport through excited states will appear as an increase in current along lines parallel to the ground state lines which form the diamond shape, as illustrated by gray lines in Fig. 2.11b. When one excited

state line intercept with an diamond, the size of the bias window exactly equals to the level spacing. One can thus read out the energy level spacing directly from the bias axis of a stability diagram.

In summary, to map out the stability diagram is extremely useful for extracting various dot parameters, such as energy level spacing, gate to dot capacitance, source to dot capacitance and total capacitance.

2.4.2 Double quantum dots

In this section we briefly outline the basic theory concerning the stability diagrams of a double quantum dot, following refs. [49, 52]. A double quantum dot includes two coupled single quantum dot. We assume a setup where two dots are separated by another tunnel barrier, and two gates (G1 and G2) that are capacitively coupled to the two dot respectively. The charge states of a double quantum dot can be described by the extending the constant interaction model for single quantum dots to include the additional dot, a second gate, and an interdot capacitive coupling.

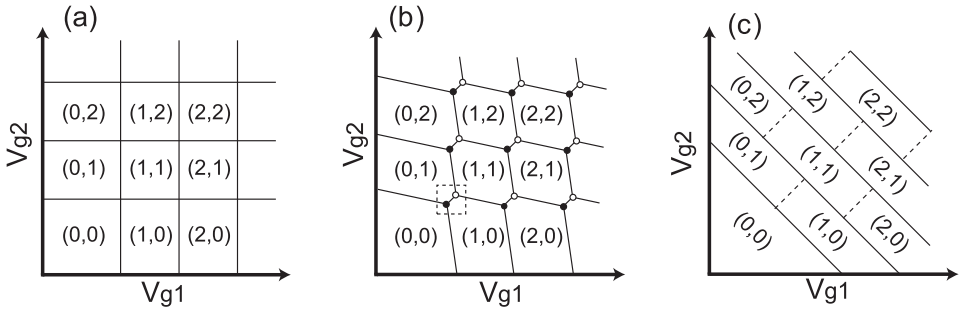


Figure 2.12: Schematics of a double dot stability diagram for weak (a), intermediate (b) and strong (c) interdot electrostatic couplings. The charge on the dot is indicated as (N_1, N_2) . (Figures are taken from [52])

In the low bias regime, the stability diagrams are plotted on the V_{G1} - V_{G2} plane in Fig. 2.12a to 2.12c for increasing interdot coupling, and a detailed derivation can be found in ref. [52]. Below we give a qualitative picture for understanding the stability diagrams of a double quantum dot in the low bias regime.

First, for the two dots that are completely decoupled, the resulting stability diagram is shown in Fig. 2.12a. Here each vertical (horizontal) line represents one Coulomb peak of dot 1 (2), and along the V_{G1} (V_{G2}) axis, the number of electrons on dot 1 (2) changes. The V_{G1} - V_{G2} plane is therefore divided into many rectangles within which the number of charges on both dots are fixed. The number of charges on each dot is indicated for each rectangle in Fig. 2.12a as well. When the two dots are connected in series, the current through the entire double dot device is nonzero only at the points where the

horizontal and vertical lines intercept. At these points, the chemical potential of the source, the drain, dot 1, and dot 2 are all aligned.

Next, Fig. 2.12b shows the well-known honeycomb shaped stability diagram of a double quantum dot with finite interdot coupling. Here when the number of charges on one dot changes by one, the other dot "feels" the potential change on the first dot via the interdot coupling and the position of the Coulomb peak of the second dot shifts by an amount proportional to this potential change. Each intercepting point in the previous case then splits into two so-called triple points. The splitting between the two triple points is proportional to the interdot coupling. At each triple point, three different charge states have the same energy and the number of charges on the double dot can fluctuate. Fig. 2.13a zooms in to one pair triple points, and the corresponding energy diagrams at different locations of the stability diagram are also sketched. Notice that each Coulomb peak line now deviate from exactly horizontal or vertical, due to finite capacitive coupling between dot 1 (2) and gate 2 (1). When the two dots are connected in series, current through the entire double dot device is nonzero only at the triple points.

When the two dots are strongly coupled, the two dots essentially merge into one dot which are capacitively coupled to both G1 and G2. The resulting charge stability diagram consists of parallel diagonal lines as illustrated in Fig. 2.12c.

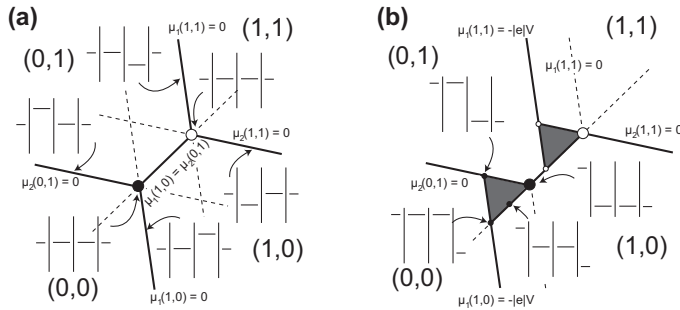


Figure 2.13: Zoom in of the dotted square region in Fig. 2.12b at zero (a) and finite bias (b). Black lines represent the alignment of a dot chemical potential level with at least one lead chemical potential. (a) At zero bias, charge transport can only occur at the two triple points at the intersections of the solid lines. The line connecting the triple points indicates the alignment of the chemical potentials of the two dots. Inset diagrams show the configuration of the ground-state electrochemical potentials at the indicated position in the charge stability diagram. (b) At finite bias $-|e|V$ the triple points develop into triangles defined by the gray area. For one discrete level inside the dot, elastic transitions are only possible at the baseline of the triangles, where both dot chemical potentials are aligned. At finite detuning, δ , cotunneling and inelastic transitions can contribute to the current. (Figures after [52])

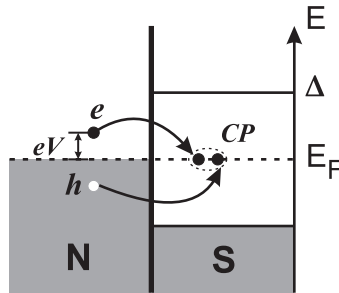


Figure 2.14: Schematic representation of Andreev reflection. An electron (e) in the normal metal (N) with energy eV smaller than the superconducting gap Δ pairs with another electron with energy eV below the Fermi energy to enter the superconductor (S) as a Cooper pair (CP). A hole (h) is left in the N region.

We next consider a double quantum dot with intermediate interdot coupling strength at a finite bias. In this case each triple point grow into a triangle shape within which current is nonzero. This is illustrated in Fig. 2.13b along with sketches of the corresponding energy diagrams at different locations of the stability diagram. When the bias window becomes larger than the charging energy, the triangles from two neighbouring charge states begin to overlap. The size of the triangle gives information on the charging energies of the two dots.

2.5 Andreev reflection in the quantum Hall regime

In this section we consider a setup where a normal metal (N) is in contact with a superconductor (S). The single particle spectrum of the superconductor has a gap of size 2Δ around the Fermi energy E_F . Andreev reflection (AR) is an important transport process at such an N-S interface. Here a basic introduction to the Andreev reflection processes is presented. In addition, a classical theory that describes AR in a strong perpendicular magnetic field is also outlined.

2.5.1 Andreev reflection

We consider an electron in a normal conducting metal with an energy $eV < \Delta$ above the Fermi energy approaching a clean N-S interface. Due to the presence of a gap in the excitation spectrum of the superconductor no electron states are available at energies $eV < \Delta$ in the superconductor. As a result, the electron is reflected and no transport occurs across the N-S interface to the first order. Higher order processes such as Andreev reflection [53] are however possible. Below we outline the main properties of AR following Chapter 6 of ref. [53].

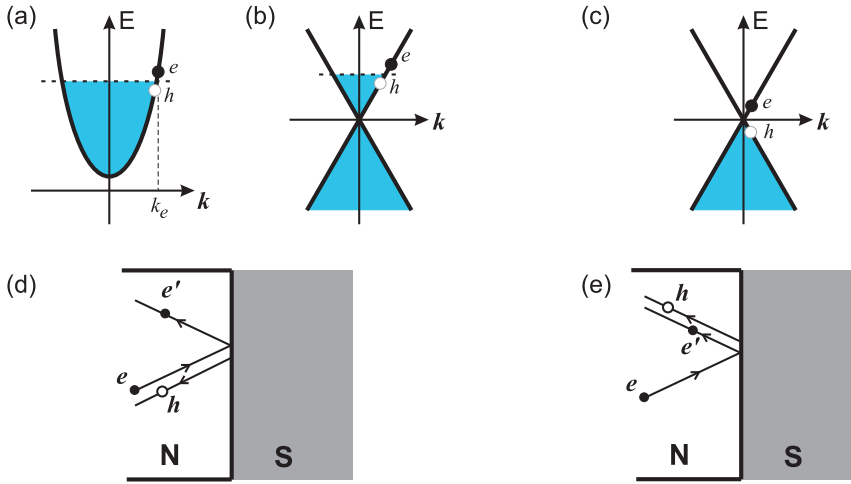


Figure 2.15: The energy diagrams of Andreev reflection in the case of $E_F \gg eV$ (retro-reflection) for parabolic dispersion (a), linear dispersion (b), and in the case of $E_F = 0$ (specular reflection) for linear dispersion (c). The incoming electrons e are represented by filled circles. The reflected holes h are represented by open circles. The shaded regions represent filled Fermi sea. The trajectories of the incoming electron (e), normally reflected electron (e'), and Andreev reflected hole h in the real spacing are shown in (d) for the case of retro-reflection and (e) for the case of specular reflection. The hole "rays" are displaced for clarity.

The basic process of Andreev reflection is schematically shown in Fig. 2.14. An electron e with energy eV above the Fermi energy ($eV < \Delta \ll E_F$) and wave vector $k_e \approx k_F$ impinges on the N-S interface. At the interface the electron can pair up with a second electron e_2 with energy eV below the Fermi energy to enter the superconductor as a Cooper pair. The absence of the electron e_2 below E_F leaves a hole h with energy eV below E_F in the N region. This is the so called Andreev reflection where an electron is reflected as a hole. Alternatively, a hole impinging on the N-S interface can also be Andreev reflected as an electron. During this process, two electron charges are transferred across the N-S interface, resulting in finite conductance.

To form a Cooper pair, the second electron e_2 needs to have opposite momentum $-k_e$ and opposite spin compared to the first electron. As a result, the Andreev reflected hole would have approximately the same momentum as the first electron $k_h \approx k_e$. This is illustrated by the energy diagrams in Fig. 2.15a and b. As the incoming electron and the reflected hole have energies just above and below the Fermi energy, respectively, and the effective mass of a hole is opposite to an electron, the hole would have opposite velocity as the incoming electron. In real space, the hole will trace back the path of the first electron as shown in Fig. 2.15d. In other words, it is *retro-reflected*. For the case where $E_F \gg eV$, the properties of AR discussed above are valid for both parabolic (Fig. 2.15a) and linear (Fig. 2.15b) dispersions.

For an N-S interface with transmission probability $T < 1$, there is also finite probability that the incoming electron will be reflected as an electron e' . Using Landauer formalism, the conductance of an N-S interface is

$$G_{NS} = N \frac{4e^2}{h} \frac{T^2}{(2-T)^2}$$

where N is the total number of modes contributing to transport. This can be contrasted to normal Landauer formula $G_{NN} = T \cdot 2Ne^2/h$. If the N-S interface has unity transmission $T = 1$, the conductance $G_{NS} = 4Ne^2/h$ that is twice as high as G_{NN} . This is because each AR transfers two charges across the N-S interface. If the transmission through the N-S interface is zero, then the conductance $G_{NS} = 0$, indicating that all incoming electrons will be reflected as electrons. For most N-S interfaces, the transmission $0 < T < 1$, so the conductance is larger than zero but smaller than $4Ne^2/h$.

Specular Andreev reflection in graphene around K points

When graphene is in contact with a superconductor, AR may also occur when the excitation energy $eV > E_F$. In this case, it is found that the AR is specular [8, 13]. The specular AR process in graphene is illustrated in Fig. 2.15c and 2.15e for $E_F = 0$. In this case, the incoming electron is in the conduction band. It pairs up with a second electron e_2 from the valence band to enter the superconductor as a Cooper pair. A hole in the valence band is left in the N region. The incoming electron and the reflected hole still have the same momentum. But the valence band hole lies on a different branch than the incoming electron and as a result the velocity is in the same direction as the momentum, so that the reflection is specular (Fig. 2.15e).

2.5.2 Andreev reflection in high magnetic field

In this section we consider the hybrid system of a semiconductor-superconductor (Sm-S) interface, where the electrons from the semiconductor are quantized in Landau levels under a perpendicular magnetic field. Numerous theoretical studies show that for a moderately disordered Sm-S interface, in the high filling factor regime, the two terminal resistance oscillates periodically in the filling factor ν , with a larger oscillation amplitude than that of Shubnikov-de Haas (SdH) oscillations [54–56]. When only one or two Landau levels are populated, numerical studies show that the conductance oscillates with a periodicity that is uncorrelated to the filling factor, and the conductance can reach zero at the valleys of oscillations [57]. Below I summarize a classical theory that describes the physics of AR in the high filling factor regime.

Fig. 2.16 illustrates the main idea. In a perpendicular magnetic field, electrons travel in skipping orbits along the edge of the normal conductor until they reach the Sm-S interface. (a) When the Andreev reflection amplitude $|r_{eh}|$ is zero, the electrons will be

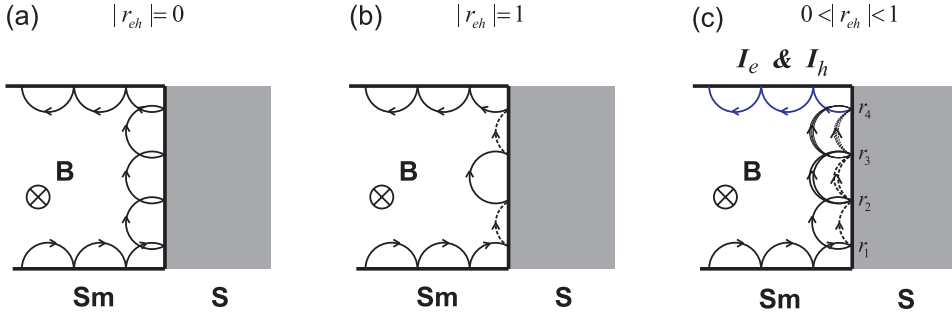


Figure 2.16: Schematic illustrations of AR in a perpendicular magnetic field B for different Andreev reflection amplitudes $|r_{eh}|$ as indicated on top of each graph. The trajectories of electrons and holes in a perpendicular magnetic field B are described by the classical skipping orbits. The dashed line represent hole waves and the solid lines represent electron waves. I_e and I_h indicates electron and hole current, respectively.

reflected normally with 100 % probability and continue traveling in skipping orbits (see Fig. 2.16a). The conductance through the Sm-S interface is low. (b) When the Andreev reflection amplitude $|r_{eh}|$ is 1, an impinging electron will go through Andreev reflection and be converted into a hole. The holes have opposite charge, opposite velocity, and opposite effective mass to the original electrons, therefore they will be skipping in the same direction. The outgoing state at the exit of the Sm-S interface is of hole (electron) character if the length of the Sm-S interface is such that it was reflected for an odd (even) number of times. In the case of hole outgoing state, the conductance is therefore twice as large as the case of normal contact because a Cooper pair is created in the superconductor. In the case of electron outgoing state, the conductance is zero. As a function of magnetic field, the conductance oscillates between this two extreme values. (c) When the Andreev reflection amplitude $0 < |r_{eh}| < 1$ as illustrated in Fig. 2.16c. In this case the incoming electron wave is partially reflected as hole with probability amplitude $|r_{eh}|$ and partially as electron with probability amplitude $|r_{ee}|$. The hole (electron) wave can be reflected again at the Sm-S interface (at point r_2 in Fig. 2.16c) and becomes another electron (hole) wave with probability amplitude $|r_{eh}|$ and another hole (electron) wave with probability amplitude $|r_{ee}|$ (assuming $|r_{ee}| = |r_{hh}|$). There are then four waves in total after the second reflection. The two electron waves interfere with each other, and the two hole waves interfere. This process goes on. After one skipping orbit, an electron (hole) wave accumulates an Aharonov-Bohm phase $\pi\nu$ ($-\pi\nu$) where $\nu = nh/eB$ is the filling factor. The conductance through the Sm-S interface is calculated after summing all the contributions. One first sums over all complex amplitudes of the electron waves and hole waves separately, then sum the total probability of the electron term and the hole term. The resulted conductance oscillation is described by a sum of oscillations with periodicity of ν (after twice reflections) and its higher harmonics due to multiple

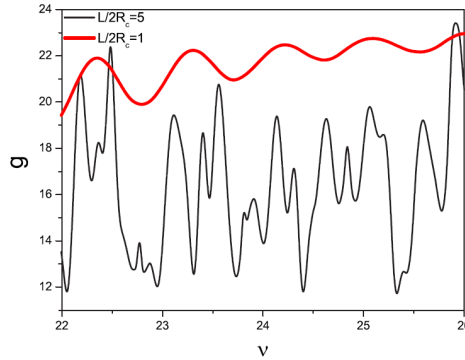


Figure 2.17: Calculated conductance in a perpendicular magnetic field for an Sm-S interface without disorder. Figure taken from ref. [56].

reflections:

$$G \propto 1 + g_1 \cos(2\pi\nu + \delta) + g_2 \cos(4\pi\nu + \delta) + \dots \quad (2.9)$$

where g_1, g_2, \dots are coefficients for each term and are on the same order of magnitude for the case without disorder. Eqn. 2.9 describes the conductance of a perfect Sm-S interface in a perpendicular magnetic field when many Landau levels are occupied.

Fig. 2.17 from ref. [56] plots numerical results. The thick line is calculated for the case where the length L of the Sm-S interface is equal to the cyclotron diameter, the electrons are reflected only once, and conductance oscillates more or less periodically in the filling factor ν . The thinner line is calculated for the case where the length L of the Sm-S interface is five times the cyclotron diameter, and the resulted oscillation is aperiodic, but with a large amplitude.

However, most experimental Sm-S interfaces are far from perfect and the effect of disorder has to be taken into account. Ref. [55, 56] found that the coefficients of the higher harmonics decrease rapidly when disorder is included in the simulations. As a result, conductance is expected to oscillate periodically in ν after reflections from a disordered Sm-S interface.

Some of these predictions have already been verified experimentally by Eroms *et al.* [58] and other groups [59, 60] on InAs 2DEGs in the large filling factor regime. Below the critical temperature of the superconductor, the amplitude of Shubnikov-de Haas oscillations is found to be larger than that above T_c .

References

- [1] P. R. Wallace, *The Band Theory of Graphite*, Physical Review Online Archive (Prola) **71**, 622 (1947).
- [2] S. Iijima, *Helical microtubules of graphitic carbon*, Nature **354**, 56 (1991), ISSN 0028-0836.
- [3] K. S. Novoselov, A. K. Geim, S. V. Morozov, D. Jiang, Y. Zhang, S. V. Dubonos, I. V. Grigorieva, and A. A. Firsov, *Electric Field Effect in Atomically Thin Carbon Films*, Science **306**, 666 (2004).
- [4] Y. Zhang, Y.-W. Tan, H. L. Stormer, and P. Kim, *Experimental observation of the quantum Hall effect and Berry's phase in graphene*, Nature **438**, 201 (2005), ISSN 0028-0836.
- [5] C. Schönberger, *Bandstructure of graphene and carbon nanotubes: an exercise in condensed matter physics* (2000), URL <http://pages.unibas.ch/phys-meso/Education/Teaching/Nanotubes/LCAO-NT.pdf>.
- [6] E. Minot, Ph.D. thesis, Cornell University (2004).
- [7] V. P. Gusynin, S. G. Sharapov, and J. P. Carbotte, *Ac Conductivity Of Graphene: From Tight-Binding Model To 2+1-Dimensional Quantum Electrodynamics*, International Journal of Modern Physics B **21**, 4611 (2007).
- [8] C. W. J. Beenakker, *Colloquium: Andreev reflection and Klein tunneling in graphene*, Reviews of Modern Physics **80**, 1337 (2008).
- [9] P. L. McEuen, M. Bockrath, D. H. Cobden, Y. G. Yoon, and S. G. Louie, *Disorder, Pseudospins, and Backscattering in Carbon Nanotubes*, Physical Review Letters **83**, 5098 (1999).
- [10] H. B. Heersche, P. Jarillo-Herrero, J. B. Oostinga, L. M. K. Vandersypen, and A. F. Morpurgo, *Bipolar supercurrent in graphene*, Nature **446**, 56 (2007), ISSN 0028-0836.
- [11] M. I. Katsnelson, K. S. Novoselov, and A. K. Geim, *Chiral tunnelling and the Klein paradox in graphene*, Nature Physics **2**, 620 (2006), ISSN 1745-2473.
- [12] A. F. Young and P. Kim, *Quantum interference and Klein tunnelling in graphene heterojunctions*, Nature Physics **5**, 222 (2009), ISSN 1745-2473.
- [13] C. W. J. Beenakker, *Specular Andreev Reflection in Graphene*, Physical Review Letters **97**, 067007 (2006).

-
- [14] E. McCann and V. I. Fal'ko, *Landau-Level Degeneracy and Quantum Hall Effect in a Graphite Bilayer*, Physical Review Letters **96**, 086805 (2006).
- [15] K. S. Novoselov, E. McCann, S. V. Morozov, V. I. Fal'ko, M. I. Katsnelson, U. Zeitler, D. Jiang, F. Schedin, and A. K. Geim, *Unconventional quantum Hall effect and Berry's phase of 2π in bilayer graphene*, Nature Physics **2**, 177 (2006), ISSN 1745-2473.
- [16] K. S. Novoselov, Z. Jiang, Y. Zhang, S. V. Morozov, H. L. Stormer, U. Zeitler, J. C. Maan, G. S. Boebinger, P. Kim, and A. K. Geim, *Room-Temperature Quantum Hall Effect in Graphene*, Science **315**, 1379 (2007).
- [17] E. V. Castro, K. S. Novoselov, S. V. Morozov, N. M. R. Peres, L. dos Santos, J. Nilsson, F. Guinea, A. K. Geim, and A. H. C. Neto, *Biased Bilayer Graphene: Semiconductor with a Gap Tunable by the Electric Field Effect*, Physical Review Letters **99**, 216802 (2007).
- [18] E. McCann, *Asymmetry gap in the electronic band structure of bilayer graphene*, Physical Review B **74**, 161403 (2006).
- [19] T. Ohta, A. Bostwick, T. Seyller, K. Horn, and E. Rotenberg, *Controlling the Electronic Structure of Bilayer Graphene*, Science **313**, 951 (2006).
- [20] J. B. Oostinga, H. B. Heersche, X. Liu, A. F. Morpurgo, and L. M. K. Vandersypen, *Gate-induced insulating state in bilayer graphene devices*, Nature Materials **7**, 151 (2007), ISSN 1476-1122.
- [21] D. J. Griffiths, *Introduction to Electrodynamics* (Prentice-Hall, New Delhi, 2008).
- [22] A. H. Castro Neto, F. Guinea, N. M. R. Peres, K. S. Novoselov, and A. K. Geim, *The electronic properties of graphene*, Reviews of Modern Physics **81**, 109 (2009).
- [23] K. S. Novoselov, A. K. Geim, S. V. Morozov, D. Jiang, M. I. Katsnelson, I. V. Grigorieva, S. V. Dubonos, and A. A. Firsov, *Two-dimensional gas of massless Dirac fermions in graphene*, Nature **438**, 197 (2005), ISSN 0028-0836.
- [24] Y. Zheng and T. Ando, *Hall conductivity of a two-dimensional graphite system*, Physical Review B **65**, 245420+ (2002).
- [25] P. L. Taylor and O. Heinonen, *A Quantum Approach to Condensed Matter Physics* (Cambridge University Press, Cambridge, UK, 2002).
- [26] L. Brey and H. A. Fertig, *Electronic states of graphene nanoribbons studied with the Dirac equation*, Physical Review B **73**, 235411 (2006).

-
- [27] N. M. R. Peres, A. H. C. Neto, and F. Guinea, *Conductance quantization in mesoscopic graphene*, Physical Review B **73**, 195411 (2006).
- [28] K. Nakada, M. Fujita, G. Dresselhaus, and M. S. Dresselhaus, *Edge state in graphene ribbons: Nanometer size effect and edge shape dependence*, Physical Review B **54**, 17954 (1996).
- [29] F. Sols, F. Guinea, and A. H. C. Neto, *Coulomb Blockade in Graphene Nanoribbons*, Physical Review Letters **99**, 166803 (2007).
- [30] A. R. Akhmerov and C. W. J. Beenakker, *Boundary conditions for Dirac fermions on a terminated honeycomb lattice*, Physical Review B **77**, 085423 (2008).
- [31] M. Y. Han, B. Özyilmaz, Y. Zhang, and P. Kim, *Energy Band-Gap Engineering of Graphene Nanoribbons*, Physical Review Letters **98**, 206805 (2007).
- [32] X. Li, X. Wang, L. Zhang, S. Lee, and H. Dai, *Chemically Derived, Ultrasmooth Graphene Nanoribbon Semiconductors*, Science **319**, 1229 (2008).
- [33] Z. Chen, Y. Lin, M. Rooks, and P. Avouris, *Graphene nano-ribbon electronics*, Physica E: Low-dimensional Systems and Nanostructures **40**, 228 (2007), ISSN 13869477.
- [34] F. Molitor, A. Jacobsen, C. Stampfer, J. Güttinger, T. Ihn, and K. Ensslin, *Transport gap in side-gated graphene constrictions*, Physical Review B **79**, 075426 (2009), ISSN 1098-0121.
- [35] C. Stampfer, J. Güttinger, S. Hellmüller, F. Molitor, K. Ensslin, and T. Ihn, *Energy Gaps in Etched Graphene Nanoribbons*, Physical Review Letters **102**, 056403 (2009), ISSN 0031-9007.
- [36] X. Liu, J. B. Oostinga, A. F. Morpurgo, and L. M. K. Vandersypen, *Electrostatic confinement of electrons in graphene nanoribbons*, Physical Review B **80**, 121407 (2009), arXiv:0812.4038.
- [37] K. Todd, H.-T. Chou, S. Amasha, and D. Goldhaber-Gordon, *Quantum Dot Behavior in Graphene Nanoconstrictions*, Nano Letters **9**, 416 (2009).
- [38] P. Gallagher, K. Todd, and D. G. Gordon, *Disorder-induced gap behavior in graphene nanoribbons*, Physical Review B **81**, 115409 (2010).
- [39] M. Y. Han, J. C. Brant, and P. Kim, *Electron Transport in Disordered Graphene Nanoribbons*, Physical Review Letters **104**, 056801 (2010).
- [40] J. B. Oostinga, B. Sacepe, M. F. Craciun, and A. F. Morpurgo, *Magneto-transport through graphene nano-ribbons* (2010), arXiv:1003.2994.

-
- [41] E. H. Hwang, S. Adam, and S. D. Sarma, *Carrier Transport in Two-Dimensional Graphene Layers*, Physical Review Letters **98**, 186806 (2007).
- [42] D. Gunlycke, D. A. Areshkin, and C. T. White, *Semiconducting graphene nanostrips with edge disorder*, Applied Physics Letters **90**, 142104 (2007).
- [43] Y. Yoon and J. Guo, *Effect of edge roughness in graphene nanoribbon transistors*, Applied Physics Letters **91**, 073103 (2007).
- [44] M. Evaldsson, I. V. Zozoulenko, H. Xu, and T. Heinzel, *Edge-disorder-induced Anderson localization and conduction gap in graphene nanoribbons*, Physical Review B **78**, 161407 (2008).
- [45] E. R. Mucciolo, A. H. C. Neto, and C. H. Lewenkopf, *Conductance quantization and transport gaps in disordered graphene nanoribbons*, Physical Review B **79**, 075407 (2009).
- [46] D. Basu, M. J. Gilbert, L. F. Register, S. K. Banerjee, and A. H. MacDonald, *Effect of edge roughness on electronic transport in graphene nanoribbon channel metal-oxide-semiconductor field-effect transistors*, Applied Physics Letters **92**, 042114 (2008).
- [47] D. Querlioz, Y. Apertet, A. Valentin, K. Huet, A. Bournel, S. G. Retailleau, and P. Dollfus, *Suppression of the orientation effects on bandgap in graphene nanoribbons in the presence of edge disorder*, Applied Physics Letters **92**, 042108 (2008).
- [48] R. Hanson, Ph.D. thesis, Technische Universiteit Delft (2005).
- [49] R. Hanson, L. P. Kouwenhoven, J. R. Petta, S. Tarucha, and L. M. K. Vandersypen, *Spins in few-electron quantum dots*, Reviews of Modern Physics **79**, 1217 (2007).
- [50] L. P. Kouwenhoven, D. G. Austing, and S. Tarucha, *Few-electron quantum dots*, Reports on Progress in Physics **64**, 701 (2001), ISSN 0034-4885.
- [51] L. P. Kouwenhoven, C. M. Marcus, P. L. McEuen, S. Tarucha, R. M. Westervelt, and N. S. Wingreen, *Electron transport in quantum dots* (Kluwer, Alphen aan den Rijn, the Netherlands, 1997).
- [52] W. G. van der Wiel, S. De Franceschi, J. M. Elzerman, T. Fujisawa, S. Tarucha, and L. P. Kouwenhoven, *Electron transport through double quantum dots*, Reviews of Modern Physics **75**, 1 (2002).
- [53] C. J. P. M. Harmans, *Mesoscopic physics, an introduction* (2003), lecture notes.
- [54] Y. Asano, *Magnetoconductance oscillations in ballistic semiconductor-superconductor junctions*, Physical Review B **61**, 1732 (2000).

-
- [55] Y. Asano and T. Yuito, *Effects of disorder on conductance oscillations in semiconductor-superconductor junctions in a magnetic field*, Physical Review B **62**, 7477 (2000).
- [56] N. M. Chtchelkatchev and I. S. Burmistrov, *Conductance oscillations with magnetic field of a two-dimensional electron gas-superconductor junction*, Physical Review B **75**, 214510 (2007).
- [57] Y. Takagaki, *Transport properties of semiconductor-superconductor junctions in quantizing magnetic fields*, Physical Review B **57**, 4009 (1998).
- [58] J. Eroms, D. Weiss, J. De Boeck, G. Borghs, and U. Zülicke, *Andreev Reflection at High Magnetic Fields: Evidence for Electron and Hole Transport in Edge States*, Physical Review Letters **95**, 107001 (2005).
- [59] T. D. Moore and D. A. Williams, *Andreev reflection at high magnetic fields*, Physical Review B **59**, 7308 (1999).
- [60] I. E. Batov, T. Schäpers, N. M. Chtchelkatchev, H. Hardtdegen, and A. V. Ustinov, *Andreev reflection and strongly enhanced magnetoresistance oscillations in $Ga_xIn_{1-x}As/InP$ heterostructures with superconducting contacts*, Physical Review B **76**, 115313 (2007).

Chapter 3

Fabrication

It is by now well known that the Geim group from Manchester University was the first to have managed to fabricate / create graphene. The initial approach that they took was rather logical: they took a large piece of graphite and tried to polish it thin [1]. With hind sight, I couldn't help wondering, would polishing really ever manage to reach exactly a single atomic layer of carbon? On the other hand, for decades people working on TEM have been using graphite samples for calibrations. To obtain thin enough graphite samples, they often peel graphite repeatedly with sticky tape, followed by dissolving in acetone. The thin graphite pieces are then scooped out with TEM grids. The Geim group developed a method of peeling graphene with sticky tape, and they pushed it to as far as a single atomic layer of graphene, that was never achieved before, and perhaps also never imagined before.

Around the same time of the Geim group's work, the McEuen group from Cornell University and the Kim group from Columbia University were working on the same topic. The McEuen group took a different approach than that of Geim's group, where they ultrasound graphite intensively until it breaks into very small and thin graphite pieces [2]. A similar approach was later taken much further by Dai's group from California to make ultra smooth graphene nanoribbons [3].

In this chapter, I describe the fabrication methods of graphene devices used in this work.

3.1 Fabricating graphene with mechanical exfoliation

Graphene is prepared in our group from mechanical exfoliation of graphite using sticky tapes. This is possible thanks to the properties of graphite. It is well known that a graphite crystal contains layers of graphene stacked together. Within each layer, atoms

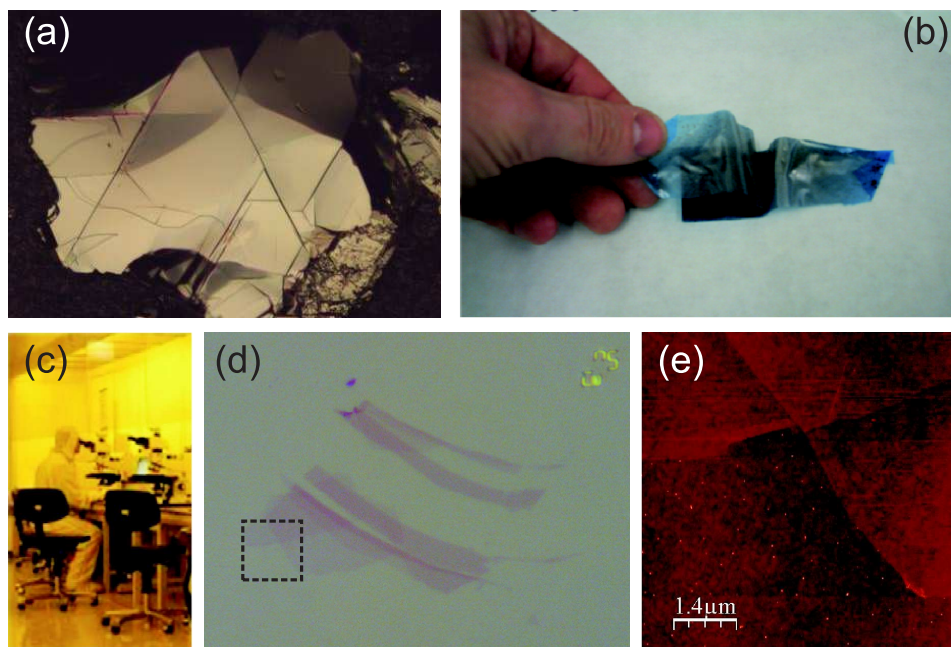


Figure 3.1: (a) Optical microscope image of a natural graphite grain of around $1.5 \text{ mm} \times 1.5 \text{ mm}$. (b) Repeated peeling of natural graphite with Nitto tape. (c) Inspection with optical microscope to find graphene. (d) Optical microscope image of a graphene flake. An optical marker is also visible in the upper right corner of the picture. The black dashed line indicate the region where the AFM image in (e) is taken. (e) Atomic force microscope (AFM) image of part of the graphene flake in (d).

are strongly bound by σ bonds and π bonds with a bond length 1.42 \AA . The inter-layer bonds consist of only the much weaker π bonds with a longer bond length 3.4 \AA . As a result, graphite layers can be separated with sticky tape. Graphite from different sources are used for fabricating graphene. Three commonly used graphite samples are natural graphite, HOPG, and Kish graphite. Natural graphite crystals are used in our group for preparing graphene samples.

The method of mechanical exfoliation includes three steps in principle: the repeated peeling of graphite with sticky tape; the cleaning of the Si substrate and the transfer of graphene from the sticky tape to Si substrates; finally, inspection with optical microscope to locate graphene. The processes are illustrated in Fig. 3.1 Below I will describe each step in detail.

Mechanical exfoliation

In the first step, we drop some graphite pieces on a sticky tape. The amount of graphite pieces should be proportional to the size of the sticky tape, the larger the

tape, the more graphite pieces. We then fold the tape such that the graphite pieces are enclosed in the "package", and unfold it again. After unfolding, one finds that each graphite piece now splits into two similar pieces, one on each side of the folds. These freshly cleaved surfaces are typically very shiny as shown in Fig. 3.1a. We repeat the folding and unfolding process a few more times, trying to use as much as possible the surface of the tape that is not yet covered with graphite, until the entire tape surface is covered by a relatively uniform density of graphite pieces. One can use a second or third tape if the density turns out to be too large for the first tape. If the density is too low, it's then better to start over with new graphite pieces and new tape.

From my experience, a good coverage (not too little, not too much) of graphite on the tape often gives a good yield of graphene flakes without too much graphite after transferring. It is however a pity that I couldn't quantify "good" coverage. Good news is that, most people can figure out the right amount of coverage after one or two trials. This is perhaps an evidence that the importance of quantification is sometimes over-emphasized.

Another empirical observation is that, somewhat higher yield of graphene is obtained using larger and thicker graphite pieces as the starting material.

Precleaning of Si substrates

In the second step, we prepare clean Si substrates with thermal oxide and transfer graphene / graphite from the tape to the substrate. Various cleaning recipes exist for cleaning Si wafers such as those described in ref. [4] and in the appendix C of this thesis. For the preparations of graphene samples, at least two consequences of a cleaning recipe need to be evaluated in order to decide whether it is suitable. (1) The cleaning recipe needs to be able to clean the surface of the wafers. The surface of most commercially available Si wafers with thermal oxides appears to be hydrophobic, despite the fact that SiO_2 is expected to be hydrophilic. This is due to various contaminants adsorbed on the surface of SiO_2 [5]. Such contaminants can be removed by exposing the wafers to an O_2 plasma¹, by cleaning in Piranha solutions, and by other means, as demonstrated by the hydrophilic surface after the treatments. Another source of contaminants on the surface is residues from resists used in lithography. Such residues can also be largely removed by ultrasonic cleaning in acetone and / or nitric acid HNO_3 . (2) The cleaning recipe needs not to increase the surface roughness of the SiO_2 . It is noticed that the mobility of the graphene transferred on a Si/ SiO_2 substrate is often influenced by the surface flatness and the quality of the thermal oxides, among others. For example cleaning in an O_2 plasma modifies the surface and the latter possibly influences the oxide quality as well, resulting in lower mobility graphene samples. We note that experimentally, special surface treatments are used intentionally in order to improve the sample mobility [6]. Other research is carried out to study the quality of graphene on different substrates [7–9] than the commonly used amorphous SiO_2 . The

¹ O_2 plasma treatment is also found to somewhat increase the yield of large size graphene flakes.

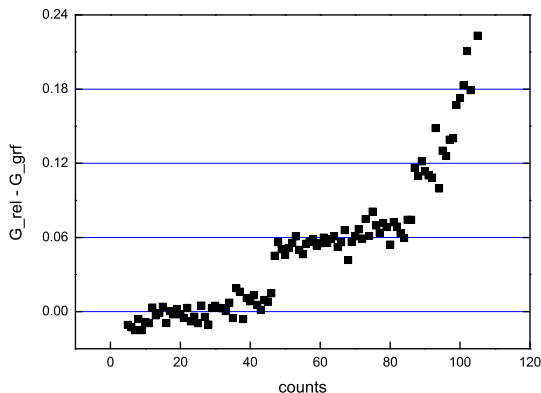


Figure 3.2: The relative contrast of graphene/graphite flakes, offset by the relative contrast of monolayer graphene.

two conditions mentioned above are often conflicting and in practice a compromise has to be made. In our work I mostly used a mild cleaning procedure such as ultrasonic cleaning in acetone followed by ultrasonic cleaning in HNO_3 .

To transfer graphene and / or graphite from the sticky tape to the freshly cleaned substrates, we press the substrates face down to the tape until it is "glued" to the tape. Using a higher pressure here often increases the coverage of graphite on the substrate and the yield of graphene. Notice that a large coverage of graphite is often not desirable for the subsequent device fabrication steps, therefore once again a compromising pressure is often used here. After several minutes, the substrate is "peeled" off from the sticky tape. We try to peel it off with as small an angle as possible. Notice that various other methods (sometimes more efficient methods) for transferring are used by different groups too.

Optical contrast of graphene

The last step is to locate graphene on the substrate. Monolayer graphene is visible under an ordinary optical microscope thanks to interference [10–12]. Fig. 3.1d shows an optical microscope image of a graphene flake. Different parts of the flake show different color contrast, indicating different thickness. Based on the optical contrast of a graphene flake, one can often determine whether it is monolayer or bilayer, etc, with rather high certainty. This is also illustrated in Fig. 3.2, where we plot the relative contrast of around 100 graphene flakes, offset by the contrast of single layer graphene. We see that the contrast of the first ~40 graphene flakes are rather constant, so is it with the next ~40 flakes. But the contrast of the second group of flakes are significantly higher

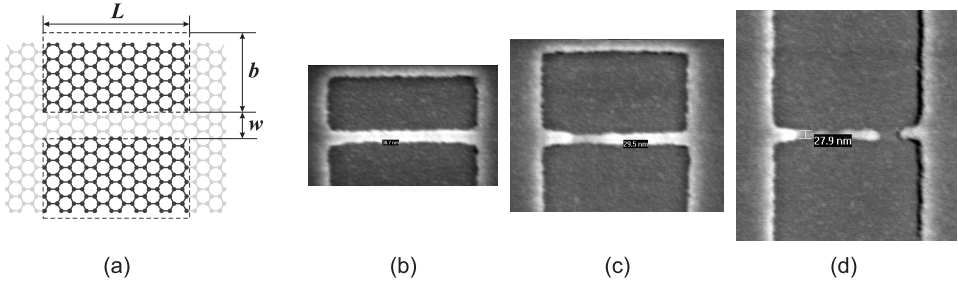


Figure 3.3: (a) Illustration of the PMMA etching mask for fabricating GNR. The width w and length L of the ribbon is labeled on the plot. The two boxes enclosed by the dashed the lines are exposed by the e-beam and removed after development. The size of each box is $L \times b$. (b, c, d) Scanning electron microscope (SEM) images of three PMMA etching masks. $L = 500$ nm and $w = 50$ nm by design for all three images, and b is designed to be 200 nm (b), 300 nm (c), and 100 nm (d). The resulting widths of the nanoribbons are measured to be 40 nm (b), 30 nm (c), and 28 nm (d).

than that of the first group, such that the optical contrast show a step like feature. In practice, we identify the first group of flakes as monolayer graphene and the second group as bilayer graphene. Quantum Hall effects measured on device based on several monolayer graphene flakes verify the identification. Only two steps are apparent in Fig. 3.2 probably because not enough samples of trilayer or thicker graphene flakes are included in the data (see ref. [13] for data up to trilayer graphene). The optical contrast thus offers an extremely convenient and efficient tool for quick identification and location of graphene flakes.

The graphene flakes prepared with the methods described above are subsequently used for fabricating various devices using standard e-beam lithography.

3.2 Graphene nanoribbon

The graphene nanoribbon (GNR) devices are fabricated by dry etching using suitable etching masks. Below we first describe the dry etching step, followed by a discussion on various etching masks used in this work.

For dry etching, we have used Ar plasma, O₂ plasma, or a mixture of Ar and O₂ for selectively removing graphene to form GNRs. All three kinds of plasma bombard the surface and physically remove graphene. In addition, O₂ plasma is also known to etch graphene chemically [14]. Therefore Ar plasma with very low gas pressure leads to highly anisotropic etching, and O₂ plasma was used to etch graphene also in the in-plane direction to obtain GNRs with narrower width than the lithography defined values [14].

For making narrow GNRs, we have used three different etching masks, PMMA, HSQ, and SiO₂. Below I discuss briefly the pros and cons of the three different masks.

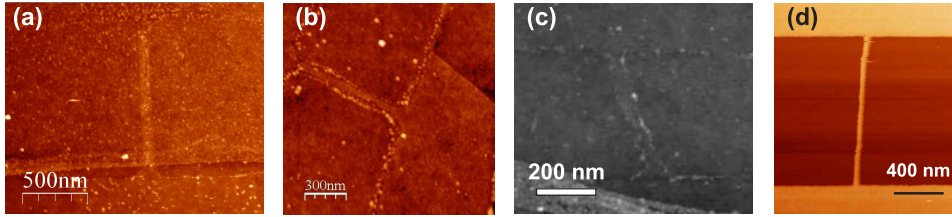


Figure 3.4: Atomic force microscope (AFM) images of four different graphene nanoribbons using PMMA (a, b, c) or HSQ (d) as etching masks.

When using PMMA as an etching mask with e-beam lithography, we first expose two boxes that are spaced by w by e-beam. Each box is of the size $L \times b$ (Fig. 3.3a). The PMMA within these two boxes is then removed by a developer and the graphene underneath is exposed. Subsequent exposure of the sample to a plasma removes the exposed graphene and forms a graphene nanoribbon device with length L and width w . The remaining PMMA can be (partially) lifted-off if required. (The lift-off is also discussed further below.) With appropriate recipe, we obtain GNR devices with width w down to 40 nm using this method.

Two major problems with PMMA as an etching mask is over-exposure and PMMA residue. The former problem is illustrated by Fig. 3.3b-d, where we tried to define GNRs of the same dimension with different exposure area. Notice that when b increases, the resulting ribbon width becomes narrower and narrower, until it breaks (Fig. 3.3d), presumably due to over-exposure as a result of the much larger dimension of b comparing to w . Consequently, using PMMA as an etching mask, we can obtain ribbons with $w \geq 60$ nm with close to 100% yield, $w = 40$ nm with around 10% yield, and $w < 40$ nm with almost zero yield.

The second problem with PMMA as an etching mask is that the PMMA after dry etching is often very difficult to lift-off, partially because it has been exposed to a relative hostile environment of plasma, even though only for a very short time (~ 20 s). Fig. 3.4 shows three GNR devices with different amount of resist residue. In Fig. 3.4a the ribbon is entirely covered by resist residue. For Fig. 3.4b most resist residue has been removed, except for around the area right next to the edges of the ribbon. This is the most common result in our work. Fig. 3.4c shows one of the cleanest devices around the ribbon region, but in the lower left corner of the the image, some large area of PMMA residue is still visible. The resist residues sitting on the ribbon are highly undesirable, especially when we need to cover the ribbon with a top gate during the subsequent fabrication steps, because the top gate action can be severely limited by the random resist residues between the gate dielectric and the GNR.

From the AFM images, we also notice that the edges of these laboratory GNRs are far from smooth, as discussed in section. 2.3.2.

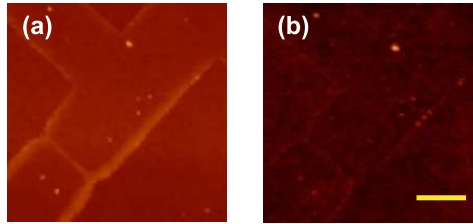


Figure 3.5: Atomic force microscope (AFM) images a GNR device before (a) and after (b) baking at 310 °C in Ar gas environment for two hours. The scale bar is 500 nm.

We have tried various chemicals in order to remove the PMMA residue, such as cleaning it using warm acetone, warm chloroform, THF and nitric acid. None of them could clean away the residue with 100% success. On the other hand, baking the sample at an elevated temperature (around 300 °C) in Ar or forming gas environment or in air often produces very clean samples. An example is shown in Fig. 3.5. But sometimes the graphene flakes disappear after baking at such temperature / environment.

In a second method in order to fabricate ribbons narrower than 40 nm, we use a different resist, HSQ. HSQ is a high resolution negative resist, that turns partially into SiO₂ after exposure to e-beam or to high temperature [15]. GNRs with width less than 20 nm can be fabricated with HSQ as an etching mask. Fig. 3.4d shows an AFM image of one GNR covered with HSQ.

In a third approach, we use evaporated SiO₂ as an etching mask. First we pattern PMMA. In contrast to the case described in Fig. 3.3a, here the exposed area is reversed, i.e. the part that will become the GNR is exposed. SiO₂ is evaporated after development, followed by lift-off. A ribbon is fabricated after the sample is subsequently exposed to plasma.

In this case lift-off is easy perhaps because PMMA was not exposed to plasma. Over-exposure is also not a problem here as only a very thin line is exposed instead of two large, closely spaced areas. Thin SiO₂ lines (ribbons) as narrow as 20 nm can be reliably fabricated with this method. One example of such a device is shown in chapter 6.

The major problem with using HSQ or SiO₂ as etching masks is that it is difficult to remove the masks except for HF, which attacks also the substrate and is not always desirable.

3.3 Top gates

In this section I summarize the fabrication methods that we used for making the top gates (TG). The main focus is a reliable dielectric that ensures low leakage and stable gate action. In addition, we also try to fabricate very narrow top gates.

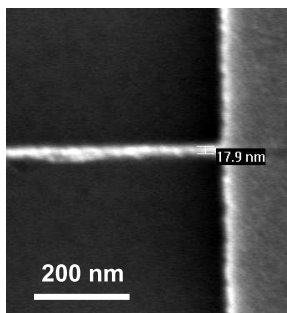


Figure 3.6: SEM image of a narrow top gate.

The fabrication of very narrow gates is analogous to the fabrication of very narrow ribbons using SiO_2 as etching masks described in the previous section. Top gates as narrow as 20 nm can be achieved relatively easily using standard e-beam lithography recipes. Fig. 3.6 shows a SEM image of one narrow top gate.

To fabricate TGs on graphene, one needs to first deposit a dielectric layer that electrically isolates graphene from the TG metal, followed by a metal layer. For the dielectric, we have tested two different oxides in our work, aluminum oxide formed by oxidation of Al films and directly evaporated silicon oxide.

For the Al_2O_3 , we evaporate 2 nm Al, followed by oxidation in O_2 environment at room temperature for around 20 minutes. 1-2 nm oxides is expected during this process. The procedure was repeated three times. We obtained in the end 20 nm Al_2O_3 , thicker than the expected 10 nm. The Al_2O_3 fabricated this way in our lab did not provide electrical isolation and the TG was leaking at room temperature.

For the SiO_2 , we evaporate more than 10 nm SiO_2 directly on graphene, followed by evaporating a metal layer without breaking the vacuum. The resulting top gates mostly show no leakage current up to 3-4 V for 10 nm oxide. The dielectric thinner than 4 nm is found to be leaking. Fig. 3.7a shows the measurement result from a TG with 20 nm SiO_2 , where no leakage current is observed up to -6 V.

To fabricate TGs on GNRs, the residues from the etching masks also play a role. As already mentioned before, with PMMA etching masks, large amount of residue can give rise to very switchy gate response. For the case with HSQ etching masks, we tried to fabricate TGs directly on HSQ without removing the masks. Fig. 3.7b shows the leakage current through such a structure. The TG starts to leak at around ± 2 V. Even below 2 V, the leakage current is a few times higher than that of without HSQ. For the case with SiO_2 etching masks, we also directly evaporate the TG dielectric on the SiO_2 etching mask such that the etching mask acts as part of the dielectric (see also chapter 6 of this thesis). The resulting TG leakage current is on average very small. For 11 out of 12 TGs tested, the leakage current is around 10 pA at ± 4 V on the TG at $T = 4$ K. (The last TG

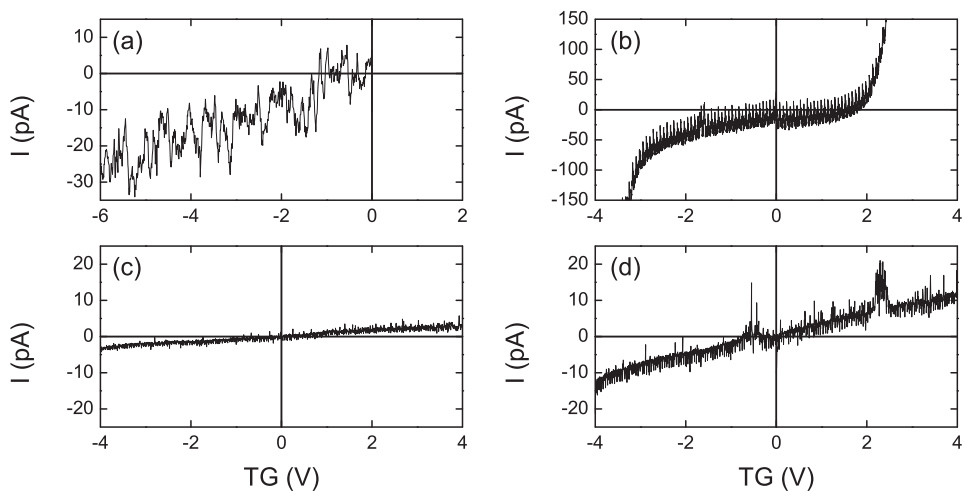


Figure 3.7: Leakage current through different top gate devices. (a) TG is fabricated directly on top of a bulk graphene without the etching step. The TG dielectric SiO_2 is 20 nm thick. (b) A TG fabricated on a GNR that is covered by 20 nm HSQ etching mask [15]. The TG dielectric SiO_2 is 10 nm thick. (c, d) TGs fabricated on a GNR that is covered by 15 nm SiO_2 etching mask. The TG dielectric is 5 nm thick. All four graphs were measured at $T = 50$ mK. Note the scale of the vertical axis for (b) is different from others.

shows increased current at around 3 V on the TG.) When the devices were cooled down further to 50 mK, most top gates show large amplitude noise at several voltages. An example is shown in Fig. 3.7d. Other gates remain stable as shown in Fig. 3.7c.

The quality of the TGs that uses the SiO_2 etching masks as part of the dielectric is less controlled than that of the TGs without the etching masks (i.e. the dielectric and TG metal are evaporated sequentially without breaking the vacuum), suggesting that the quality of the SiO_2 etching mask might be worse than the as-evaporated SiO_2 . The reason for this could be that the etching mask has been (1) exposed to air; (2) exposed to e-beam during lithography; (3) exposed to plasma during dry etching.

References

- [1] K. S. Novoselov, A. K. Geim, S. V. Morozov, D. Jiang, Y. Zhang, S. V. Dubonos, I. V. Grigorieva, and A. A. Firsov, *Electric Field Effect in Atomically Thin Carbon Films*, *Science* **306**, 666 (2004).
- [2] J. S. Bunch, Y. Yaish, M. Brink, K. Bolotin, and P. L. McEuen, *Coulomb Oscillations and Hall Effect in Quasi-2D Graphite Quantum Dots*, *Nano Letters* **5**, 287 (2005).

-
- [3] X. Li, X. Wang, L. Zhang, S. Lee, and H. Dai, *Chemically Derived, Ultrasmooth Graphene Nanoribbon Semiconductors*, *Science* **319**, 1229 (2008).
- [4] *Wet-chemical etching and cleaning of silicon* (2003), URL <http://www.virginiasemi.com/pdf/siliconetchingandcleaning.pdf>.
- [5] T. Zijlstra, private communication.
- [6] M. Lafkioti, B. Krauss, T. Lohmann, U. Zschieschang, H. Klauk, K. von Klitzing, and J. H. Smet, *Graphene on a Hydrophobic Substrate: Doping Reduction and Hysteresis Suppression under Ambient Conditions*, *Nano Letters* **10**, 1149 (2010).
- [7] A. Giesbers, U. Zeitler, S. Neubeck, F. Freitag, K. Novoselov, and J. Maan, *Nanolithography and manipulation of graphene using an atomic force microscope*, *Solid State Communications* **147**, 366 (2008), ISSN 00381098.
- [8] U. Stöberl, U. Wurstbauer, W. Wegscheider, D. Weiss, and J. Eroms, *Morphology and flexibility of graphene and few-layer graphene on various substrates*, *Applied Physics Letters* **93**, 051906 (2008).
- [9] L. A. Ponomarenko, R. Yang, T. M. Mohiuddin, M. I. Katsnelson, K. S. Novoselov, S. V. Morozov, A. A. Zhukov, F. Schedin, E. W. Hill, and A. K. Geim, *Effect of a High-k Environment on Charge Carrier Mobility in Graphene*, *Physical Review Letters* **102**, 206603 (2009).
- [10] D. S. L. Abergel, A. Russell, and V. I. Fal'ko, *Visibility of graphene flakes on a dielectric substrate*, *Appl. Phys. Lett.* **91**, 063125 (2007).
- [11] P. Blake, E. W. Hill, A. H. Castro Neto, K. S. Novoselov, D. Jiang, R. Yang, T. J. Booth, and A. K. Geim, *Making graphene visible*, *Appl. Phys. Lett.* **91**, 063124 (2007).
- [12] J. B. Oostinga, H. B. Heersche, X. Liu, A. F. Morpurgo, and L. M. K. Vandersypen, *Gate-induced insulating state in bilayer graphene devices*, *Nature Materials* **7**, 151 (2007), ISSN 1476-1122.
- [13] M. F. Craciun, S. Russo, M. Yamamoto, J. B. Oostinga, A. F. Morpurgo, and S. Tarucha, *Trilayer graphene is a semimetal with a gate-tunable band overlap*, *Nature Nanotechnology* **4**, 383 (2009), ISSN 1748-3387.
- [14] L. A. Ponomarenko, F. Schedin, M. I. Katsnelson, R. Yang, E. W. Hill, K. S. Novoselov, and A. K. Geim, *Chaotic Dirac Billiard in Graphene Quantum Dots*, *Science* **320**, 356 (2008).
- [15] D. Hug, *Transport measurement on graphene nanoribbon* (2009), master thesis.

Chapter 4

Gate induced insulating state in bilayer graphene devices

The potential of graphene-based materials consisting of one or a few layers of gra-phite for integrated electronics originates from the large room-temperature carrier mobility in these systems ($\sim 10,000 \text{ cm}^2/\text{Vs}$). However, the realization of electronic devices such as field-effect transistors will require controlling and even switching off the electrical conductivity by means of gate electrodes, which is made difficult by the absence of a bandgap in the intrinsic material. Here, we demonstrate the controlled induction of an insulating state – with large suppression of the conductivity – in bilayer graphene, by using a double-gate device configuration that enables an electric field to be applied perpendicular to the plane. The dependence of the resistance on temperature and electric field, and the absence of any effect in a single-layer device, strongly suggest that the gate-induced insulating state originates from the recently predicted opening of a bandgap between valence and conduction bands.

The contents of this chapter have been published in *Nature Materials*:

J. B. Oostinga, H. B. Heersche, X. L. Liu, A. F. Morpurgo, L. M. K. Vandersypen, *Gate-induced insulating state in bilayer graphene devices*. *Nature Materials* **7** (2), 151-157 (2008).

4.1 Introduction

Graphene systems, consisting of one or a few crystalline monolayers of carbon atoms, stand out because of their unusual electronic properties and their potential for applications in nano-electronics [1–5]. Carrier mobility values as high as $10,000 \text{ cm}^2/\text{Vs}$ at room temperature – ten times higher than in silicon – are routinely obtained in these materials, without the need for sophisticated preparation techniques [1]. Both the high mobility and the possibility of low-cost mass production provide a strong drive to explore the use of graphene for future high-speed integrated electronic circuits. To develop such ‘graphene-based electronics’, however, several problems need to be overcome. Perhaps the most important obstacle is the absence of an energy gap separating the valence and conduction bands of graphene – graphene is a zero-gap semiconductor [6]. As a consequence, electrical conduction cannot be switched off using control voltages [7], which is essential for the operation of conventional transistors. It was recently shown that conduction can be switched off by patterning single-layer graphene into narrow ribbons [8]. Here, we demonstrate that we can produce an insulating state and switch off electrical conduction in a bilayer graphene device, simply by applying control voltages to two on-chip gate electrodes.

4.2 The low-energy bandstructure of single- and bilayer graphene

Our strategy is motivated by recent theoretical work that discusses how a band-gap can be opened in single- and bilayer graphene [9, 10]. To understand the physical mechanisms underlying these predictions, we consider the basic electronic properties of graphene-based materials in some detail. Monolayer graphene has a honeycomb lattice structure with a unit cell consisting of two atoms – normally referred to as A and B atoms (Fig. 3.1a). The Hamiltonian that describes the electronic properties of graphene near the Fermi level can be approximated as [6, 11]

$$H = \begin{pmatrix} \Delta & \hbar v_F(k_x - i k_y) \\ \hbar v_F(k_x + i k_y) & -\Delta \end{pmatrix}, \quad (4.1)$$

where k is the momentum and v_F is the Fermi velocity. This operator acts on spinors $\psi = (\varphi_A, \varphi_B)^T$, where φ_A and φ_B are the amplitudes of the wavefunction on sublattices A and B, and Δ is the on-site energy difference between the two sublattices. Normally $\Delta = 0$ and this Hamiltonian results in the Dirac-like linear dispersion relation $E = \pm \hbar v_F |k|$ (Fig. 4.1a). The positive and negative solutions, which correspond to conduction and valence bands respectively, meet at $k = 0$, implying the absence of a bandgap. To open a gap, the inversion symmetry in the graphene plane must be broken by making $\Delta \neq 0$. In this case, the low-energy Hamiltonian (eqn. 4.1) leads to a

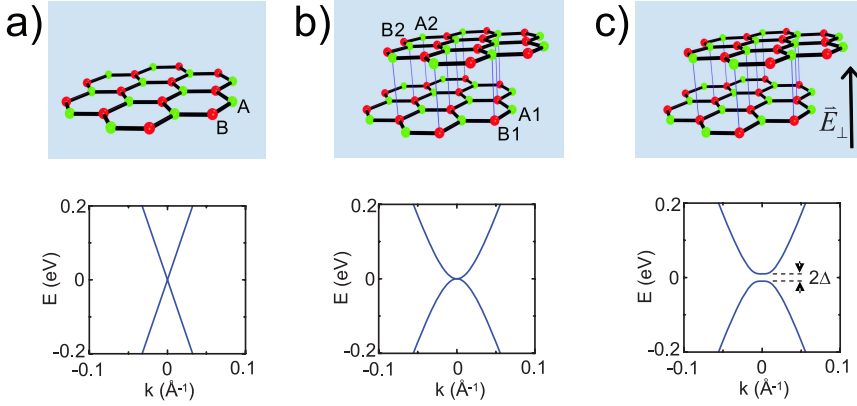


Figure 4.1: Band structure of graphene. (a,b), Schematic diagrams of the lattice structure of monolayer (a) and bilayer (b) graphene. The light gray and dark gray coloured lattice sites indicate the A (A1/A2) and B (B1/B2) atoms of monolayer (bilayer) graphene, respectively. The diagrams represent the calculated energy dispersion relations in the low-energy regime, and show that monolayer and bilayer graphene are zero-gap semiconductors (for bilayer graphene, a pair of higher-energy bands is also present, not shown in the diagram). (c), When an electric field (\vec{E}_\perp) is applied perpendicular to the bilayer, a bandgap is opened in bilayer graphene, whose size (2Δ) is tunable by the electric field.

gapped dispersion relation $E(k) = \pm \sqrt{\Delta^2 + (\hbar v_F k)^2}$ [2]. This inversion symmetry breaking can in principle be implemented experimentally. For instance, we can imagine placing graphene onto a boron nitride (BN) substrate that has the same honeycomb lattice structure and comparable lattice spacing, so that the A and B atoms experience different on-site energies [9]. In practice, however, the technological challenges that need to be met to implement such a strategy are highly non-trivial.

In bilayer graphene, in contrast, a conceptually similar strategy is within technological reach. Bilayer graphene consists of two monolayers stacked as in natural graphite (Fig. 4.1b). This so-called Bernal stacking yields a unit cell of four atoms (one atom of each of the sublattices A1, B1, A2 and B2) resulting in four electronic bands. Only two of these bands are relevant at low energy; they can be described by the effective Hamiltonian [12]

$$H = \begin{pmatrix} \Delta & -\frac{\hbar^2}{2m}(k_x - ik_y)^2 \\ -\frac{\hbar^2}{2m}(k_x + ik_y)^2 & -\Delta \end{pmatrix}. \quad (4.2)$$

This operator has a structure similar to that of eqn. 4.1 and, as for the monolayer, it also leads to a spectrum with zero gap between valence and conduction bands when $\Delta = 0$, but now with a quadratic dispersion relation ($E = \pm \hbar^2 k^2 / 2m$; Fig. 4.1b). Furthermore, and essential for our purposes, the operator (eqn. 4.2) acts on spinors $\psi = (\varphi_{A1}, \varphi_{B2})^T$, which contain the amplitude of the wavefunction on atoms A1 and B2 that are located

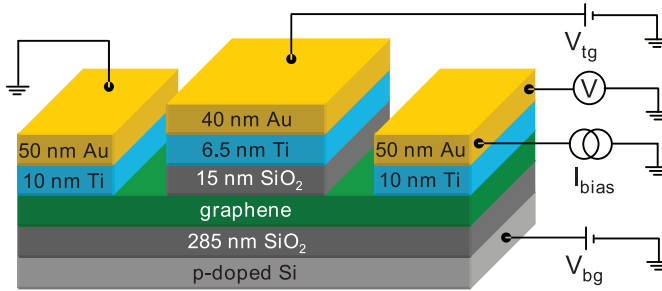


Figure 4.2: Schematic diagram of a double-gated graphene device as used in our investigations. Both the Fermi level in the graphene (bi)layer and the perpendicular electric field are controllable by means of the voltages applied to the back-gate, V_{bg} , and to the top-gate, V_{tg} . We study the resistivity of the graphene (bi)layer as a function of both gate voltages by applying a current bias (I) and measuring the resulting voltage across the device, V . Note the different SiO_2 thicknesses of the dielectric layers for the top- and back-gates.

in the two different layers. This makes it possible to control the difference between the on-site energy of A1 and B2 electrostatically, simply by applying a sufficiently strong electric field E perpendicular to the carbon atom planes. In the presence of such an electric field, a gap of size 2Δ opens between conduction and valence bands [10, 12, 13] (Fig. 4.1c). Indeed, a bandgap originating from this mechanism has recently been observed in angle-resolved photoemission spectroscopy experiments on a chemically doped graphene bilayer, in which the electric field is associated with the charge transfer from the dopants to the carbon atoms [14] (see also ref. [15]). Here, we use a double-gate device configuration to impose a perpendicular electric field onto a graphene bilayer, which enables us to demonstrate the controlled transition from a zero-gap semiconductor to an insulator, by simply adjusting the voltages applied to the two gate electrodes.

4.3 Fabrication of double-gated graphene devices

Fig. 4.2 shows a schematic of our device layout. It consists of monolayer or bilayer graphene sandwiched between two gate electrodes, the top gate and the back gate. The graphene is also connected to metallic leads. These double-gated structures enable simultaneous and independent control of the charge density in the system (that is, the position of the Fermi level) and of the electric field perpendicular to the graphene layer. In a single layer, the presence of a perpendicular field is not expected to affect the transport properties: the conductivity of the device should never become smaller than a minimum value of the order of $4e^2/h$, irrespective of the applied gate voltages [2]. In a bilayer, on the contrary, a large applied field results in a different electrostatic potential in the two layers, which, according to theory, should cause a bandgap to open. If the

Fermi level is maintained in the gap (that is, the device is operated near the charge-neutrality point), this should result in an insulating temperature dependence of the conductivity, dropping to well below $4e^2/h$ at low temperature. A unique signature of this effect is that the decrease in conductivity with lowering temperature becomes more pronounced for larger applied electric field values. This possibility to controllably induce an insulating state, which is crucial for switching devices, was missing in earlier experiments on graphene bilayers [14, 15] where the gap and the carrier density could not be gate-controlled independently.

The fabrication of double-gated graphene devices is similar to what has been described elsewhere [1], and relies on micromechanical cleaving of natural graphite. The flakes used in the experiments were selected under an optical microscope and identified as single- and double-layer graphene, respectively, on the basis of their optical contrast (see chapter 3 a similar method is used as previously demonstrated in refs [16, 17]). Contact to the flakes was made by means of electron-beam lithography, electron-beam evaporation of a Ti/Au bilayer (10/50 nm) and lift-off. The top-gate insulating layer and electrodes were defined subsequently, by electron-beam evaporation of a SiO₂ layer (15 nm) followed by deposition of a Ti/Au bilayer (6.5/40 nm), without breaking the vacuum. The comparison between single- and double-layer graphene devices is useful not only to illustrate the profound difference between them and to identify the mechanism responsible for the gate-induced insulating state, but also to rule out possible spurious effects originating from the device fabrication (for example, damage to the graphene layers or disorder introduced by the deposition of the SiO₂ gate dielectric).

4.4 Characterization of single-layer and bilayer graphene devices

We now proceed to discuss the systematic transport measurements that we have carried out, starting with the single-layer device shown in Fig. 4.3a. Figure 4.3b,c shows the resistance measured as a function of the voltage applied to one of the gates, with the other gate at a constant potential as indicated (we extract a carrier mobility of $\sim 3,000$ cm²/Vs, similar to the mobility of an ungated device on the same flake). Irrespective of which gate voltage is kept constant, we always observe a peak in resistance characteristic of the behaviour of few-layer graphene and hereafter referred to as the 'charge-neutrality peak' (to be precise, we are measuring a device comprising regions of different carrier density, n_1 - n_2 - n_1 ; at the resistance maximum, $n_2 = 0$ only). The position of the charge-neutrality peak when sweeping one gate shifts linearly with the voltage applied to the other gate. Irrespective of the gate configuration, the height of the resistance peak remains approximately constant. From the top-gate dimensions, we can estimate a minimum conductivity value close to $4e^2/h$ (the part of the flake that is not covered by the top-gate also contributes to the resistance, but given the dimensions, this increases

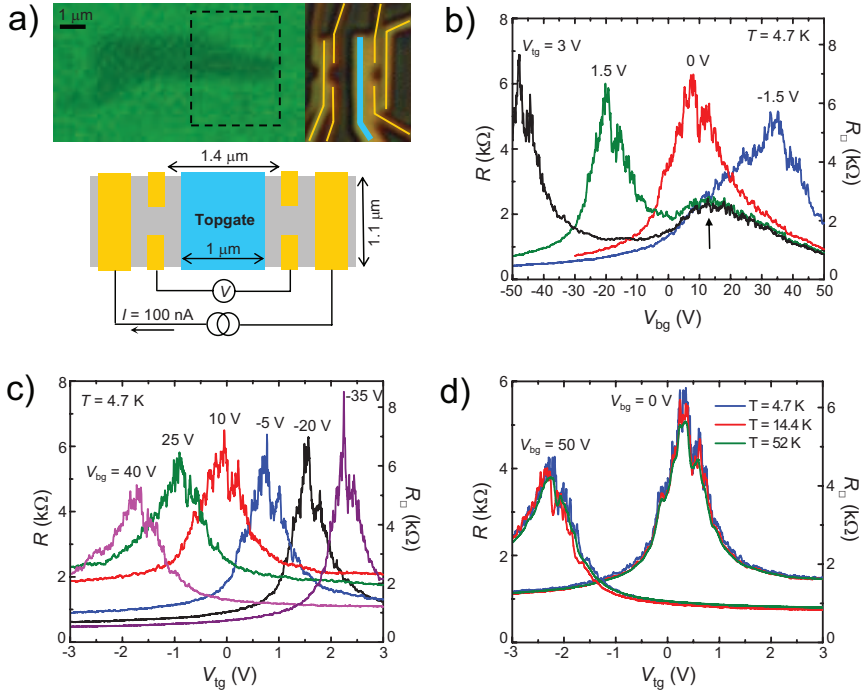


Figure 4.3: Gate voltage and temperature dependence of transport through monolayer graphene. (a) Optical microscope images of a single-layer flake (left) and of the double-gated device fabricated on this flake (right). The yellow lines indicate metal contacts to the flake, and the blue line corresponds to the top-gate. The schematic diagram of the four-probe device configuration is also shown. (b) Resistance versus back-gate voltage measured for different fixed values of the top-gate voltage showing an approximately gate voltage independent height of the charge-neutrality peak (the right axis gives an estimation of the square resistance, neglecting the contributions from the region without the top-gate and any p - n junctions to the measured resistance). The aperiodic fluctuations present near the charge-neutrality peak are reproducible and are due to quantum interference. The smaller extra peak (indicated by the arrow) is the charge-neutrality peak originating from the part of the flake that is not covered by the top-gate. (c) Resistance versus top-gate voltage measured for different fixed values of back-gate voltage. Again, the height of the charge-neutrality peak is nearly gate voltage independent. The difference in the magnitude of the voltage applied to top- and back-gates (b,c) originates from the different SiO_2 thicknesses separating the two gates from the graphene flake. (d) Temperature dependence of the resistance versus top-gate voltage, measured for two different back-gate voltages. Irrespective of the gate voltage configuration, the height of the charge-neutrality peak is independent of temperature in the range 4.7–52 K.

the conductivity estimate by at most a factor of 1.4). This is typical of graphene at the charge-neutrality point, which indicates that the device fabrication and the deposition of the top-gate dielectric have not resulted in substantial damage to the material. Note also that depending on the values of the voltages applied to both gates, $p-n$ junctions are formed near the interfaces between the region covered by the top-gate and both uncovered regions [18]. Such $p-n$ junctions may be the origin of the weak asymmetry seen in many of the gate sweeps in Fig. 4.3b,c. However, near the charge-neutrality point, we expect $p-n$ junctions to give only a small contribution to the measured resistance. Finally, Fig. 4.3d shows that the gate voltage dependence of the resistance is not affected by varying the temperature between 4 and 50 K, apart from reproducible conductance fluctuations that increase in magnitude as the temperature is lowered. These observations are consistent with the expected behaviour of electrical transport through graphene monolayers [2, 18–20].

The behaviour of the double-gated graphene bilayer device (Fig. 4.4a) is strikingly different. Figure 4.4b,c shows the (square) resistance of bilayer graphene as a function of the back-gate and top-gate voltages (the carrier mobility is $\sim 1,000 \text{ cm}^2/\text{Vs}$, again similar to an ungated device on the same flake). Similarly to the monolayer, the position of the charge-neutrality peak shifts linearly with the respective gate voltages. Contrary to the monolayer, the charge-neutrality peaks are nearly perfectly symmetric, ruling out the possibility that the formation of $p-n$ junctions gives a dominant contribution to the measured resistance. More importantly, the maximum resistance value now depends on the configuration of gate voltages. Specifically, when the voltage applied to both gates is close to 0 V, the height of the charge-neutrality peak corresponds to a conductivity of the order of $4e^2/h$, which is typical for zero-gap bilayers [5] (again we rely on the fact that near the charge-neutrality peak the region under the top-gate gives the largest contribution to the resistance). However, as the top- and back-gates are biased with opposite voltages of increasing magnitude, the height of the charge-neutrality peak exhibits a pronounced rise. In addition, the temperature dependence observed in the bilayer device is markedly different from that measured in the single-layer device (Fig. 4.4d). For small gate voltages, the resistance near the charge-neutrality peak is essentially temperature independent, characteristic of a zero-gap semiconductor. When the difference in top-gate and back-gate voltage is increased, however, the maximum resistance value also increases as the temperature is lowered. The observation of a conductivity much smaller than $4e^2/h$ exhibiting an insulating temperature dependence for oppositely biased gate electrodes is what we would expect qualitatively in a bilayer graphene device.

4.5 Transport in the insulating regime

To confirm that in the double-gated bilayer device large differences in voltage between the top- and back-gate do lead to an insulating state, we have carried out measurements

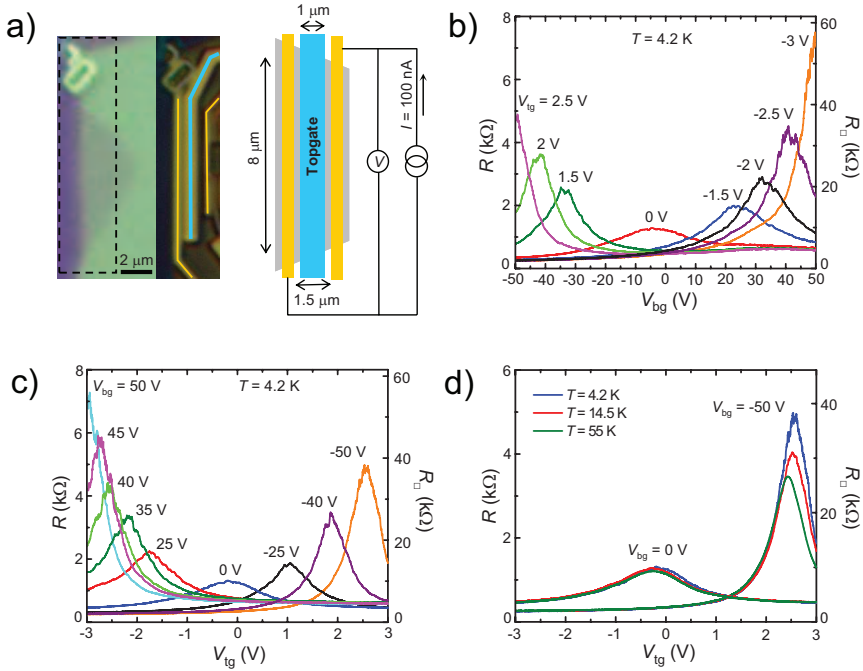


Figure 4.4: Gate voltage and temperature-dependent transport through bilayer graphene. (a) Optical microscope images of a double-layer flake (left) and of the double-gated device fabricated on this flake (right). The light gray stripes represent metal contacts and the dark gray stripe represents the top-gate electrode. The two-probe measurement configuration is shown in the schematic diagram (the measured resistance thus includes the contact resistance, which is smaller than $\sim 250 \Omega$). (b) Resistance versus back-gate voltage measured for different fixed values of the top-gate voltage (the right axis gives the square resistance, again assuming that the region under the top-gate dominates the measured resistance; this assumption is valid near the charge-neutrality peak where the resistance of the region with top-gate is relatively large). The height of the charge-neutrality peak systematically increases when both gates are biased with increasingly large opposite voltages. (c) Resistance versus top-gate voltage measured for different fixed back-gate voltages showing a similar gate voltage dependence of the height of the charge-neutrality peak. (d) Temperature dependence of the resistance versus top-gate voltage measured for two different values of back-gate voltage. When the voltage difference between both gates is small, the height of the charge-neutrality peak is not affected by temperature in the range 4.2–55 K. However, a clear temperature dependence is observed in this same range when both gates are biased with large opposite voltages.

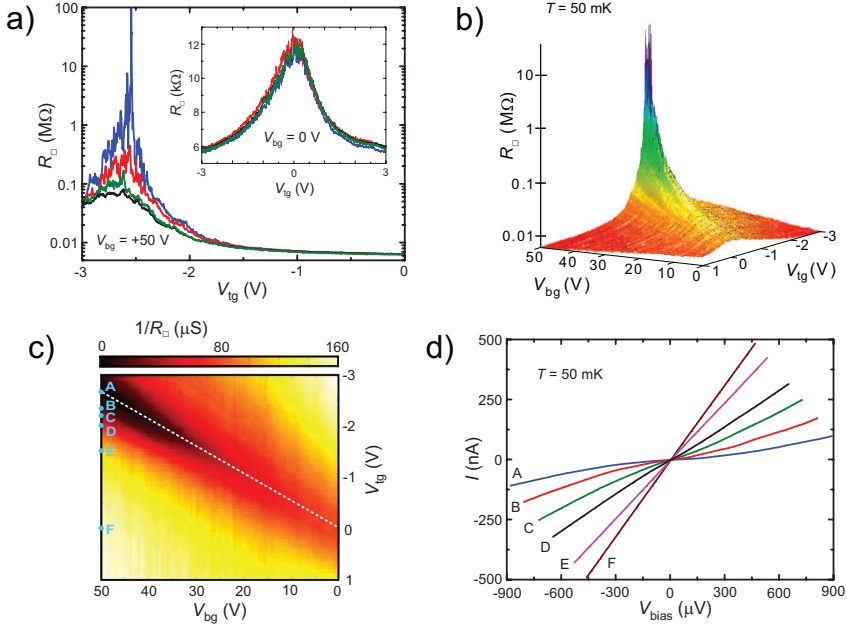


Figure 4.5: Gate-induced insulating state in the bilayer graphene device. (a) Square resistance as a function of top-gate voltage measured at different temperatures: $T = 55$ mK (dark gray line), $T = 270$ mK (gray line), $T = 600$ mK (light gray line) and $T = 1,200$ mK (black line) (the back-gate voltage is kept fixed at $V_{bg} = +50$ V). Here, the square resistance is plotted, because near the charge-neutrality peak the resistance is almost completely dominated by the region under the top-gate. A pronounced temperature dependence is observed when the top- and back-gates are biased asymmetrically; when both gates are symmetrically biased no temperature dependence is observed (see inset). (b) Three-dimensional plot of the square resistance as a function of both top- and back-gate voltage at $T = 50$ mK, showing a sharp rise of the height of the charge-neutrality peak with electric field. (c) Colour plot of the same data, showing that the position of the charge-neutrality peak shifts linearly with both gate voltages. The dark-gray region corresponds to voltage configurations where an insulating state is observed. (d) $I - V$ characteristics measured at different gate voltage configurations (the letters correspond to the letters in (c), which indicate both gate voltages). The data in (a, b, c) were taken with lock-in detection, using a zero-voltage bias with a $5 \mu\text{V}$ excitation voltage modulated at 17 Hz. The data in (d) were measured with a DC voltage bias. Note that the plotted voltage bias is corrected for the internal resistance ($1.1 \text{ k}\Omega$) of the current measurement unit used in the experiment.

in a dilution refrigerator, in the temperature range between 50 mK and 1.2 K, where the increase in resistance with lowering temperature should be more pronounced. Indeed, Fig. 4.5a (note the logarithmic scale) shows that when the top- and back-gates are biased asymmetrically, a very strong temperature dependence of the square resistance is observed near the charge-neutrality peak, reaching values between 10 and 100 M Ω at 55 mK. This is in stark contrast to the case of small gate voltages (Fig. 4.5a inset), for which a temperature independent resistance near the charge-neutrality peak – corresponding to a conductivity of approximately $4e^2/h$ – persists down to the lowest temperature. The full dependence of the square resistance measured at 50 mK as function of the voltage applied to both gate electrodes is shown in Fig. 4.5b, c, from which the very fast increase in resistance near the charge-neutrality peak with increasing the electric field applied perpendicular to the layer is apparent. According to the expectations, the region of high resistance scales linearly with both top- and back-gate voltage (see the white dotted line in Fig. 4.5c) as it is required to maintain charge neutrality in the graphene bilayer. In addition, we have also measured the $I - V$ characteristics of the device for different top- and back-gate voltage configurations (Fig. 4.5d) and observed that they evolve from exhibiting a linear ohmic behaviour far from the charge-neutrality peak, to a pronounced nonlinear behaviour near the charge-neutrality peak.

Finally, we discuss more quantitatively the insulating temperature dependence of the resistance that we observe for large oppositely biased gates. In an ideal defect-free insulator, thermally activated transport is expected, whereby the maximum resistance, R , varies with temperature as $R(T) \propto \exp(E_a/kT)$, where k is Boltzmann's constant and E_a is the activation energy, corresponding to half the bandgap. Our data, however, do not exhibit such a simple thermal activation behaviour (Fig. 4.6a). Below approximately $T = 5$ K, and at the highest applied electric fields, they are much better described by $R(T) \propto \exp(T_0/T)^{1/3}$, as seen in Fig. 4.6b, with fitted values of T_0 of ~ 0.5 - 0.8 K (note that between 5 and 55 K the resistance drops more rapidly with increasing temperature, but the range is too small to deduce an accurate value for the activation energy). Qualitatively, an $n = 1/3$ exponent is expected for transport in two dimensions of non-interacting carriers via variable-range hopping in insulating materials where transport is mediated by localized impurity sites that are present inside a gap [21, 22]. Such localized states have been predicted theoretically in the case of disordered bilayer graphene [23], but drawing quantitative conclusions as to the properties of these states, for example, their density of states, spatial extension, and so on, is not straightforward from our measurements. For smaller applied perpendicular electric fields, the fitted exponent becomes smaller than $1/3$ and decreases towards zero (see inset of Fig. 4.6b), and the fitted value of T_0 also decreases. This indicates clearly that the insulating temperature dependence of the resistance that we measure becomes stronger when the applied perpendicular electric field is higher.

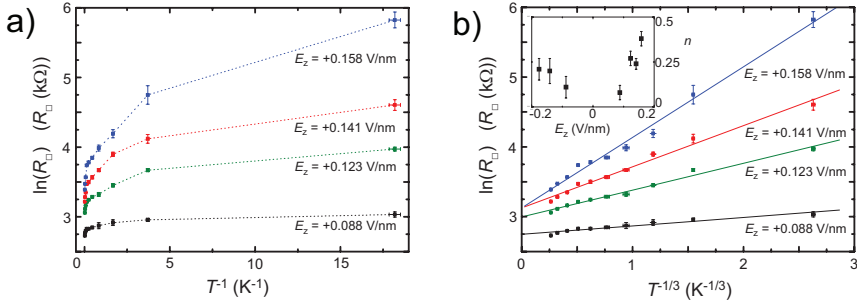


Figure 4.6: Thermally activated hopping transport in biased bilayer graphene. (a) Logarithm of the square resistance at the charge-neutrality peak versus inverse temperature, for different perpendicular electric fields ($E_{\perp} = (V_{bg} - V_{tg}) / (d_{bg} + d_{tg})$), where d_{bg} and d_{tg} are the thicknesses of the back- and top-gate oxides). These plots clearly show sublinear behaviour in the temperature range from 55 mK to 55 K (the dotted lines are a guide to the eye), implying that the data cannot be described by $R(T) \propto \exp(E_g/kT)$. b, Logarithm of the square resistance of the charge-neutrality peak as function of $T^{-1/3}$ for different perpendicular electric fields in the temperature range from 55 mK to 55 K. The linear fits to the data (solid lines) show that, at the highest fields, the data are well described by $R(T) \propto \exp(T_0/T)^{1/3}$. At lower fields, the fitted exponent, n , is smaller than $1/3$ (see inset; the error bars reflect the standard deviation of the fitted values).

4.6 Conclusions and discussion

We conclude that the data unambiguously show the occurrence of an insulating state in bilayer graphene in the presence of a perpendicular electric field, which has not been reported earlier. Our observation that the insulating state occurs only in bilayers and not in monolayers, and that the increase in resistance with lowering temperature is more pronounced for larger values of the electric field applied perpendicular to the material, is in agreement with the predicted controlled opening of a bandgap. In contrast, these two very specific observations cannot be accounted for simply by an increase in the amount of disorder, for instance caused by the presence of the top-gate. Furthermore, as pointed out earlier, carrier mobilities were comparable in devices with and without top-gates, actually suggesting equal amounts of disorder. Although we cannot rule out that mechanisms other than the formation of a bandgap could lead to the same striking observations, we believe this explanation is the most plausible.

It is clear from the experiments that a possible gap induced in the bilayer device is rather small. This is consistent with recent theoretical calculations [10, 13], which, for zero carrier density and for electric field values of the order of those achieved in our experiments, predict a gap size below approximately 10 meV depending on, for instance, the way in which screening effects in the bilayer are modelled (note that in refs [14, 15], measurements were done at very high charge density, where much larger gap sizes were expected and observed). In comparison, the energy scale of disorder can be estimated to be of the order of a few milli-electron volts from measurements of the

spin splitting in the quantum Hall regime [24], and larger from scanning single-electron transistor experiments [25]. Altogether, it seems that a gap of below 10 meV in conjunction with the presence of subgap states originating from disorder can account for the observed $\exp(T^{-1/3})$ dependence of the resistance in the temperature range between 50 mK and 4.2 K. However, this does not well explain the steep dependence on electric field at 55 K and on temperature above 4.2 K. It is possible that the gap is in fact larger than predicted, or alternatively there may be other mechanisms also contributing to the observed resistance increase in this $n1-n2-n1$ device.

The possibility to use double-gated structures to suppress the conductivity of bilayer graphene to values much lower than $4e^2/h$ represents an important proof-of-principle for the feasibility of future graphene-based electronic devices. Obviously the development of practical devices will require further innovations, which are needed to switch off electrical conduction at room temperature. Nevertheless, the operation of devices at cryogenic temperatures that we have demonstrated here will already enable new fundamental studies of quantum transport in bilayer graphene, through the fabrication of structures such as quantum point contacts based on split gates and electrostatically tunable quantum dots.

References

- [1] K. S. Novoselov, A. K. Geim, S. V. Morozov, D. Jiang, Y. Zhang, S. V. Dubonos, I. V. Grigorieva, and A. A. Firsov, *Electric Field Effect in Atomically Thin Carbon Films*, *Science* **306**, 666 (2004).
- [2] K. S. Novoselov, A. K. Geim, S. V. Morozov, D. Jiang, M. I. Katsnelson, I. V. Grigorieva, S. V. Dubonos, and A. A. Firsov, *Two-dimensional gas of massless Dirac fermions in graphene*, *Nature* **438**, 197 (2005), ISSN 0028-0836.
- [3] Y. Zhang, Y.-W. Tan, H. L. Stormer, and P. Kim, *Experimental observation of the quantum Hall effect and Berry's phase in graphene*, *Nature* **438**, 201 (2005), ISSN 0028-0836.
- [4] K. S. Novoselov, E. McCann, S. V. Morozov, V. I. Fal'ko, M. I. Katsnelson, U. Zeitler, D. Jiang, F. Schedin, and A. K. Geim, *Unconventional quantum Hall effect and Berry's phase of 2π in bilayer graphene*, *Nature Physics* **2**, 177 (2006), ISSN 1745-2473.
- [5] A. K. Geim and K. S. Novoselov, *The rise of graphene*, *Nature Materials* **6**, 183 (2007), ISSN 1476-1122.
- [6] P. R. Wallace, *The Band Theory of Graphite*, *Physical Review Online Archive (Prola)* **71**, 622 (1947).

-
- [7] M. I. Katsnelson, K. S. Novoselov, and A. K. Geim, *Chiral tunnelling and the Klein paradox in graphene*, Nature Physics **2**, 620 (2006), ISSN 1745-2473.
- [8] M. Y. Han, B. Özyilmaz, Y. Zhang, and P. Kim, *Energy Band-Gap Engineering of Graphene Nanoribbons*, Physical Review Letters **98**, 206805 (2007).
- [9] G. Giovannetti, P. A. Khomyakov, G. Brocks, P. J. Kelly, and J. van den Brink, *Substrate-induced band gap in graphene on hexagonal boron nitride: Ab initio density functional calculations*, Physical Review B **76**, 073103 (2007).
- [10] E. McCann, *Asymmetry gap in the electronic band structure of bilayer graphene*, Physical Review B **74**, 161403 (2006).
- [11] G. W. Semenoff, *Condensed-Matter Simulation of a Three-Dimensional Anomaly*, Physical Review Letters **53**, 2449 (1984).
- [12] E. McCann and V. I. Fal'ko, *Landau-Level Degeneracy and Quantum Hall Effect in a Graphite Bilayer*, Physical Review Letters **96**, 086805 (2006).
- [13] H. Min, B. Sahu, S. K. Banerjee, and A. H. MacDonald, *Ab initio theory of gate induced gaps in graphene bilayers*, Physical Review B **75**, 155115 (2007).
- [14] T. Ohta, A. Bostwick, T. Seyller, K. Horn, and E. Rotenberg, *Controlling the Electronic Structure of Bilayer Graphene*, Science **313**, 951 (2006).
- [15] E. V. Castro, K. S. Novoselov, S. V. Morozov, N. M. R. Peres, L. dos Santos, J. Nilsson, F. Guinea, A. K. Geim, and A. H. C. Neto, *Biased Bilayer Graphene: Semiconductor with a Gap Tunable by the Electric Field Effect*, Physical Review Letters **99**, 216802 (2007).
- [16] P. Blake, E. W. Hill, A. H. Castro Neto, K. S. Novoselov, D. Jiang, R. Yang, T. J. Booth, and A. K. Geim, *Making graphene visible*, Appl. Phys. Lett. **91**, 063124 (2007).
- [17] D. S. L. Abergel, A. Russell, and V. I. Fal'ko, *Visibility of graphene flakes on a dielectric substrate*, Appl. Phys. Lett. **91**, 063125 (2007).
- [18] B. Huard, J. A. Sulpizio, N. Stander, K. Todd, B. Yang, and D. G. Gordon, *Transport Measurements Across a Tunable Potential Barrier in Graphene*, Physical Review Letters **98**, 236803 (2007).
- [19] J. R. Williams, L. DiCarlo, and C. M. Marcus, *Quantum Hall Effect in a Gate-Controlled p-n Junction of Graphene*, Science **317**, 638 (2007).
- [20] B. Özyilmaz, P. J. Herrero, D. Efetov, D. A. Abanin, L. S. Levitov, and P. Kim, *Electronic Transport and Quantum Hall Effect in Bipolar Graphene p-n-p Junctions*, Physical Review Letters **99**, 166804 (2007).

- [21] O. Madelung, *Introduction to Solid-State Theory* (Springer, Berlin, Heidelberg, 1978).
- [22] B. I. Shklovskii and A. L. Efros, *Electronic Properties of Doped Semiconductors* (Springer, Berlin, Heidelberg, 1984).
- [23] J. Nilsson and A. H. C. Neto, *Impurities in a Biased Graphene Bilayer*, Physical Review Letters **98**, 126801 (2007).
- [24] Y. Zhang, Z. Jiang, J. P. Small, M. S. Purewal, Y. W. Tan, M. Fazlollahi, J. D. Chudow, J. A. Jaszczak, H. L. Stormer, and P. Kim, *Landau-Level Splitting in Graphene in High Magnetic Fields*, Physical Review Letters **96**, 136806 (2006).
- [25] J. Martin, N. Akerman, G. Ulbricht, T. Lohmann, J. H. Smet, K. von Klitzing, and A. Yacoby, *Observation of electron-hole puddles in graphene using a scanning single-electron transistor*, Nature Physics **4**, 144 (2007), ISSN 1745-2473.

Chapter 5

Coulomb blockade in top-gated graphene nanoribbons

Coulomb blockade is observed in a graphene nanoribbon device with a top gate. When two pn-junctions are formed via the back gate and the local top gate, electrons are confined between the pn-junctions which act as the barriers. When no pn-junctions are induced by the gate voltages, electrons are still confined, as a result of strong disorder, but in a larger area. Measurements on five other devices with different dimensions yield consistent results.

The contents of this chapter are partially published in *Physical Review B*:
X. L. Liu, J. B. Oostinga, A. F. Morpurgo, and L. M. K. Vandersypen, *Electrostatic confinement of electrons in graphene nanoribbons*, *Physical Review B* **80**, 121407R (2009).

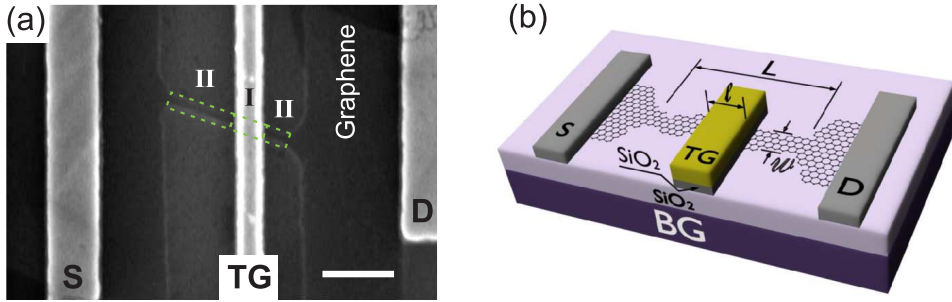


Figure 5.1: (a) Scanning electron microscope image of device *E* (scale bar 300 nm). The light gray dashed lines indicate segment I and II discussed in the text. (b) Schematic drawing of the device.

5.1 Background and introduction

Confinement of the Dirac particles is of particular importance for the realization of nano-electronic devices in graphene such as quantum dots [1]. These would enable one to perform single-level spectroscopy of Dirac particles, study their spin and valley degrees of freedom, and explore their potential for quantum coherent control [2]. In conventional semiconductors, particles can be confined by potential barriers created via electrostatic gates. This approach permits independent control of the number of electrons on the island, the tunnel coupling between the island and the reservoirs, as well as the tunnel coupling between neighbouring islands. Such flexibility and versatility has been instrumental for a wide variety of mesoscopic experiments. In graphene, this approach normally fails, due to the absence of a bandgap and the presence of Klein tunnelling [3, 4]. In previous studies, graphene has been etched into small islands, separated from the reservoir by narrow constrictions [5–7], but here it is difficult to tune the barriers. Alternatively, a bandgap could be created in graphene first, so that electrostatic gates can again be used for confinement. Theoretically, a bandgap is predicted in graphene nanoribbons (GNRs) due mainly to quantum confinement [8–10].

In this chapter I summarize our experimental results on transport through graphene nanoribbons in the framework of Coulomb blockade and quantum dot formation. The devices contain a local top gate (TG) and a global back gate (BG) where the transport gap in the GNR enables electrostatic confinement by the gates. Electrons can be confined in an island where the barriers are formed by the pn -junctions induced at the two edges of the TG, as demonstrated by the capacitances analysis of the measured Coulomb blockade in bipolar regimes. On the other hand, when no pn -junctions were induced by the gates, Coulomb blockade was also observed, showing a larger confinement area. Here the island may be due to Anderson localization. Consistent results were found in six other devices with different dimensions. In addition, disorder present

	Label	<i>A</i>	<i>B</i>	<i>C</i>	<i>D</i>	<i>E</i>	<i>F</i>	<i>G</i>
GNR width	w (nm)	60	50	50	50	40	40	60
GNR length	L (nm)	2000	1500	1000	700	520	520	500
TG width	l (nm)	500	400	200	140	100	50	200

Table 5.1: The dimensions of devices *A* to *F*. The TG dielectric is $d = 10$ nm thick SiO₂ for all devices.

in the system significantly limits the device performance.

5.2 Device fabrication and characterizations

Seven devices (*A* to *G*) are fabricated on graphene flakes deposited on a substrate by mechanical exfoliation of natural graphite [11]. The substrate consists of highly *p*-doped silicon, acting as a back gate (BG), capped by 285 nm of SiO₂. From their optical contrast against the substrate, we estimate that the flakes are single-layer [12]. Three electron beam lithography steps were used for patterning the devices. First, selected graphene flakes are patterned into GNRs, using PMMA as an etching mask and an Ar plasma for etching (for device *F* an O₂ plasma was used). Next we pattern a single top gate across each ribbon. The TG consists of 10/5/40 nm thick evaporated SiO₂/Ti/Au, and it covers only part of the ribbon, denoted as segment I (see Fig. 5.1a). The remainder of the ribbon (segments II) connects to wider pieces of graphene, which are contacted by 10/40 nm thick Ti/Au source (S) and drain (D) electrodes. The device is schematically illustrated in Fig. 5.1b, and the relevant device dimensions are given in Table 5.1.

All measurements were performed in a ³He system at a base temperature of 350 mK, unless stated otherwise. We measured the two terminal resistance through the top gated GNR devices by applying a DC voltage bias, V_{bias} , on the source electrode and measuring the current at the drain electrode.

By tuning the BG and TG voltages, we can shape the potential landscape along the ribbon. Fig. 5.2a shows the low bias conductance of device *G* as a function of V_{BG} and V_{TG} . Along the dark vertical band, the conductance is suppressed as E_F is within the transport gap in segment II. Along the dark diagonal band, the TG and BG dope the graphene with opposite polarity and E_F lies in the transport gap in segment I. At zero gate voltages, the device is slightly hole doped.

When $0 \lesssim V_{BG} \lesssim 10$ V and $V_{TG} \approx 0$, E_F lies in the transport gap in both segment I and II. This is also indicated by the suppressed conductance in Fig. 5.2b. Furthermore, Fig. 5.2b shows that when the bias voltage is higher than ≈ 20 mV, conductance through the ribbon increases again, similar to the case of Coulomb blockade (see also section 2.4). The 20 meV thus gives an estimate of the energy needed for the electrons to overcome the transport gap. This energy scale is also sometimes referred to the energy

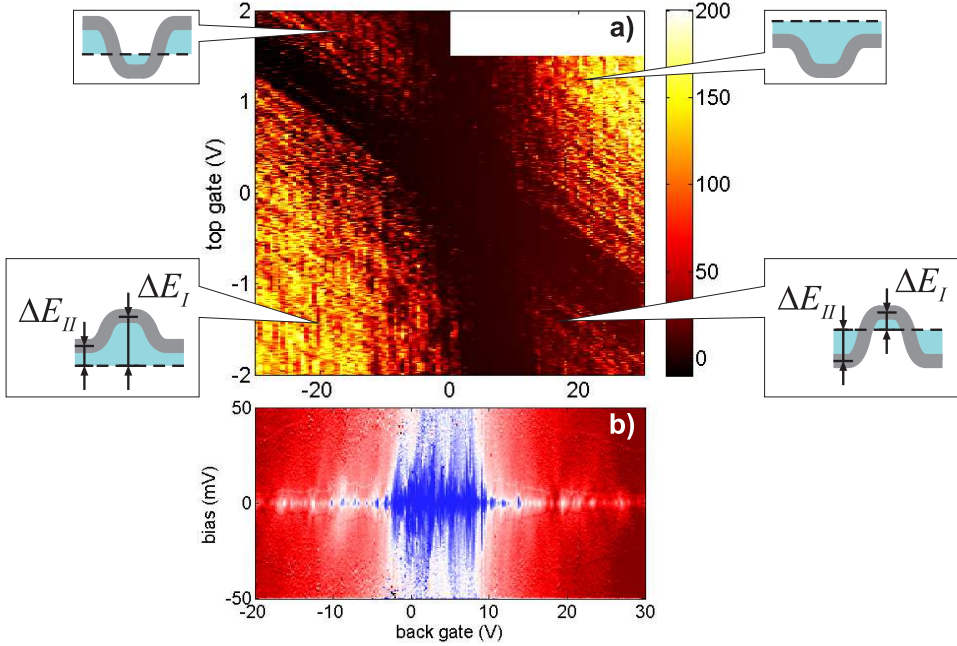


Figure 5.2: (a) Current as a function of the back gate and top gate voltages for device G at $V_{bias} = 30 \mu\text{V}$ and $T = 350 \text{ mK}$. The insets illustrate the potential landscapes that are created in the four corners of the plot. They represent energy diagrams along the ribbon length, where the gray band indicates the transport gap and the dashed lines represent the Fermi level E_F . $\Delta E_{I(II)}$ reflects the doping level in segment I (II). (b) Differential conductance dI/dV as a function of (b) V_{BG} and V_{bias} at $V_{TG} = 0$. $T = 350 \text{ mK}$.

gap or addition energy in the literature [13–21].

In the lower right (upper left) corner of Fig. 5.2, the ribbon is in a npn (pnp) configuration. In this regime, holes (electrons) can be confined in the area (segment I) between the two pn -junctions owing to the presence of the transport gap [22, 23]. We thus expect Coulomb blockade in the npn and pnp regimes. In the lower left (upper right) corner, the ribbon is in a $pp'p$ ($nn'n$) configuration. Here Fabry-Perot type resonances could occur between the two steps in the potential landscape, but no Coulomb blockade is expected in an ideal ribbon, as there are no barriers. The difference in energy from E_F to the middle of the transport gap in segment I and II are denoted as ΔE_I and ΔE_{II} , respectively, which is a measure of the doping level.

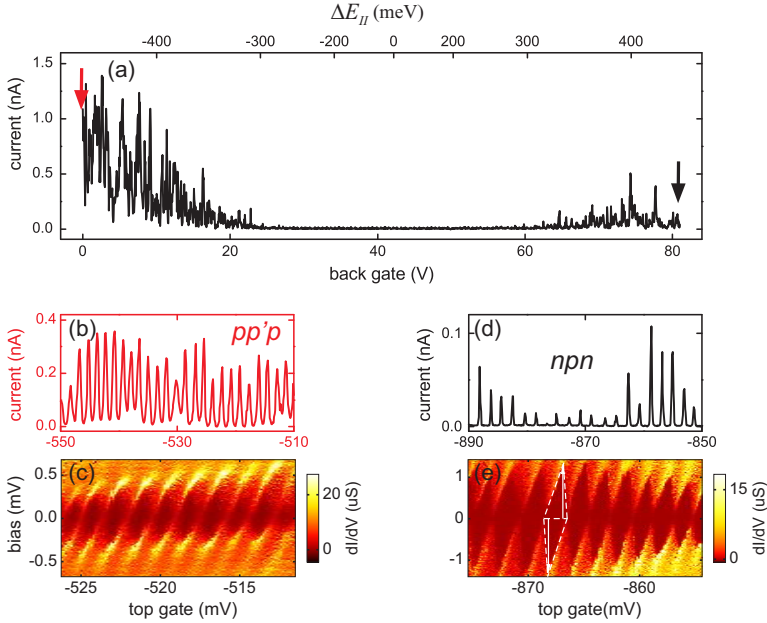


Figure 5.3: (a) Current as a function of V_{BG} for device *B* at $V_{TG} = -1.2$ V and $V_{bias} = 200$ μ V. The top axis indicates the corresponding doping level in segment II, ΔE_{II} , estimated in the same way as ΔE_I (see text). (b) Coulomb oscillations as a function of V_{TG} in the $pp'p$ configuration. $V_{BG} = 0$ as indicated by the gray arrow in (a) and $V_{bias} = 100$ μ V. (c) Differential conductance dI/dV as a function of V_{TG} and V_{bias} (Coulomb diamonds), measured in the same $pp'p$ regime as (b). (d) Coulomb oscillations as a function of V_{TG} in the npn configuration. $V_{BG} = +81$ V as indicated by the black arrow in (a), and $V_{bias} = 100$ μ V. (e) Coulomb diamonds measured in the same npn regime as (d). The addition energy E_a is taken as the average of the two white arrows.

5.3 Coulomb blockade in the npn regime

In the npn configuration, we observe pronounced current peaks separated by zero-current regions as V_{TG} is swept. A representative measurement is shown in Fig. 5.3d for device *B*, measured in the gate voltage configuration indicated by the black arrows in Fig. 5.3a and 5.5b. High bias measurements in the same range (Fig. 5.3e) show diamond-shaped regions in the $V_{bias} - V_{TG}$ plane, in which current is blocked. Both are characteristic of Coulomb blockade due to the formation of an island that is only weakly coupled to the leads.

Fig. 5.4a shows the evolution of a few Coulomb peaks in the npn configuration as a function of a perpendicular applied magnetic field. When the perpendicular field is increased, the positions of all Coulomb peaks shift towards negative top gate voltages, i.e. away from the transport gap. This is qualitatively understandable within the

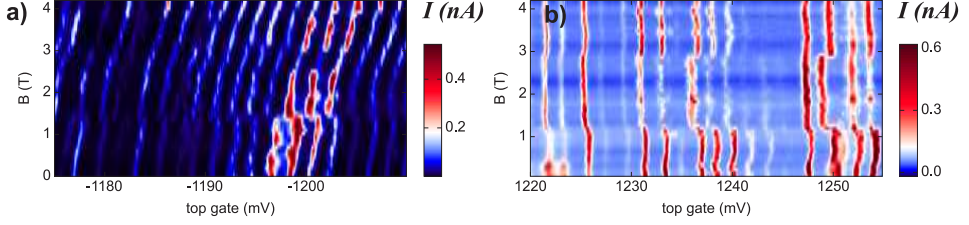


Figure 5.4: Current as a function of V_{TG} and perpendicular magnetic field B in (a) the nnp configuration, $V_{BG} = +81$ V and $V_{bias} = 200$ μ V; and (b) the $pp'p$ configuration where $V_{BG} = 0$ and $V_{bias} = 100$ μ V.

framework of the Landau level [24], and confirms that the dot is filled with holes. Quantitatively speaking, however, (1) we expect the cross-over to the Landau level regime to occur at a much larger magnetic field rather than in the range $0 < B < 4$ T, since the cyclotron diameter $2R_C$ is around the size of the ribbon width (50 nm) at $B \approx 8$ T; (2) the magnitude of the change in the Coulomb peak position as a function of magnetic field is much smaller than what is expected from Landau levels, assuming an island area of wl . At the moment we don't understand this particular magnetic field dependence.

In this device, over 700 Coulomb peaks were resolved in the range -2 V $< V_{TG} < -0.2$ V, corresponding to a large change in doping level in segment I, -360 meV $\lesssim \Delta E_I \lesssim -240$ meV (Fig. 5.5a). Here ΔE_I reflects the doping level in segment I (Fig. 5.2 inset), and is roughly estimated by considering the density of states of bulk graphene, $\Delta E_I = (\pm)\hbar v_F \sqrt{\pi n_I}$, where n_I is the carrier density in region I, v_F is the Fermi velocity of bulk graphene, and the (+) and (-) signs represent electron and hole doping, respectively. The spacings between neighbouring peaks, ΔV_{TG}^{nnp} , are shown in Fig. 5.5a (black spheres), as a function of the peak positions. The average value $\langle \Delta V_{TG}^{nnp} \rangle = 2.0 \pm 0.4$ mV corresponds to a TG capacitance $C_{TG} = 70-100$ aF, close to what one would expect from simple parallel plate capacitance between the TG and segment I, $C_{TG}^{\parallel} = \epsilon_0 \epsilon_r wl/d = 70$ aF, where $\epsilon_r = 3.9$ is the relative permittivity of SiO₂. In addition, the capacitance to the back gate, measured to be ~ 3.9 aF, compares well to the value expected from the geometry of an island of area (wl). The agreement demonstrates that for this device, an island is formed between the two pn -junctions in the nnp configuration.

In addition, we measured over 100 Coulomb diamonds similar to Fig. 5.3e, and the extracted addition energy E_a^{nnp} for each diamond is shown in Fig. 5.5a with green triangles. The average addition energy is $\langle E_a^{nnp} \rangle = 1.0 \pm 0.4$ meV. From Fig. 5.5a, no spin filling or shell filling or evident particle number dependence is observed in either ΔV_{TG} or E_a , but both quantities show a large spread similar to [5, 6], due to contributions from both the level spacing and strong disorder from the ribbon edges, which is discussed further in section 5.8.2. In all these measurements, segments II of the GNR were heavily n -doped such that disorder in the leads was largely screened ($V_{BG} = +81$ V). This is in contrast to the case that when the carrier density in segment I or II is low, low bias

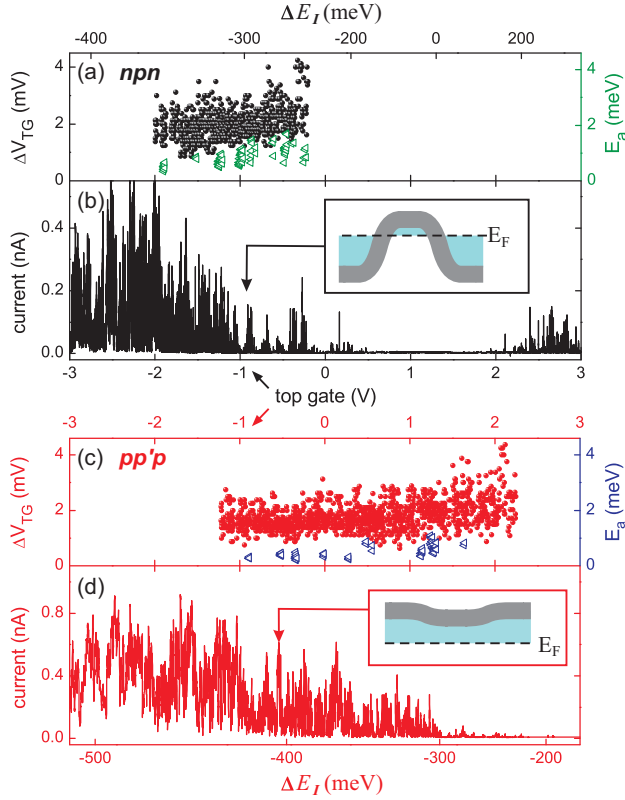


Figure 5.5: (a) ΔV_{TG} (black spheres) and E_a (gray triangles) as a function of peak positions in the *npn* regime for device *B*. $V_{BG} = +81$ V. (b) Current (black line) as a function of V_{TG} at $V_{bias} = 100$ μ V and $V_{BG} = +81$ V. (c) ΔV_{TG} (gray spheres) and E_a (gray triangles) in the *pp'p* regime for at $V_{BG} = 0$. (d) Current (gray line) as a function of V_{TG} at $V_{bias} = 100$ μ V and $V_{BG} = 0$. The corresponding doping level in segment I, ΔE_I , are indicated in the top axis (a) and bottom axis (d). The two insets illustrate the potential landscapes created at the gate voltage configurations where Fig. 5.3b and 5.3d are taken.

conductance vanishes and Coulomb diamonds overlap which is discussed later in this chapter (see section 5.6).

Coulomb blockade in the *npn* configuration was found in three other devices of different dimensions (*A*, *C*, *E*) where the *npn* regime could be accessed (the various devices exhibited different positions of the charge neutrality point). For device *E*, also the *pnp* configuration could be reached, where the measurement results are analogous to those for *npn*. The extracted $\langle \Delta V_{TG}^{nnp} \rangle$ and $\langle E_a^{nnp} \rangle$ for these devices are summarized in Fig. 5.6a (black filled circles) and 5.6b (black filled squares), respectively. For all four devices, the measured $\langle \Delta V_{TG}^{nnp} \rangle$ agrees quantitatively well with the numerically computed

e/C_{TG} [25] by considering an island of size wl (black dotted line in Fig. 5.6a). Moreover, both $\langle \Delta V_{TG}^{npp} \rangle$ and $\langle E_a^{npp} \rangle$ increase with decreasing area (wl), consistent with the observation in device *B*, i.e. carriers are confined in segment I in the *npp* configuration.

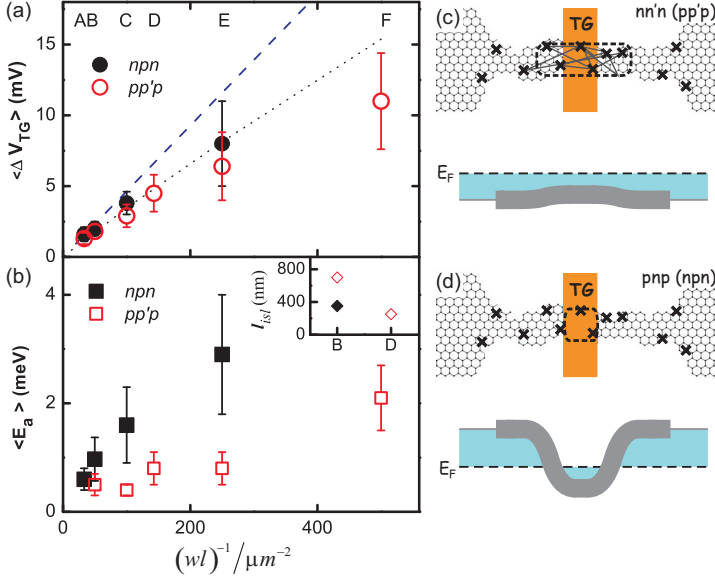


Figure 5.6: (a) Average peak spacing versus the inverse area of segment I, $(wl)^{-1}$, in the *npp* (black filled circles) and *pp'p* (gray open circles) configurations, for devices *A* through *F* as indicated. The dashed line is the peak spacing estimated by e/C_{TG}^{\parallel} , where C_{TG}^{\parallel} is a parallel plate capacitance between the TG and GNR (see text). The values of e/C_{TG} were also computed numerically by considering an island of area (wl) (black dotted line) [25]. (b) Average addition energy extracted from Coulomb diamonds measured in the *npp* (black filled squares) and *pp'p* (gray open squares) configurations versus $(wl)^{-1}$. The error bars in (a,b) represent standard deviation. Inset: the island size in the direction along the ribbon length (l_{isl}) for devices *B* and *D* in both *npp* (black filled diamonds) and *pp'p* (gray open diamonds) regimes extracted from the back gate capacitances. (c,d) Schematic illustrations of the device, with the \times symbol representing the scattering sites and the island enclosed in dashed lines. The underlying energy diagrams for the *nn'n* (c) and *pnp* (d) regimes are also shown where the gray band represents the transport gap in the GNRs.

From the measured Coulomb diamonds, we estimate the capacitance of the dot to the source contact, the top gate, and the total capacitance based on a purely capacitively coupled quantum dot model (see chapter 2). The result is plotted in Fig. 5.7a, where the total capacitances C_{tot} (squares) are extracted from the average addition energy E_a (assuming the level spacing is zero), the top gate capacitances C_{TG} (circles) are extracted from the average peak spacing ΔV_{TG} , and the source contact capacitances C_s (triangles) are extracted from the slope of the Coulomb diamonds. The back gate capacitance C_{BG} (diamond) of device *B* estimated from its level arm with respect to that of C_{TG} (as directly obtainable from the stability diagrams as a function of V_{BG} and

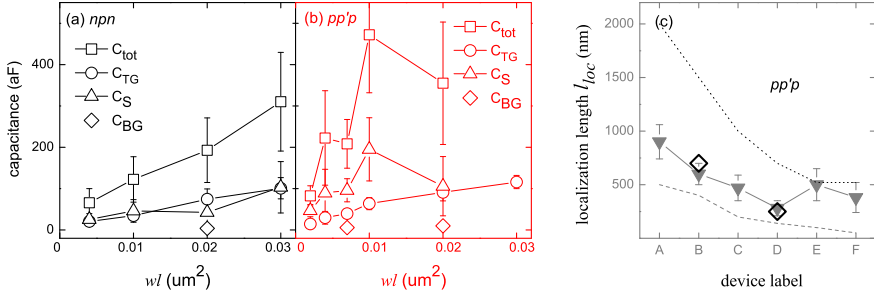


Figure 5.7: Extracted average capacitances versus the area of segment I, (wl), in both the npn (a) and $pp'p$ (b) configurations. The error bars represent standard deviations. (c) The average localization length l_{loc} (filled triangles) estimated from the peak conductance measured in the $pp'p$ regimes for devices A to F. The error bars represent standard deviations. The island sizes (open diamonds) extracted from the measured back gate capacitances are also shown for devices B and D. The dashed and dotted line indicates the TG width l and ribbon length L of each device, respectively.

V_{TG}) is also included in the plot. All capacitances increase as the device dimensions wl increase, as expected. From Fig. 5.7 we see that, for all four devices, the top gate capacitance C_{TG} makes up only around 1/3 of the total capacitance, and is of the same magnitude as the capacitance to the source contact C_S in this npn configuration. This is at the first sight surprising, assuming a device geometry that the leads are spatially separated from the dot. A plausible explanation to this large source / drain capacitance is that the wavefunctions of the electrons on the dot and on the leads overlap in space [26]. Nevertheless, the fact that the top gate capacitance is not the dominant capacitance of the system undermines the reliability of the estimate of dot area based on C_{TG} .

5.4 Coulomb blockade in the $pp'p$ regime

Unexpectedly, Coulomb blockade was also observed when no pn -junctions are present. Fig. 5.3b and 5.3c show a representative current trace and Coulomb diamonds measured from the same device in a $pp'p$ configuration indicated by the red arrows in Fig. 5.3a and 5.5d. As a function of perpendicular magnetic field up to 4 T, the positions of these Coulomb peaks barely change as shown in Fig. 5.4b, in contrast to the case of npn (Fig. 5.4a). The weak magnetic field dependence could be because the applied field is rather low. No higher magnetic field data are available at the moment.

Over 1400 current peaks were observed in the range $-1 \text{ V} < V_{TG} < 2.2 \text{ V}$, corresponding to a change in doping level ΔE_I from -430 meV to -230 meV (Fig. 5.5c). We measured 70 Coulomb diamonds in the same range. The extracted peak spacings $\Delta V_{TG}^{pp'p}$

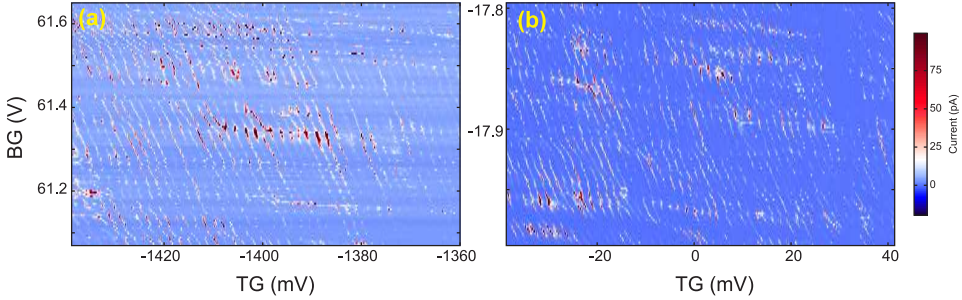


Figure 5.8: Current as a function of the back gate and top gate voltages for device *B* measured in the *npn* (a) and *pp'p* (b) configurations. $V_{bias} = 200 \mu\text{V}$ (a) and $20 \mu\text{V}$ (b). $T = 30 \text{ mK}$.

and addition energy $E_a^{pp'p}$ are shown in Fig. 5.5c with red spheres and blue triangles, respectively. The measurements were taken at $V_{BG} = 0$ (red arrow in Fig. 5.3a), such that segment II of the GNR was heavily *p*-doped.

The average peak spacing in the *pp'p* configuration $\langle \Delta V_{TG}^{pp'p} \rangle = 1.8 \pm 0.4 \text{ mV}$ is very close to $\langle \Delta V_{TG}^{nnpn} \rangle$, but the average addition energy $\langle E_a^{pp'p} \rangle = 0.5 \pm 0.2 \text{ meV}$ is only half the value of $\langle E_a^{nnpn} \rangle$. The back gate capacitance in *pp'p* is $\sim 10 \text{ aF}$, indicating an island area of 50 nm by 700 nm , larger than (wl) (assuming the island extends over the entire ribbon width in the transverse direction). All average quantities were reproducible over multiple thermal cycles. Therefore the island formed in the *pp'p* configuration is located in part under the TG, but extends to a larger area than the island in the *nnpn* case.

Furthermore, we observed Coulomb blockade in the *pp'p* regime in all six devices *A* to *F*. For devices *A, B, E*, we could also access the *nn'n* configuration and the results are similar to those in the *pp'p* case. For all devices, the average addition energy, $\langle E_a^{pp'p} \rangle$ in the *pp'p* regime is much smaller than that in the *nnpn* case, and does not vary much despite the differences in device dimensions (except for device *F*), as shown by the gray open squares in Fig. 5.6b (no clear Coulomb diamonds were observed in device *A* in the *pp'p* regime). In devices *B* and *D*, the measured back gate capacitance indicates that the island sizes are $50 \times 700 \text{ nm}^2$ and $50 \times 250 \text{ nm}^2$, respectively (Fig. 5.6b inset), significantly larger than the area of segment I. The capacitance of this large island to the relative narrow TG, $C_{TG}^{pp'p}$, is still roughly the same as that for an island limited to segment I, so the peak spacings in *pp'p* (Fig. 5.6a, gray circles) are similar to those for *nnpn*.

Similar to the case of *nnpn*, the extracted capacitance values based on the measured Coulomb diamonds in the *pp'p* configurations are plotted in Fig. 5.7b for all six devices. The source / drain capacitances in this regime are very large for all devices and dominate the scaling of addition energy as a function of device dimensions as presented in

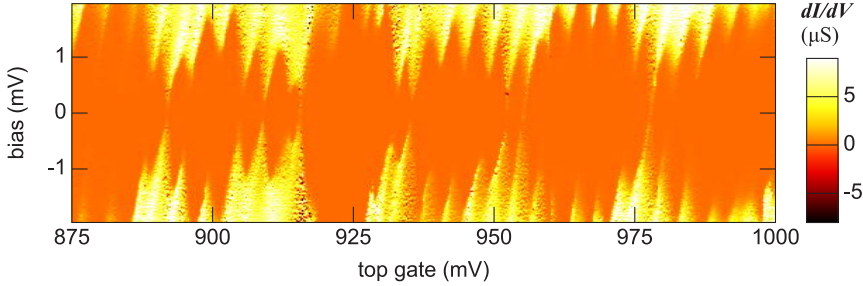


Figure 5.9: Differential conductance as a function of bias and top gate voltage for device D measured with V_{BG} fixed at zero. $T = 350$ mK.

Fig. 5.6. Similar to the case of npn , also in this regime we couldn't extract the island size with high precision due to the large source / drain capacitance. Notice in contrast to the npn case where $C_S \approx C_{TG}$, here in the $pp'p$ case $C_S > C_{TG}$.

The reproducible scaling of addition energy and peak spacing as a function of devices dimensions is consistent with the results obtained from device B : when pn -junctions are induced by the TG and BG, an island is formed in between the junctions; without the pn -junctions, a much larger island is formed, presumably due to disorder. However, the source and drain capacitances are comparable (npn) or even larger ($pp'p$) than C_{TG} , and contribute more than half of the total capacitance. This means that extracting the island size from E_a may be unreliable. For device B (npn and $pp'p$) and D ($pp'p$), we have measured the back gate capacitance, which gives an independent estimate of the island size (Fig. 5.6b inset) and is in agreement with our interpretation of the island size in the two regimes.

These disorder-induced islands in the $pp'p$ regimes are 5-10 times longer than the ribbon width, which could be explained by Anderson localization, due to strong scattering at the rough ribbon edges as proposed in [27–32].

In an Anderson insulator, the conductance through the channel decreases exponentially as the length of the sample grows. For a simple estimate of the localization length l_{loc} in the GNRs, we use the relation $G = N_{1D}(e^2/h)\exp(-2L/l_{loc})$ [27], where N_{1D} is the number of 1D channels and L is the length of the ribbons. Since the original theory does not take into account Coulomb blockade, we take G as the conductance measured at the Coulomb peak maxima, where the gate compensates the charging energy exactly and the interaction effect is small. This very rough estimate gives a value for l_{loc} (Fig. 5.7c, filled triangles) that is much longer than the ribbon width w (40 nm to 60 nm). For two devices B and D , the island size in the $pp'p$ regime is extracted from the measured back gate capacitance as mentioned above. The island size (along the ribbon length direction) is also shown in Fig. 5.7c (open diamonds), and is on the same order of magnitude as the estimated l_{loc} .

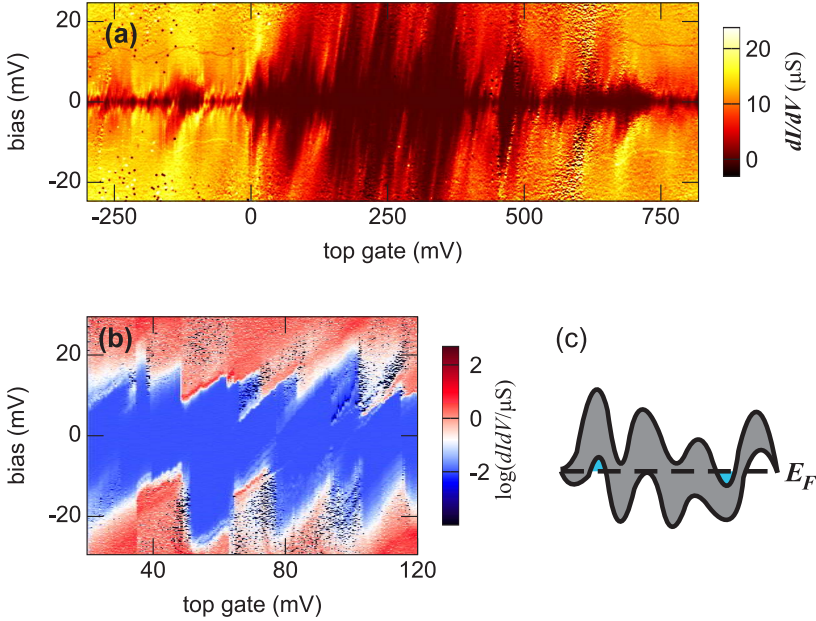


Figure 5.10: Differential conductance dI/dV as a function of V_{TG} and V_{bias} at (a) $V_{BG} = -5.5$ V and (b) $V_{BG} = 0$ for device G . In panel (b), the color scale represents the log scale of the differential conductance. $T = 350$ mK. (c) Schematic illustration of one possible scenario for the energy diagram in the transport gap and the formation of multi-grains. The dashed line represents the Fermi energy.

This result reveals a different aspect of the electronic properties of the GNRs compared to other work, where the extent of the island is found to be comparable with the ribbon width [16, 18, 33]. Further studies are needed in order to clarify the underlying mechanisms behind the various observations.

5.5 Multiple dots behaviour

If islands are induced by disorder in the pp' case, there are likely to be disorder-induced islands in the nnp case as well in addition to the islands formed by the pn -junctions. Indeed evidence of multiple islands was observed experimentally in several gate voltage regimes.

Fig. 5.8a shows an example measurement taken on device B in the nnp regime, where the current peaks do not run exactly parallel to each other as V_{TG} and V_{BG} are swept. This indicates that multiple islands are present in the system. Most prominently, in the top right corner of the plot, these current lines are broken up into isolated triple

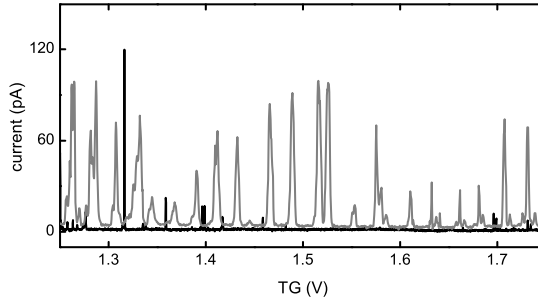


Figure 5.11: Current as a function of TG voltage for device D measured at bias $V_{bias} = 100 \mu\text{V}$, $T = 350 \text{ mK}$ (black curve) and $T = 2 \text{ K}$ (gray curve). The BG is fixed at zero voltage, such that the segment II of the ribbon is p -doping, while the segment I of the ribbon is within the transport gap.

points, implying that electron transport here occurs only when the electrochemical potential in one dot is lined up with the electrochemical potential level in another dot. This is indicative of transport through two dots in series. In the top left corner of the plot, honeycomb like features are also visible. This can occur when there is coupling between the dots. Similar features are found in the $pp'p$ configurations (Fig. 5.8b).

Sometimes Coulomb diamonds type of measurements also give indications on the presence of additional dots in series or in parallel [34, 35]. Fig. 5.9 gives an example of Coulomb diamonds measured in a regime where there are two dots in series. One prominent feature from the plot is that the addition energy oscillates as the number of particles change, and the oscillation period is approximately five electrons. This is an indication of the presence of two dots, and one dot is coupled approximately five times stronger to the top gate than the other. The large capacitive coupling can be due to either a larger dot size or a closer position to the top gate. In addition, the Coulomb diamonds overlap (especially when the addition energy is large). The overlapping diamonds suggest that the two dots are in series. We note that sometimes regular Coulomb diamonds can appear in a double dot system in the presence of co-tunneling. Thus the diamonds analysis is a less sensitive tool for identifying the number of islands.

From these stability diagrams, it's apparent that the presence of the additional dots contributes to the large spread in peak spacings and addition energies mentioned earlier (Fig. 5.5).

5.6 Coulomb blockade within the transport gap

In this section we switch to discuss the regime inside the transport gap, i.e. when the density is low. As already mentioned earlier, in this regime, strong disorder can break

a GNR into a series of small islands where the carriers are localized. In such a multi-grain system, we typically observe that low bias conductance vanishes and Coulomb diamonds overlap, similar to what was reported in the literature [16, 18, 33]. Below I will support this statement with some measurements.

Fig. 5.10a plots differential conductance as a function of the top gate and bias voltages for device *G* when the back gate was fixed at -5.5 V (as indicated by the vertical dashed line in Fig. 5.2a). The transport in segment I is clearly visible within the range $0 \lesssim V_{TG} \lesssim 0.5$ V. Similar to the measurement of Fig. 5.2b, the conductance through the ribbon increases again when a bias voltage higher than ≈ 15 mV is applied.

In addition, we now can clearly see that finer structures are present within the transport gap, in contrast to uniform zero conductance as one would naively expect. In fact, the finer structures resemble overlapping diamonds that are often observed in multi-grain quantum dot systems (Fig. 5.10b). We extract an addition energy of around 18 meV in this regime, which is almost one order of magnitude higher than that measured in the high density regimes (Fig. 5.6). Following ref. [16], Fig. 5.10c shows an illustration of the disorder potential and the formation of the multiple dots in the ribbon. We note that here we could not distinguish whether the source of the disorder is the rough edge of the ribbon or charged impurities and is thus unspecified.

We notice that the "energy gaps" extracted from Fig. 5.2b ($\Delta V_{bias}^{(1)} \approx 20$ meV) and Fig. 5.10a ($\Delta V_{bias}^{(2)} \approx 15$ meV) are slightly different. This difference could be due to the difference in effective length of the segment where transport is suppressed: in the former case, the entire ribbon (length $L = 500$ nm) is pinched-off, while in the later case, only segment I (length $l = 200$ nm) is pinched-off. This length dependence of energy gap could be due to at least two possible reasons: (1) Following ref. [20], the transport through the ribbon is diffusive and responds directly to the driving electric field. For the same "critical" electric field needed for the transport to be enabled, a longer ribbon needs a higher bias voltage than a shorter one. This is reasonable as $\Delta V_{bias}^{(1)}/L \approx \Delta V_{bias}^{(2)}/l$; (2) Within the framework of coulomb blockade in multi-grain systems, without co-tunneling, transport can occur only if the energy levels of all grains are aligned. The chance for this to occur decreases as the number of grains increases. For a longer ribbon, the number of grains is larger, thus a larger energy window is needed for transport to occur. A quantitative analysis based on this picture is however difficult.

Furthermore, we observed an interesting temperature dependence of the Coulomb oscillations in this regime, as shown in Fig. 5.11. The black curve is the low bias conductance through device *D* within the transport gap in segment I measured at 350 mK. Several current peaks are visible but the spacings between them are random. When the temperature is increased to 2 K (gray curve), a more regular Coulomb oscillation is restored. Such behavior is indeed predicted for a double dot system [36].

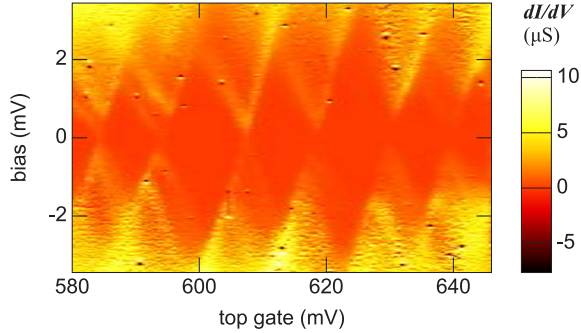


Figure 5.12: Differential conductance dI/dV as a function of V_{TG} and V_{bias} (Coulomb diamonds) for device F , measured in the $pp'p$ regime. $V_{BG} = 0$, $T = 350$ mK.

5.7 Conclusions

In conclusion, a single electron transistor is formed in graphene nanoribbon devices with single top gates. Two pn -junctions at the two edges of the top gate induced by the top gate and back gate voltages act as barriers to form an island. Hundreds of Coulomb peaks were observed in this regime. In the absence of the pn -junctions, regular Coulomb blockade is also observed where the island can be induced by ribbon edge disorder. Observations from measurements of five other devices give consistent results. When the number of electrons is very small, however, the system break into multiple islands due to disorder. We anticipate that multiple top gates on a graphene nanoribbon will offer additional control for future device applications, and provide further insight into the electronic properties of graphene nanoribbons.

5.8 Additional information

5.8.1 Estimate level spacing

For device F , we could resolve the excited states from Coulomb diamonds measurements as shown in Fig. 5.12. We see that the level spacing in the regime with $V_{TG} \approx 0.6$ V is around $\delta E \approx 0.2 - 0.6$ meV.

The level spacing can also be estimated using the method described in the appendix B of this thesis. For this device, the measurement shown in Fig. 5.12 is taken in the regime where $E_F \approx 80$ meV. The GNR of device F is 40 nm in width, giving an expected bandgap $E_g \approx 25$ meV. The number of occupied 1D subbands is then $N_{1D} \approx E_F/(E_g/2) \approx 6$. The expected level spacing for a single 1D subband is $\delta E_{1D} \approx 4$ meV assuming the island extends to the entire 520 nm long ribbon. And we finally ob-

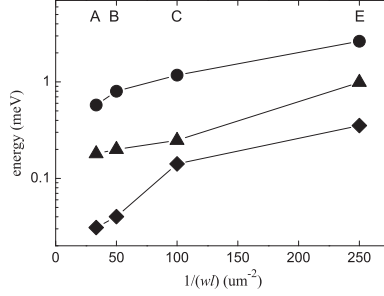


Figure 5.13: Estimated average level spacing (diamonds) as a function of $1/(wl)$ for devices A, B, C and E in the npn regimes. The measured average peak spacings (circles) and the standard deviations (triangles) are also shown (same data as the filled circles and error bars in Fig. 5.6a, but converted to energy via the α factor).

tain an expected average level spacing $\delta E^{(F)} \approx 0.2$ meV, smaller but on the same order of magnitude as the measured result. This agreement suggests that the method that we used for estimating level spacing gives reasonable estimates.

Label	A	B	C	E
α/e	0.36	0.4	0.3	0.33
N	31	30	17	13

Table 5.2: The average α factor and a typical number of occupied 1D sub-bands N for devices A, B, C and E in the npn regimes.

Using the same method, we obtain an average level spacing for device B to be $\delta E^{(B)} \approx 0.04$ meV¹. We can now compare the estimated level spacing with the measured Coulomb peak spacings and addition energies and its spread. From Fig. 5.5, the average peak spacing is ~ 0.8 meV (using an α factor of $0.4e$) and the average addition energy is ~ 1 meV, both are at least 20 times larger than the estimated level spacing in the dot. Therefore we expect the level spacing not to give a dominant contribution to the average peak spacing. On the other hand, the spread of the peak spacing, measured by the standard deviation, is 0.2 meV, and the spread of the addition energy is 0.4 meV, both are relatively comparable to the estimated level spacing. Therefore the level spacing may also contribute to the observed large spread in peak spacing discussed in the main text.

Similar results were found in other devices. In Fig. 5.13, we plot the results of the estimated typical level spacing (an average value for E_F was used from the energy range where measurements were taken) for devices A, B, C and E in the npn regimes (diamonds). For all four devices, the estimated average level spacing is one order of magnitude smaller than the average peak spacing (circles), and is also a few times smaller

¹Parameters used: $E_g \approx 20$ meV, $\delta E_{1D} \approx 5$ meV, $E_F \approx 300$ meV, and the number of occupied 1D subbands is $N_{1D} \approx 30$.

than the standard deviation from the peak spacing (triangles). Thus, for all our devices, we expect that the charging energy dominates the measured peak spacing, and the level spacing gives a small contribution to the observed large spread. Table 5.2 lists the average values of N and α factor used for the plot.

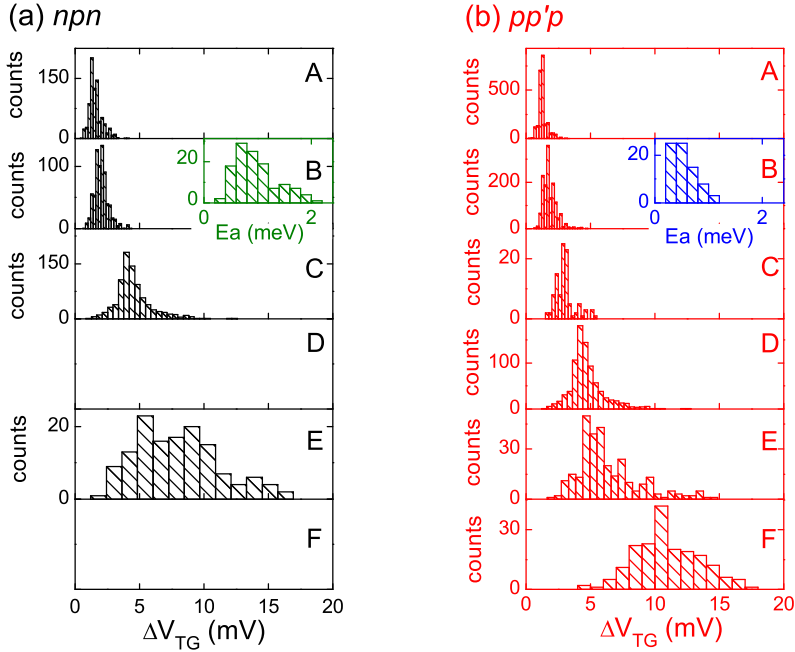


Figure 5.14: The histograms of the peak spacings ΔV_{TG} for all devices in the *npn* (a) and *pp'p* (b) configurations. The device labels *A* to *F* are indicated in the graph. For device *B*, the histograms of the addition energy E_a are shown as well, both in the *npn* (light gray columns) and the *pp'p* (dark gray columns) configurations.

5.8.2 Statistics of peak spacings

In both the bipolar and unipolar regimes, we found a large spread in the measured peak spacing for all devices. Fig. 5.14 gives the histograms of the measured peak spacings from top gate sweeps for devices *A* to *F*. Clearly, as the device area increases (from down to up), the center position of the histograms shifts to higher values, as expected for a growing island size. For device *B*, the histograms for the addition energy are given

as well, both in the bipolar and in the unipolar regime (from the same data as shown in Fig. 5.5a and 5.5c).

5.8.3 Coulomb staircase

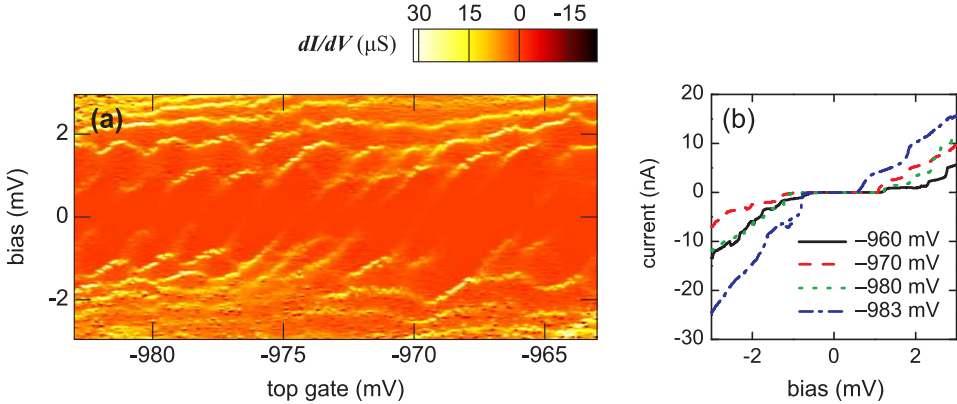


Figure 5.15: (a) Differential conductance dI/dV as a function of V_{TG} and V_{bias} (Coulomb diamonds) for device B measured in an npn regime. $V_{BG} = 81$ V and $T = 350$ mK. (b) Current as a function of bias in the same regime as (a) at several TG voltages as indicated in the graph.

We observed Coulomb staircase in one particular voltage configuration in the npn regime for device B , as shown in Fig. 5.15b, where pronounced current steps appear in the IV characteristics. Fig. 5.15a plot the steps as a function of the back gate voltage.

This observation allows us to infer some interesting properties of the barriers of the dot. Coulomb staircase can occur when the incoming barrier is much more transparent than the outgoing one [37, 38]. Such a situation is unlikely if the barriers are formed by clean $p-n$ junctions in the conventional semiconductor language. A possible scenario that can account for this is that, across a $p-n$ junction in a disordered GNR, the carrier density change from one polarity to the other and at exactly the $p-n$ junction location, carrier density is close to zero and the impedance is high which is sufficient for defining an island [39]. In other words, disorder may strongly affect the barrier transparencies, and lead to asymmetric barriers.

References

- [1] L. P. Kouwenhoven, C. M. Marcus, P. L. McEuen, S. Tarucha, R. M. Westervelt, and N. S. Wingreen, *Electron transport in quantum dots* (Kluwer, Alphen aan den Rijn, the Netherlands, 1997).

-
- [2] B. Trauzettel, D. V. Bulaev, D. Loss, and G. Burkard, *Spin qubits in graphene quantum dots*, Nature Physics **3**, 192 (2007), ISSN 1745-2473.
- [3] M. I. Katsnelson, K. S. Novoselov, and A. K. Geim, *Chiral tunnelling and the Klein paradox in graphene*, Nature Physics **2**, 620 (2006), ISSN 1745-2473.
- [4] A. K. Geim and K. S. Novoselov, *The rise of graphene*, Nature Materials **6**, 183 (2007), ISSN 1476-1122.
- [5] L. A. Ponomarenko, F. Schedin, M. I. Katsnelson, R. Yang, E. W. Hill, K. S. Novoselov, and A. K. Geim, *Chaotic Dirac Billiard in Graphene Quantum Dots*, Science **320**, 356 (2008).
- [6] C. Stampfer, J. Güttinger, F. Molitor, D. Graf, T. Ihn, and K. Ensslin, *Tunable Coulomb blockade in nanostructured graphene*, Appl. Phys. Lett. **92**, 012102 (2008).
- [7] J. Güttinger, C. Stampfer, S. Hellmüller, F. Molitor, T. Ihn, and K. Ensslin, *Charge detection in graphene quantum dots*, Applied Physics Letters **93**, 212102 (2008).
- [8] K. Nakada, M. Fujita, G. Dresselhaus, and M. S. Dresselhaus, *Edge state in graphene ribbons: Nanometer size effect and edge shape dependence*, Physical Review B **54**, 17954 (1996).
- [9] L. Brey and H. A. Fertig, *Electronic states of graphene nanoribbons studied with the Dirac equation*, Physical Review B **73**, 235411 (2006).
- [10] Y. W. Son, M. L. Cohen, and S. G. Louie, *Energy Gaps in Graphene Nanoribbons*, Physical Review Letters **97**, 216803 (2006).
- [11] K. S. Novoselov, A. K. Geim, S. V. Morozov, D. Jiang, M. I. Katsnelson, I. V. Grigorieva, S. V. Dubonos, and A. A. Firsov, *Two-dimensional gas of massless Dirac fermions in graphene*, Nature **438**, 197 (2005), ISSN 0028-0836.
- [12] J. B. Oostinga, H. B. Heersche, X. Liu, A. F. Morpurgo, and L. M. K. Vandersypen, *Gate-induced insulating state in bilayer graphene devices*, Nature Materials **7**, 151 (2007), ISSN 1476-1122.
- [13] M. Y. Han, B. Özyilmaz, Y. Zhang, and P. Kim, *Energy Band-Gap Engineering of Graphene Nanoribbons*, Physical Review Letters **98**, 206805 (2007).
- [14] X. Li, X. Wang, L. Zhang, S. Lee, and H. Dai, *Chemically Derived, Ultrasmooth Graphene Nanoribbon Semiconductors*, Science **319**, 1229 (2008).
- [15] F. Molitor, A. Jacobsen, C. Stampfer, J. Güttinger, T. Ihn, and K. Ensslin, *Transport gap in side-gated graphene constrictions*, Physical Review B **79**, 075426 (2009), ISSN 1098-0121.

- [16] C. Stampfer, J. Güttinger, S. Hellmüller, F. Molitor, K. Ensslin, and T. Ihn, *Energy Gaps in Etched Graphene Nanoribbons*, Physical Review Letters **102**, 056403 (2009), ISSN 0031-9007.
- [17] X. Liu, J. B. Oostinga, A. F. Morpurgo, and L. M. K. Vandersypen, *Electrostatic confinement of electrons in graphene nanoribbons*, Physical Review B **80**, 121407 (2009), arXiv:0812.4038.
- [18] K. Todd, H.-T. Chou, S. Amasha, and D. Goldhaber-Gordon, *Quantum Dot Behavior in Graphene Nanoconstrictions*, Nano Letters **9**, 416 (2009).
- [19] P. Gallagher, K. Todd, and D. G. Gordon, *Disorder-induced gap behavior in graphene nanoribbons*, Physical Review B **81**, 115409 (2010).
- [20] M. Y. Han, J. C. Brant, and P. Kim, *Electron Transport in Disordered Graphene Nanoribbons*, Physical Review Letters **104**, 056801 (2010).
- [21] J. B. Oostinga, B. Sacepe, M. F. Craciun, and A. F. Morpurgo, *Magneto-transport through graphene nano-ribbons* (2010), arXiv:1003.2994.
- [22] P. G. Silvestrov and K. B. Efetov, *Quantum Dots in Graphene*, Physical Review Letters **98**, 016802 (2007).
- [23] G. A. Steele, G. Gotz, and L. P. Kouwenhoven, *Tunable few-electron double quantum dots and Klein tunnelling in ultraclean carbon nanotubes*, Nature Nanotechnology **4**, 363 (2009), ISSN 1748-3387, arXiv:0907.2321.
- [24] S. Schnez, K. Ensslin, M. Sigrist, and T. Ihn, *Analytic model of the energy spectrum of a graphene quantum dot in a perpendicular magnetic field*, Physical Review B **78**, 195427 (2008).
- [25] G. A. Steele, Ph.D. thesis, Massachusetts Institute Of Technology (2006).
- [26] Y. Nazarov, private communication.
- [27] D. Gunlycke, D. A. Areshkin, and C. T. White, *Semiconducting graphene nanostrips with edge disorder*, Applied Physics Letters **90**, 142104 (2007).
- [28] Y. Yoon and J. Guo, *Effect of edge roughness in graphene nanoribbon transistors*, Applied Physics Letters **91**, 073103 (2007).
- [29] M. Evaldsson, I. V. Zozoulenko, H. Xu, and T. Heinzel, *Edge-disorder-induced Anderson localization and conduction gap in graphene nanoribbons*, Physical Review B **78**, 161407 (2008).

-
- [30] E. R. Mucciolo, A. H. C. Neto, and C. H. Lewenkopf, *Conductance quantization and transport gaps in disordered graphene nanoribbons*, Physical Review B **79**, 075407 (2009).
- [31] D. Basu, M. J. Gilbert, L. F. Register, S. K. Banerjee, and A. H. MacDonald, *Effect of edge roughness on electronic transport in graphene nanoribbon channel metal-oxide-semiconductor field-effect transistors*, Applied Physics Letters **92**, 042114 (2008).
- [32] D. Querlioz, Y. Apertet, A. Valentin, K. Huet, A. Bournel, S. G. Retailleau, and P. Dollfus, *Suppression of the orientation effects on bandgap in graphene nanoribbons in the presence of edge disorder*, Applied Physics Letters **92**, 042108 (2008).
- [33] F. Sols, F. Guinea, and A. H. C. Neto, *Coulomb Blockade in Graphene Nanoribbons*, Physical Review Letters **99**, 166803 (2007).
- [34] J. Park and P. L. McEuen, *Formation of a p-type quantum dot at the end of an n-type carbon nanotube*, Applied Physics Letters **79**, 1363 (2001).
- [35] A. V. Danilov, D. S. Golubev, and S. E. Kubatkin, *Tunneling through a multigrain system: Deducing sample topology from nonlinear conductance*, Physical Review B **65**, 125312 (2002).
- [36] I. M. Ruzin, V. Chandrasekhar, E. I. Levin, and L. I. Glazman, *Stochastic Coulomb blockade in a double-dot system*, Physical Review B **45**, 13469 (1992).
- [37] K. Mullen, E. B. Jacob, R. C. Jaklevic, and Z. Schuss, *I-V characteristics of coupled ultrasmall-capacitance normal tunnel junctions*, Physical Review B **37**, 98 (1988).
- [38] R. Wilkins, E. B. Jacob, and R. C. Jaklevic, *Scanning-tunneling-microscope observations of Coulomb blockade and oxide polarization in small metal droplets*, Physical Review Letters **63**, 801 (1989).
- [39] Y. V. Nazarov, *Coulomb Blockade without Tunnel Junctions*, Physical Review Letters **82**, 1245 (1999).

Chapter 6

Gate-defined graphene double quantum dot and excited state spectroscopy

A double quantum dot is formed in a graphene nanoribbon device using three top gates. These gates independently change the number of electrons on each dot and tune the inter-dot coupling. Transport through excited states is observed in the weakly coupled double dot regime. We extract from the measurements all relevant capacitances of the double dot system, as well as the quantized level spacing.

The contents of this chapter are partially published in *Nano Letters*:

X. L. Liu, D. Hug, and L. M. K. Vandersypen, *Gate-defined graphene double quantum dot and excited state spectroscopy*, *Nano Letters* **10**, 1623 (2010).

6.1 Motivations and introduction

Extensive efforts are made in investigating double quantum dots defined by electrostatic gates in various systems such as a GaAs two-dimensional electron gas [1, 2], semiconductor nano-wires [3] and carbon nano-tubes [4–7], with the motivation of realizing quantum computation schemes based on spins in quantum dots [8]. Graphene is a promising candidate for such applications due to the expected long spin coherence time [9, 10], and flexibility in device designs offered by its two-dimensional nature. Accidental double dots formed by disorder were found in graphene nanoribbons [11]. More recently, graphene double dot devices have been realized by etching graphene into two small islands separated by a narrow constriction, where the inter-dot coupling was shown to be tunable by a side gate [12, 13]. However, the tunability was limited partially due to the permanent presence of the constriction.

Here we define a double quantum dot device based on a graphene nanoribbon (GNR) using only local top gates. The device contains three top gates. The rightmost and leftmost top gate control the electron number on the right and left dot, respectively. A middle gate is used to tune the inter-dot coupling. The measurements exhibit familiar double dot characteristics [1]. In addition, when the inter-dot coupling is switched off by the middle gate, we observe excited states of the graphene double dot, which has not been reported before. The design principle used here can be applied for defining single and multiple quantum dots along a GNR with independent gate control over barriers and charges.

6.2 Device fabrications and measurement setup

The device is fabricated on graphene flakes deposited on a substrate by mechanical exfoliation of natural graphite [14]. The substrate consists of highly p-doped Si, covered with 285 nm thermally grown silicon dioxide. From their optical contrast against the substrate, we conclude that the flakes are single-layer [15–17]. Three electron beam lithography steps are used for fabricating the devices using PMMA as resist. First the source and drain electrodes are fabricated on selected graphene flakes. We use 5/50 nm thick e-beam evaporated Cr/Au as electrodes. In a second step, we cover the region where the GNR will be with 15 nm thick silicon dioxide using e-beam evaporation followed by lift-off. This SiO₂ layer not only acts as the etching mask for the GNR, but also forms part of the dielectric for the top gates. The GNR is then patterned by exposing it to an O₂/Ar (1:9) plasma [18] for 15 seconds¹. Without removing the SiO₂ etching mask, three local top gates, G1, G2, and G3 are fabricated in the last step. The gates consist of 5/5/20 nm thick e-beam evaporated SiO₂/Ti/Au, where an extra layer of SiO₂ is evap-

¹Other parameters used for dry etching: the O₂ and Ar flow are 3 sccm and 20 sccm, respectively; rf power is set at 20W, work pressure 6 μ bar ($V_{bias} \approx 40$ V)

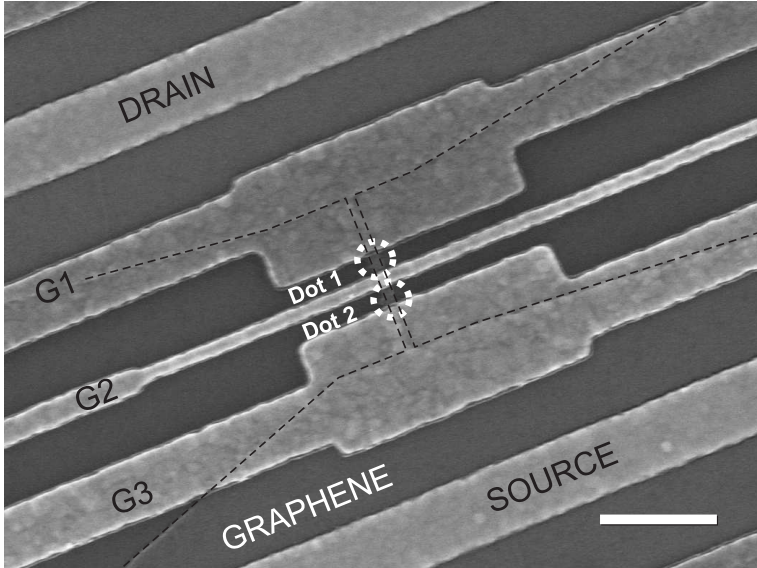


Figure 6.1: Scanning electron microscope image of a device similar to the one that is measured in this work (scale bar 400 nm). The dashed lines outline the graphene nanoribbon and the dotted lines indicate dot 1 and dot 2

orated to ensure reliable top gate operations. Here we present measurements from a device where the GNR is 800 nm long and 20 nm wide. For this device, the middle gate G2 is 40 nm in width, separated by 80 nm from gate G1 and G3 which are both 600 nm wide. Fig. 6.1 shows a scanning electron microscope image of a similar device.

For this device, we chose to make very narrow ribbon in order to obtain as large a gap as possible. And the very narrow top gate also allows higher chance of covering less "puddles".

All measurements are performed in a dilution refrigerator at a base temperature of 50 mK. The electron temperature is around 150 mK. We measure the two-terminal resistance through the top gated GNR devices by applying a DC voltage bias on the source electrode and measuring the current at the drain electrode. The degenerately doped Si substrate is grounded.

6.3 Characterization of the top gates

The GNR is intrinsically hole-doped when all gates are at zero voltage. Fig. 6.2a shows the low bias conductance as a function of G1 and G3 while G2 is fixed at zero voltage. When either of the gate voltages is above 0.5 V, current is suppressed by 3 to 4 orders

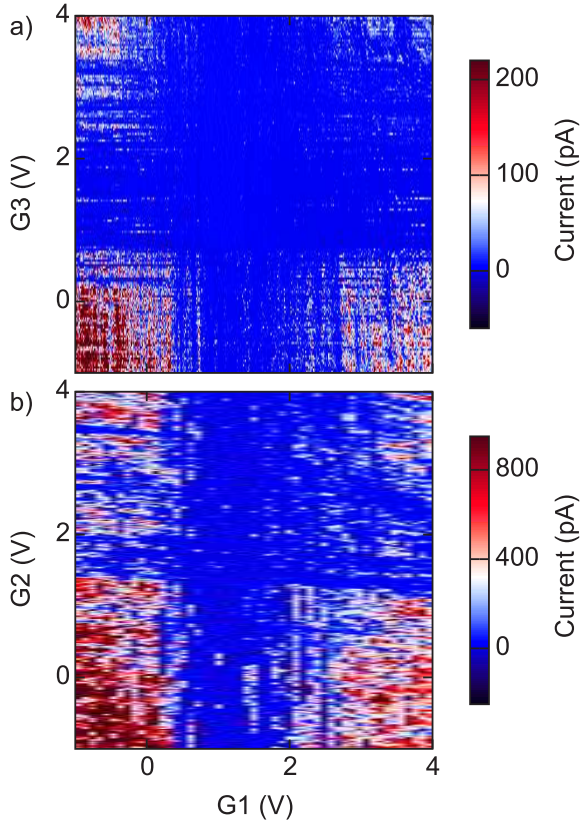


Figure 6.2: (a) Current as a function of top gate voltages V_{G1} and V_{G3} at $V_{G2} = 0$ and $V_{bias} = 100 \mu\text{V}$. (b) Current as a function of top gate voltages V_{G1} and V_{G2} at $V_{G3} = 0$, and $V_{bias} = 300 \mu\text{V}$.

of magnitude, as the Fermi level enters the transport gap locally under the top gates. The conductance increases again when the voltage on either gate is increased further to above 3 V, where the Fermi level is locally in the conduction band and the electrons that are induced in the GNR contribute to transport. The pinch-off voltage for one gate is nearly independent of the other, indicating little cross-coupling in this configuration. Similarly, Fig. 6.2b shows the low bias conductance as a function of gate $G1$ and $G2$ while $G3$ is fixed at zero voltage. Current is also suppressed by 3 to 4 orders of magnitude when the applied voltage on $G2$ is above 1.3 V. The pinch-off voltage of $G2$ is higher than that of $G1$ and $G3$, and shows a mild dependence on V_{G1} . The voltage on $G2$ is increased further up to 4 V, but the ribbon below $G2$ still does not reach heavily n-doping.

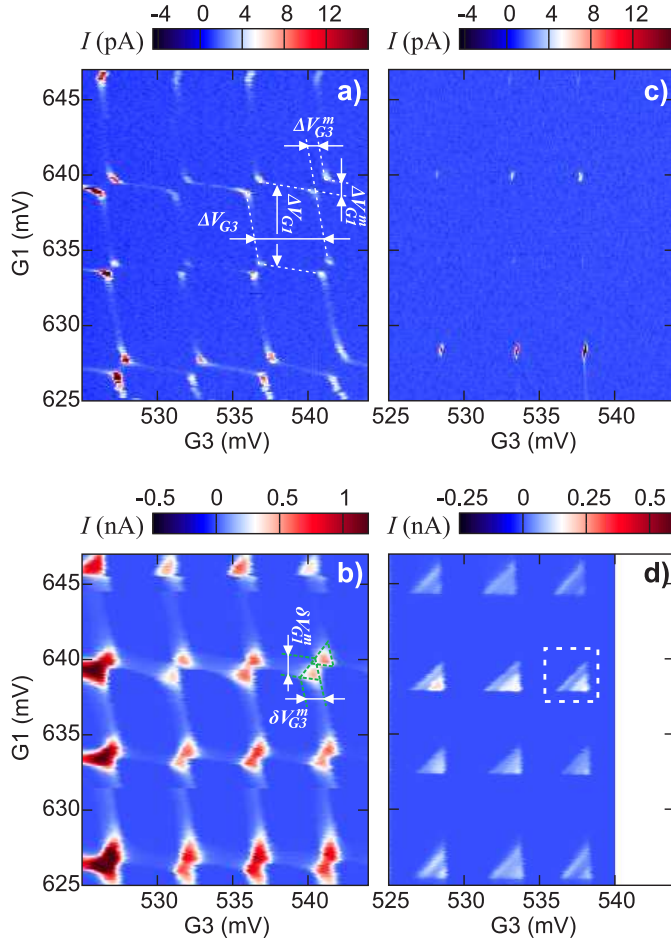


Figure 6.3: Current as a function of top gate voltages V_{G1} and V_{G3} (charge stability diagrams) in the double dot regime at (a) $V_{G2} = 1363$ mV and $V_{bias} = -15$ μ V; (b) $V_{G2} = 1363$ mV and $V_{bias} = 0.7$ mV; (c) $V_{G2} = 1380$ mV and $V_{bias} = -20$ μ V; (d) $V_{G2} = 1380$ mV and $V_{bias} = 1.35$ mV. Color scales represent the absolute value of current through the double dot. The white (a) and gray (b) dotted lines are guides to the eye showing the honeycomb patterns and the bias triangles. The relevant parameters are also illustrated in (a) and (b). The dashed line in (d) encloses the triple points where the measurements in Fig. 6.4a, 6.4b and 6.5 are taken. The two horizontal shifts at $V_{G1} = 644.5$ mV and 631.4 mV in (b) are due to charge switching events.

6.4 Top-gated double quantum dot in a graphene nanoribbon

A double quantum dot is formed when the voltages on all three gates are increased to close to pinch-off. Fig. 6.3a plots the low bias conductance as a function of the volt-

ages on G1 and G3, measured at $V_{G2} = 1363$ mV. It shows a regular honeycomb pattern characteristic of the charge stability diagram of a double quantum dot 1. The gates G1 and G3 control the number of holes on dot 1 and 2, respectively. Resonant transport occurs at the triple points. Due to co-tunneling we also measure a finite current along all boundaries of the hexagons.

From the size of the hexagons, the peak spacing in G1 and G3 is extracted to be $\Delta V_{G1} = 6$ mV and $\Delta V_{G3} = 5$ mV, respectively. Thus the capacitance from dot 1 to gate G1 is $C_{G1} \approx e/\Delta V_{G1} = 27$ aF, and that from dot 2 to gate G3 is $C_{G3} \approx e/\Delta V_{G1} = 32$ aF, assuming zero level spacing. The large capacitive coupling to these gates indicates that the dot extends far under the gates. Thus the barriers are likely to be induced by the disorder potential instead of being defined by electrostatic potentials induced by the top gates, similar to earlier work [11, 19, 20]. We estimate from the capacitance values that dot 1 (2) extends to roughly 160 nm under gate G1 (G3). Since the spacing between G1 (G3) and G2 is 80 nm and the ribbon is 20 nm wide, we then assume that the area A of each dot is around 240 nm by 20 nm. The large capacitive coupling allows G1 and G3 to change the number of carriers on dot 1 and dot 2, respectively. Assuming that holes cross over to electrons at around $V_{G1,G3} \approx 1.3$ V, we roughly estimate that in the voltage configuration of Fig. 6.3 each dot contains around 150 holes, giving a hole density $n = 3 \times 10^{12} \text{ cm}^{-2}$.

The splitting between each pairs of triple points is indicative of the coupling between the two dots. For the pair of triple points highlighted by the dashed lines in Fig. 6.3a, the splitting is $\Delta V_{G1}^m = \Delta V_{G3}^m = 0.9$ mV. When the bias voltage is increased, each triple point grows into a triangle due to inelastic transport [1], as shown in Fig. 6.3b. From the size of the triangles, we extract conversion factors between gate voltages and energy to be $\alpha_1 = eV_{bias}/\delta V_{G1} \approx 0.4e$ and $\alpha_3 = eV_{bias}/\delta V_{G3} \approx 0.4e$. The charging energy of dot 1 and dot 2 is then $E_{c1} = e^2/C_1 = \alpha_1 e/C_{G1} \approx 2.6$ meV, and $E_{c2} = e^2/C_2 = \alpha_3 e/C_{G3} \approx 2.2$ meV, respectively, where C_1 and C_2 are the total capacitances of dot 1 and dot 2. Applying a model for purely capacitively coupled double dots [1] (see also Chapter 2), we extract the inter-dot coupling capacitance $C_m = C_2 C_{G1} \Delta V_{G1}^m / e = C_1 C_{G3} \Delta V_{G3}^m / e \approx 11$ aF, and the coupling energy $E_m = e^2 / C_m (C_1 C_2 / C_m^2 - 1)^{-1} = 0.4$ meV. Table 6.1 lists also other capacitance values estimated from the hexagons (level spacing is not taken into account), where CG1-2 (G3-1) is the cross capacitance between G1 (G3) and dot 2 (dot 1).

A further change of the voltage on the gate G2 changes the inter-dot coupling. When $V_{G2} = 1380$ mV, the inter-dot coupling is practically zero, and the charge stability diagram consists of rectangular cells with overlapping triple points (Fig. 6.3c). Fig. 6.3d shows high-bias measurements in the same regime, where the pairs of triangles also overlap as a result of the small inter-dot coupling. Resonant transport through excited states is clearly visible in every triple point (the excited states are discussed further below). In this regime, we extract the energy conversion factors to gates G1 and G3 as $\alpha_1 = \alpha_3 \approx 0.6e$. The charging energies of the two dots are $E_{c1} = 3.6$ meV and $E_{c2} = 2.7$ meV,

V_{G2} (mV)	C_{G1}	C_{G3}	C_1	C_2	C_{G1-2}	C_{G3-1}
1363	27	32	59	77	5	6
1380	28	38	44	59	0	0

Table 6.1: Capacitance values (in aF) extracted from the honeycomb diagrams shown in Figure 6.3

much larger than in the previous regime of strong inter-dot coupling. Other capacitance values estimated from the stability diagram are also listed in Table 6.1, where a level spacing value of 0.5 meV is now included in the estimate.

6.5 Resonant transport through excited states of the double quantum dot

We now discuss in detail the excited-state patterns. Fig. 6.4a and 6.4b show high resolution measurements of the pair of overlapping triple points enclosed by the dashed line in Fig. 6.3d at different bias voltages. Along the baseline of the triangle the ground states of the two dots are aligned, and at the center of the baseline (point d), they lie exactly in the middle of the bias window, as illustrated by the level scheme in Fig. 6.4d. At positive bias (Fig. 6.4a), moving along a line from point d to the tip of the triangle (the detuning axis), the energy levels in dot 1 shift upwards while those in dot 2 shift downwards. At point e , the ground state of dot 1 aligns exactly with the 1st excited state of dot 2 (Fig. 6.4e), and resonant transport occurs. The non-resonant background current level is caused by inelastic processes. From these data, the level spacing of dot 2 is extracted to be around 0.6 meV in this charge configuration. At large negative bias, resonant lines parallel to the baseline are also observed (Fig. 6.4b) due to resonant transport through the ground state of dot 2 and excited states of dot 1. The level spacing of dot 1 is around 0.6 – 0.9 meV. The measured level spacing is comparable to the average level spacing estimated using $\delta E \approx 1/(D(E_F)A) \approx 0.7$ meV, where $D(E_F)$ is the density of states per unit area for 2D graphene at the Fermi energy and is calculated based on the hole density in the dot estimated earlier. For this triple point, the peak current levels of the excited state lines are slightly higher than that of the baseline, likely because the excited states are better coupled to the source / drain contacts [1, 7]. In Fig. 6.4c, we show another pair of overlapping triple points measured at a slightly different charge configuration, where the resonant current through the ground state and excited state are nearly equal.

Transport through the excited states can be analyzed more quantitatively using the result from Stoof and Nazarov for resonant tunneling [1, 21]. In the limit of weak inter-dot tunnel coupling $t_m \ll \Gamma_{i,o}$, where t_m is the inter-dot tunnel coupling, and $\Gamma_{i,o}$ are incoming and outgoing tunnel rates, the current I follows a Lorentzian line shape as a function of detuning ε , $I(\varepsilon) = (4et_m^2/\Gamma_o)/(1 + (2\varepsilon/h\Gamma_o)^2)$, with h the Plank constant.

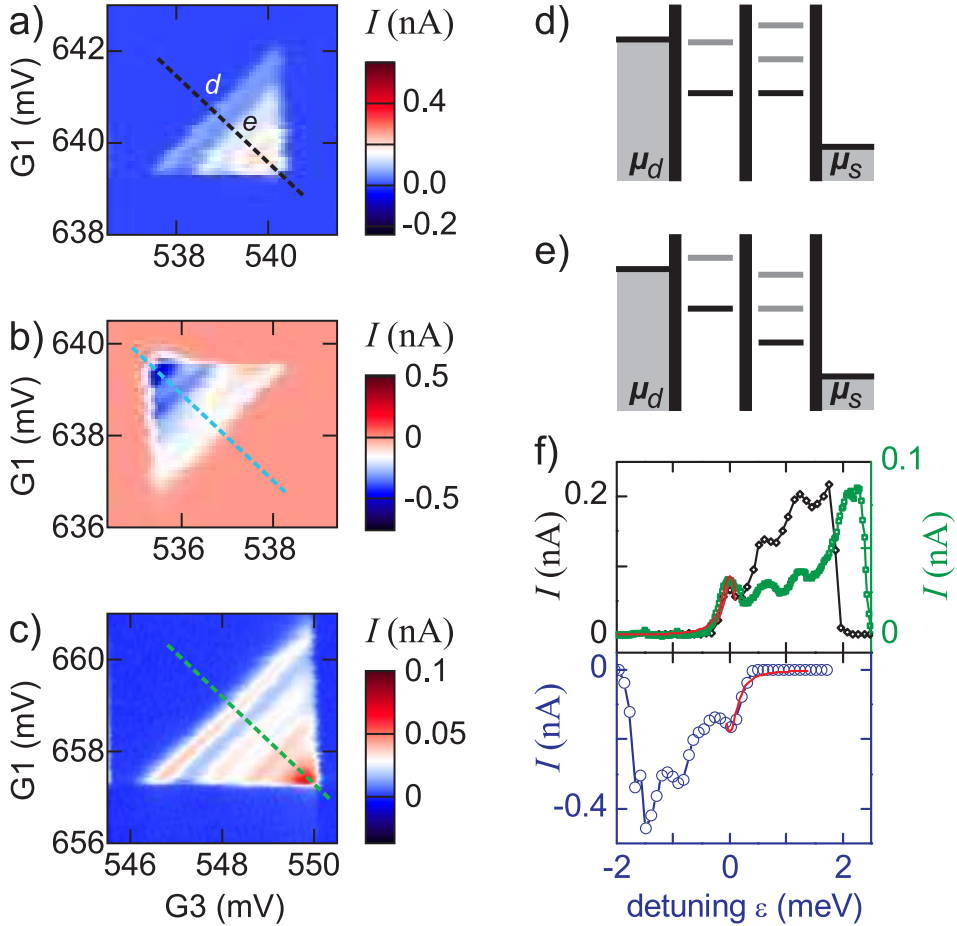


Figure 6.4: Resonant transport through excited states in the double dot. Current as a function of top gate voltages V_{G1} and V_{G3} at (a) $V_{G2} = 1380$ mV and $V_{bias} = 1.9$ mV; (b) $V_{G2} = 1380$ mV and $V_{bias} = -1.9$ mV; (c) $V_{G2} = 1370$ mV and $V_{bias} = 2.8$ mV. The dotted lines indicate the detuning axis. (d, e) Energy level schemes of the double dot corresponding to the points d and e in (a). Black solid lines represent the ground states and gray lines represent excited states. The chemical potentials of the source and drain contacts are denoted as μ_s and μ_d , respectively. (f) Line cuts along the detuning axis. The black diamonds, dark gray circles, and light gray squares are line-cuts from (a), (b), and (c), respectively. The gray solid lines are Lorentzian fits to the data points of the ground state lines outside of the bias triangle.

Fig. 6.4f plots line-cuts along the detuning axis for both positive and negative bias, and Lorentzian line fits to the ground state lines. The fitting is done for the data points outside of the bias triangle in order to minimize the contributions from the inelastic

transport [22]. We extract from the fittings a tunnel rate from dot 1 to the drain $h\Gamma_1 \approx 350 \mu\text{eV}$, from dot 2 to the source $h\Gamma_3 \approx 280 \mu\text{eV}$, and an inter-dot tunnel rate $ht_m \approx 10 \mu\text{eV}$. We note that the ground state resonance lines overlap partially with the excited state lines because the tunnel rates to the leads are comparable to the level spacing. This overlap is not taken into account for the fit.

6.6 Tuning the inter-dot coupling and the effects of disorder

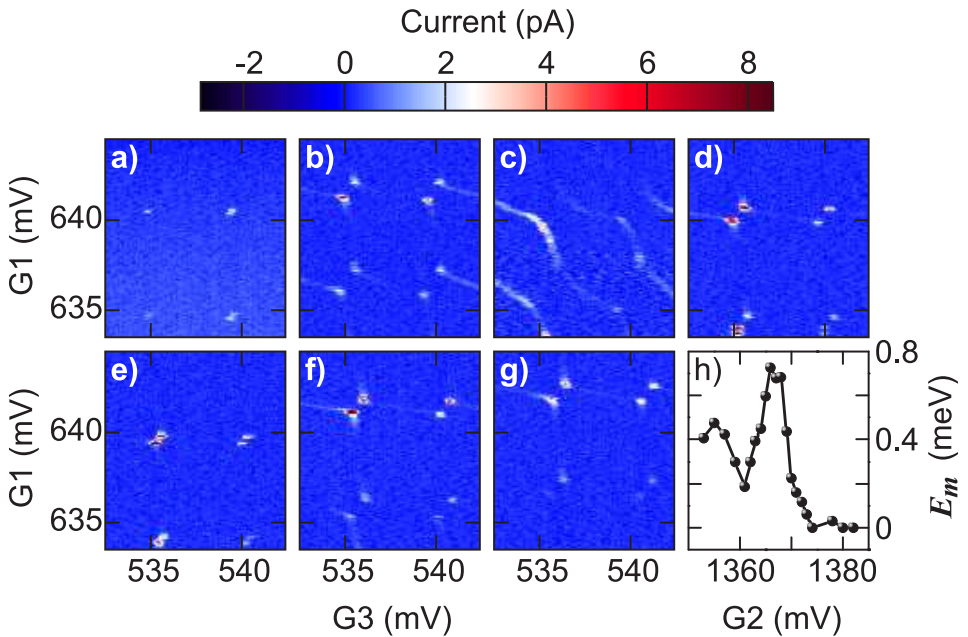


Figure 6.5: Inter-dot coupling vs. middle gate voltage V_{G2} . Current as a function of top gate voltages V_{G1} and V_{G3} at $V_{bias} = 15 \mu\text{V}$ and (a) $V_{G2} = 1373 \text{ mV}$, (b) $V_{G2} = 1369 \text{ mV}$, (c) $V_{G2} = 1367 \text{ mV}$, (d) $V_{G2} = 1363 \text{ mV}$, (e) $V_{G2} = 1361 \text{ mV}$, (f) $V_{G2} = 1359 \text{ mV}$, (g) $V_{G2} = 1357 \text{ mV}$, measured at around the same charge configuration as that of Figure 6.4a. (h) The inter-dot coupling energy E_m as a function of V_{G2} extracted from (a – g) and similar measurements.

The inter-dot coupling changes non-monotonously as a function of V_{G2} , similar to ref. [12]. Fig. 6.5 shows additional data on the evolution of the pair of triple points in Fig. 6.4a and 6.4b, as the voltage on G2 is changed in small steps. Clearly, the splitting between the triple points changes as V_{G2} is varied. This is also shown in Fig. 6.5h where the inter-dot coupling energy E_m extracted from the data is plotted as a function of V_{G2} .

The coupling energy can be tuned from around 0.7 meV down to virtually zero. However, the oscillating behavior suggests that most likely, the change of inter-dot coupling is partially due to resonances induced by disorder close to gate G2.

There is likely to be disorder close to gates G1 and G3 as well. This could be the reason for the observation that even when the voltage on G2 is fixed, the vertex splittings and the peak current of the vertices vary for different vertices rather rapidly (Fig. 6.6). It indicates that the gates G1 and G3 also change the dot-to-lead couplings in a similar non-monotonous manner as G2, in addition to controlling the number of carriers on each dot.

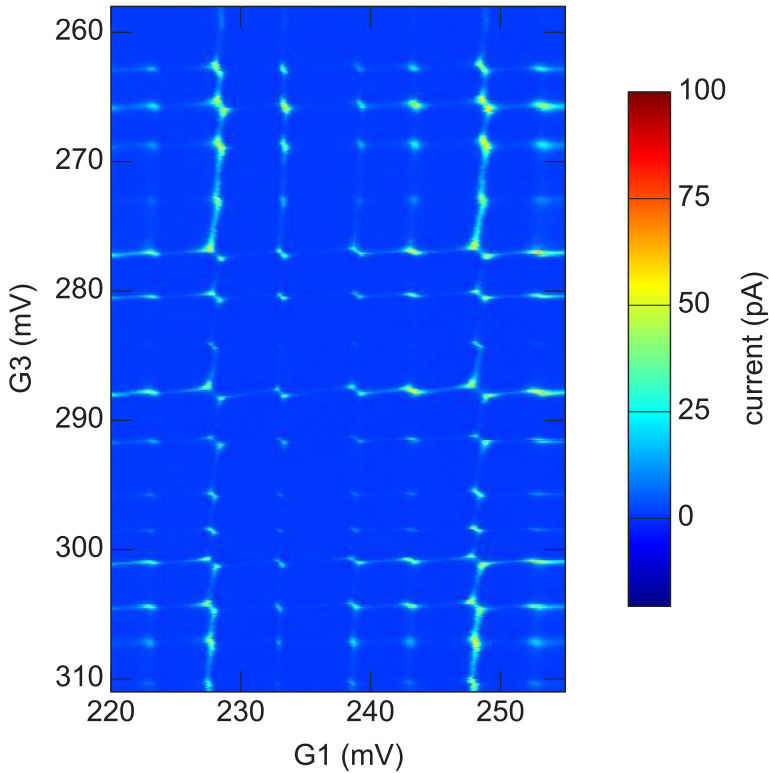


Figure 6.6: Current as a function of top gate voltages V_{G1} and V_{G3} (charge stability diagrams) in a double dot regime at $V_{G2} = 1315$ mV and $V_{bias} = 40$ μ V.

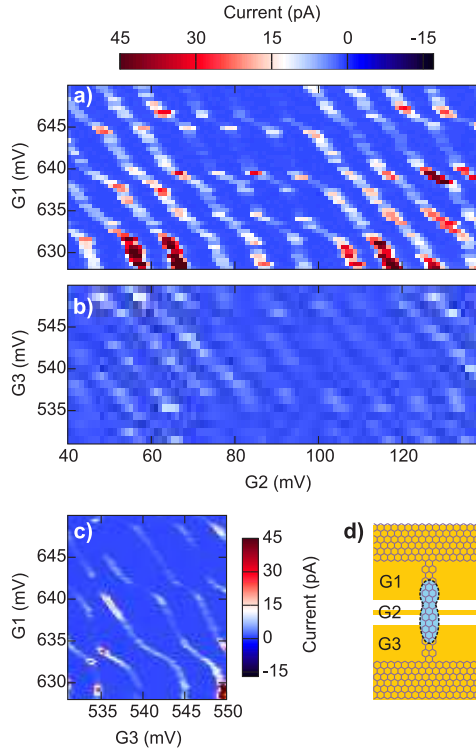


Figure 6.7: Transport in the single dot regime. (a) Current as a function of top gate voltages V_{G2} and V_{G1} at $V_{G3} = 530$ mV and $V_{bias} = 50$ μ V. (b) Current as a function of top gate voltages V_{G2} and V_{G3} at $V_{G1} = 640$ mV and $V_{bias} = 50$ μ V. (c) Current as a function of top gate voltages V_{G1} and V_{G3} at $V_{G2} = 110$ mV and $V_{bias} = 50$ μ V. (d) Illustration of the dot formation along the GNR in this configuration. The yellow rectangles represent the top gates, and the dashed lines indicate a possible position of the dot.

6.7 Form a single dot along the graphene nanoribbon

A single quantum dot is expected in the graphene nano-ribbon (GNR) when both G1 and G3 pinch off the GNR while G2 remains hole-doping. We tried to form a single dot through the ribbon by lowering the voltage on the gate G2 to close to zero, but the device could not be tuned to a regime where a well-defined single dot is formed, mainly due to strong disorder. Fig. S1c shows the low bias conductance as a function of the voltages on G1 and G3, measured at $V_{G2} = 110$ mV. We observe resonant lines approximately from top left to bottom right of the plot, indicating the formation of a quantum dot along the GNR. These lines deviate from parallel straight lines expected for a single quantum dot, indicating that the potential landscape in the dot deviates from that of an

ideal single dot. We can nevertheless extract the peak spacing in gate G1 and G3 to be $\Delta V_{G1} \approx \Delta V_{G3} \approx 5$ mV. It follows that the capacitances from the dot to the gate G1 and G3 are $C_{G1} \approx C_{G3} \approx 32$ aF, close to the capacitance value in the double dot regime.

We now estimate roughly how far the dots extend below G1 and G3 in the "single dot" regime from comparison of C_{G1} and C_{G3} to C_{G2} . Since the value of C_{G1} and C_{G3} are about the same in the single and double dot regimes, this allows us to also obtain a rough estimate of the dot areas in the double dot regime as well.

Fig. 6.7a (6.7b) shows the low bias conductance as a function of the voltages on gates G2 and G1 (G3), measured at $V_{G3} = 530$ mV ($V_{G1} = 640$ mV). The peak spacing and the resulting capacitance to gates G1 and G3 remain the same as those from Fig. 6.7c, as expected. The peak spacing in gate G2 is $\Delta V_{G2} \approx 10$ mV, so the resulting capacitance to gate G2 is $C_{G2} \approx 16$ aF. Given that G2 is 40 nm wide and is separated from the GNR by about 20 nm, and with a GNR width of 20 nm, we estimate that G2 effectively controls the dot potential over an area of 80 nm by 20 nm (we hereby make the reasonable assumption that the single dot wave function extends fully across the segment of the GNR below G2). Based on the relative lever arm between the gates, $C_{G1, G3}/C_{G2} \approx 2$, we then estimate the dot area underneath gates G1 and G3 to be around twice as large, namely, 160 nm by 20 nm. The total area of each of the dots in the double dot regime is then approximately 240 nm by 20 nm.

The dot area can in principle be extracted from the measured $C_{G1, G3}$ values and the device geometry based on electrostatic calculations [23]. However, the calculated capacitance between the entire GNR and G2 (for which the geometry is well defined) is $C_{G2}^{cal} = 10$ aF using a dielectric constant of 3.9 for SiO₂ and the intended dielectric thickness of 20 nm. This is 1.5 times smaller than the measured capacitance to the dot. It suggests that either the actual gate dielectric is thinner than 20 nm or has a different dielectric constant. This is possible because the thickness of the dielectric from the fabrication is not well calibrated, and the dielectric constant of the evaporated SiO₂ is likely to be different from that of the bulk value. An estimate of the dot area based on calculation is thus less applicable.

Fig. 6.8 shows coulomb diamonds measured in this single dot regime. The charging energy of this single dot is around 2 meV, much smaller than that of the double dot, as expected. From the excited state lines, we extract a level spacing of around 0.5 meV for this dot.

6.8 Conclusions

In conclusion, a double quantum dot device is realized in a graphene nanoribbon with multiple top gates. Resonant transport through excited states is observed. The inter-dot coupling strength is tunable over a wide range by the middle gate, although the

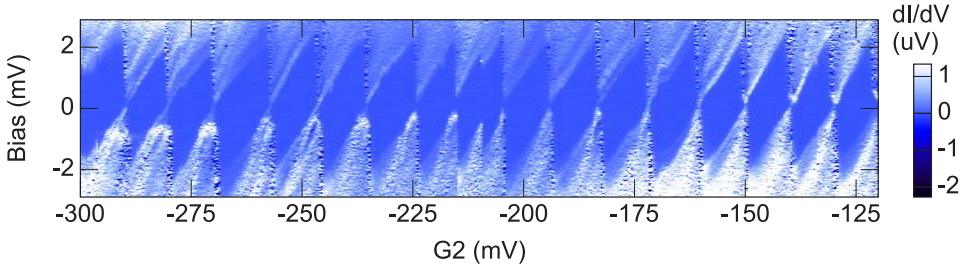


Figure 6.8: Differential conductance dI/dV as a function of V_{TG} and V_{bias} (Coulomb diamonds) measured at the same single dot regime as in Fig. 6.7, at $V_{G1} = 540$ mV and $V_{G3} = 631$ mV.

coupling changes non-monotonously with gate voltage as a result of disorder. Therefore, further progress is needed in order to suppress the influence of disorder on the tunability of the device. We also anticipate that adding two more gates to the left and right dots would allow one to control the number of charges on the two dots and the barriers to the leads separately, which would further improve the controllability of a graphene double dot device. The device demonstrated here represents an important step towards the manipulations of single charges and spins in graphene quantum dots.

6.9 Additional information

6.9.1 Charge stability diagram of the double dot in different configurations

In Fig. 6.9, we tuned the device to a different regime by lowering the voltages on gate G1 and G3 such that more holes are induced to the dot. Well defined charge stability diagrams for a double dot are again observed. Similar to the previous measurement, also in this regime we could tune the inter-dot coupling with gate G2. When $V_{G2} = 1275$ mV (Fig. 6.9a), current peaks of different charge states run almost parallel to each other as gate G1 and G3 are swept, indicating that dot 1 and 2 are strongly coupled such that they behave almost like a single dot in this regime. An increase of V_{G2} to 1307 mV (Fig. 6.9b) decreases the inter dot coupling and the charge stability diagram resembles a honeycomb. A further increase of the voltage on gate G2 to 1315 mV decouples the two dots (Fig. 6.9b). We notice that in this case the overall current level through the double dot is higher than the measurements shown in Fig. 6.3a and c, reflecting a higher tunnel rate between the dot and the leads. This is an indication that the tunnel coupling to the leads can be changed by the gates G1 and G3.

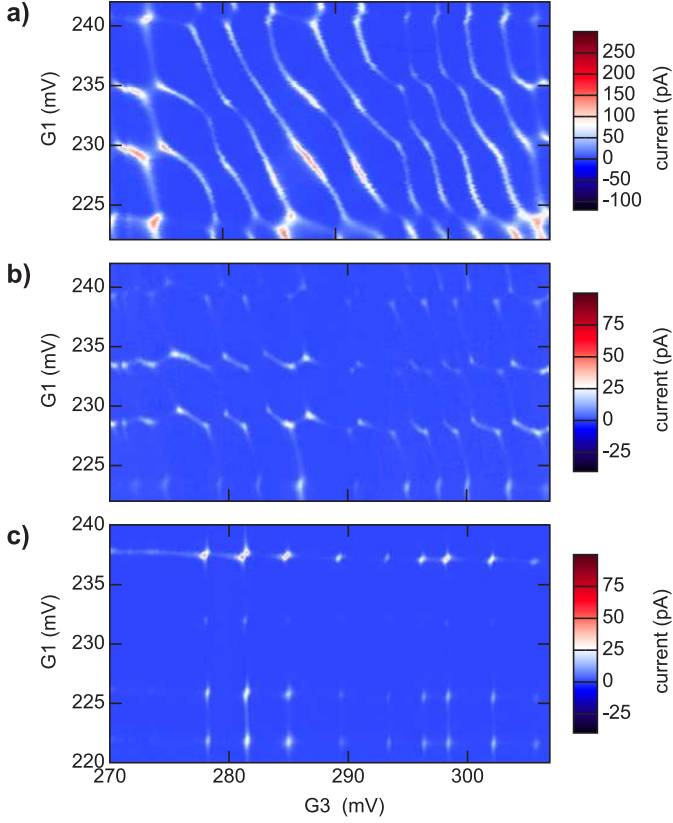


Figure 6.9: Current as a function of top gate voltages V_{G1} and V_{G3} (charge stability diagrams) in a double dot regime at (a) $V_{G2} = 1275$ mV and $V_{bias} = 30$ μ V; (b) $V_{G2} = 1307$ mV and $V_{bias} = 40$ μ V; (c) $V_{G2} = 1315$ mV and $V_{bias} = 40$ μ V. Color scales represent the current level through the double dot.

6.9.2 Estimates of the level spacing

The Fermi energy is given by

$$E_F = \hbar v_F \sqrt{\pi n} = 1.17 \text{e-}9 \text{ eV} \cdot \text{m} \sqrt{n}$$

with n the density:

$$\begin{aligned} n &= C_g(V_g - V_{NP})/eA \\ &= (1/A)(V_g - V_{NP})/\Delta V_g \end{aligned}$$

where A is area, ΔV_g is the Coulomb peak spacing, V_{NP} is the gate voltage at the charge neutrality point or the electron-hole cross over point, V_g is the applied gate voltage.

Thus if $A = [180, 240] \text{ nm} \times 20 \text{ nm}$, $\Delta V_g = 6 \text{ mV}$, $V_g - V_{NP} = (1.3 - 0.5) \text{ V}$, then total number of carriers is 133, and

$$n = [3.7\text{e}12, 3.1\text{e}12] \text{ cm}^{-2}$$

$$E_F = [225, 207] \text{ meV}$$

The density of states per unit volume for 2D graphene is

$$D(E) = \frac{fE}{2\pi(\hbar v_F)^2}$$

$$= 36.6e-4 f E (\text{meV} \cdot \text{nm})^{-2}$$

where $f=4$ is the degeneracy.

Finally, we find the following estimate for the level spacing

$$\delta E = 1/D(E_F)A$$

$$= \frac{f}{\hbar v_F} \sqrt{\pi n}$$

$$= [0.8, 0.7] \text{ meV}$$

References

- [1] W. G. van der Wiel, S. De Franceschi, J. M. Elzerman, T. Fujisawa, S. Tarucha, and L. P. Kouwenhoven, *Electron transport through double quantum dots*, Reviews of Modern Physics **75**, 1 (2002).
- [2] R. Hanson, L. P. Kouwenhoven, J. R. Petta, S. Tarucha, and L. M. K. Vandersypen, *Spins in few-electron quantum dots*, Reviews of Modern Physics **79**, 1217 (2007).
- [3] C. Fasth, A. Fuhrer, M. T. Björk, and L. Samuelson, *Tunable Double Quantum Dots in InAs Nanowires Defined by Local Gate Electrodes*, Nano Letters **5**, 1487 (2005).
- [4] N. Mason, M. J. Biercuk, and C. M. Marcus, *Local Gate Control of a Carbon Nanotube Double Quantum Dot*, Science **303**, 655 (2004).
- [5] M. J. Biercuk, S. Garaj, N. Mason, J. M. Chow, and C. M. Marcus, *Gate-Defined Quantum Dots on Carbon Nanotubes*, Nano Letters **5**, 1267 (2005).
- [6] M. R. Gräber, M. Weiss, S. Oberholzer, and C. Schönenberger, *Defining and controlling double quantum dots in single-walled carbon nanotubes*, Semiconductor Science and Technology **21**, S64 (2006), ISSN 0268-1242.

- [7] S. Sapmaz, C. Meyer, P. Beliczynski, P. Jarillo-Herrero, and L. P. Kouwenhoven, *Excited State Spectroscopy in Carbon Nanotube Double Quantum Dots*, Nano Letters **6**, 1350 (2006).
- [8] D. Loss and D. P. DiVincenzo, *Quantum computation with quantum dots*, Physical Review A **57**, 120 (1998).
- [9] B. Trauzettel, D. V. Bulaev, D. Loss, and G. Burkard, *Spin qubits in graphene quantum dots*, Nature Physics **3**, 192 (2007), ISSN 1745-2473.
- [10] J. Fischer, B. Trauzettel, and D. Loss, *Hyperfine interaction and electron-spin decoherence in graphene and carbon nanotube quantum dots*, Physical Review B **80**, 155401 (2009).
- [11] K. Todd, H.-T. Chou, S. Amasha, and D. Goldhaber-Gordon, *Quantum Dot Behavior in Graphene Nanoconstrictions*, Nano Letters **9**, 416 (2009).
- [12] F. Molitor, S. Dröscher, J. Güttinger, A. Jacobsen, C. Stampfer, T. Ihn, and K. Ensslin, *Transport through graphene double dots*, Applied Physics Letters **94**, 222107 (2009).
- [13] S. Moriyama, D. Tsuya, E. Watanabe, S. Uji, M. Shimizu, T. Mori, T. Yamaguchi, and K. Ishibashi, *Coupled Quantum Dots in a Graphene-Based Two-Dimensional Semimetal*, Nano Letters **9**, 2891 (2009).
- [14] K. S. Novoselov, A. K. Geim, S. V. Morozov, D. Jiang, Y. Zhang, S. V. Dubonos, I. V. Grigorieva, and A. A. Firsov, *Electric Field Effect in Atomically Thin Carbon Films*, Science **306**, 666 (2004).
- [15] D. S. L. Abergel, A. Russell, and V. I. Fal'ko, *Visibility of graphene flakes on a dielectric substrate*, Appl. Phys. Lett. **91**, 063125 (2007).
- [16] P. Blake, E. W. Hill, A. H. Castro Neto, K. S. Novoselov, D. Jiang, R. Yang, T. J. Booth, and A. K. Geim, *Making graphene visible*, Appl. Phys. Lett. **91**, 063124 (2007).
- [17] J. B. Oostinga, H. B. Heersche, X. Liu, A. F. Morpurgo, and L. M. K. Vandersypen, *Gate-induced insulating state in bilayer graphene devices*, Nature Materials **7**, 151 (2007), ISSN 1476-1122.
- [18] C. Stampfer, J. Güttinger, F. Molitor, D. Graf, T. Ihn, and K. Ensslin, *Tunable Coulomb blockade in nanostructured graphene*, Appl. Phys. Lett. **92**, 012102 (2008).
- [19] C. Stampfer, J. Güttinger, S. Hellmüller, F. Molitor, K. Ensslin, and T. Ihn, *Energy Gaps in Etched Graphene Nanoribbons*, Physical Review Letters **102**, 056403 (2009), ISSN 0031-9007.

-
- [20] X. Liu, J. B. Oostinga, A. F. Morpurgo, and L. M. K. Vandersypen, *Electrostatic confinement of electrons in graphene nanoribbons*, Physical Review B **80**, 121407 (2009), [arXiv:0812.4038](#).
- [21] T. H. Stoof and Yu, *Time-dependent resonant tunneling via two discrete states*, Physical Review B **53**, 1050 (1996).
- [22] G. A. Steele, G. Gotz, and L. P. Kouwenhoven, *Tunable few-electron double quantum dots and Klein tunnelling in ultraclean carbon nanotubes*, Nature Nanotechnology **4**, 363 (2009), ISSN 1748-3387, [arXiv:0907.2321](#).
- [23] G. A. Steele, Ph.D. thesis, Massachusetts Institute Of Technology (2006).

Chapter 7

Quantum Hall effect in graphene Josephson junctions

Josephson junctions are fabricated on graphene using a high H_{c2} superconductor NbTiN as contacts. The junctions exhibit tunable supercurrent and a high critical current density of up to $110 \text{ nA}/\mu\text{m}$ at $T = 50\text{mK}$. We study the magneto-transport properties of the device in a perpendicular field of up to 11 T where the superconducting contacts remain superconducting at 50 mK . The device shows two-terminal quantum Hall effect. We observe resistance fluctuations and Coulomb charging effects on the Hall plateaus which are attributed to resonant tunneling through the bulk insulating states in the quantum Hall regime. The temperature dependence of the magneto-resistance suggests that in these samples Andreev reflections do not contribute significantly to the results at high magnetic fields.

7.1 Introduction

Hybrid systems consisting of a superconductor in contact with a two-dimensional electron gas (2DEG) have attracted considerable interest, because of the conversion of electrons into holes through Andreev reflections (AR) at such interfaces, as well as the fascinating properties of the 2DEGs such as the high degree of control and tunability [1–3]. High mobility 2DEG systems also exhibit quantum Hall effect (QHE) at low temperatures. In the quantum Hall regime, electrons in the 2DEGs are quantized in Landau levels and only the edge states carry current. It is interesting to study how AR would influence the edge states when the 2DEG is in contact with a superconductor.

A number of theoretical works have investigated the transport properties of a semiconductor-superconductor interface in a high perpendicular magnetic field where Landau level quantization is important [4–7]. An electron wave that travels in skipping orbits is expected to experience multiple Andreev reflections along the NS interface. At the exit of the NS interface, the state is of both electron and hole character. Such microscopic processes modify the magneto-resistance of the sample. For a moderately disordered NS interface, the two terminal resistance is predicted to oscillate periodically in the filling factor ν with a larger oscillation amplitude than that of Shubnikov-de Haas (SdH) oscillations in the high filling factor regime [5–7]. In the low filling factor regime, numerical studies show that the conductance oscillations become uncorrelated in the filling factor [4]. The theoretical aspects are discussed in more detail in section 2.5.2 of this thesis.

The combination of AR and QHE is very challenging experimentally. The challenge is two-fold. First, superconductivity does not usually coexist with high magnetic fields as the critical field of most superconductors is rather low. Secondly, systems that show quantum Hall effect are typically two dimensional electron gases in semiconductors which often do not make good contact with superconductors due, for instance, to the presence of Schottky barriers (with the exception of InAs 2DEGs). The first challenge was met rather early when type II superconductors were discovered. The H_{c2} of some superconducting materials, such as Nb, NbN, NbTiN, TiV, Sn, can be as large as a few Tesla ¹.

Significant progress was achieved in coping with the second challenge during the past decade. Several research groups are able to contact high mobility two dimensional electron gases (2DEG) in InAs with superconductors [1, 2], and study the transport properties of the semiconductor-superconductor interfaces in high magnetic fields [8–12]. However, existing experiments are all performed in the regime with high filling factors, where the "quantum" effect is not yet important. Besides, even though it is possible, it is still extremely difficult to have high mobility InAs 2DEG simultaneously with transparent superconducting contacts.

Graphene turns out to be an ideal candidate for studying Andreev reflections in the quantum Hall regime. Robust QHE has been observed in graphene [13–16] and rou-

¹Many of these materials are used for building superconducting magnets.

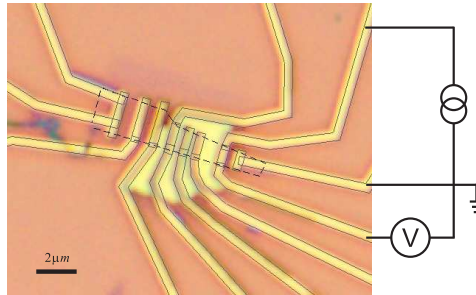


Figure 7.1: Optical microscope image of the device measured in this work. The dashed line outlines the graphene flake, and the solid gray lines outline the designed electrodes. We notice that the lift-off of the device was not complete, as a large bulk of metal remains on the left of this device. Most measurements presented here use a quasi three-terminal geometry with current bias as illustrated in the graph, unless stated otherwise.

tinely reproduced in many labs, owing mainly to the large Landau level separations in graphene and to the fact that the electronic system is strictly 2D in graphene. Meanwhile, supercurrents have been observed in Josephson junctions on graphene by several research groups [17–21]. Graphene makes good electric contact with many superconductors and normal metals² perhaps because it has zero bandgap. In addition, compared to InAs 2DEG, the carrier density of graphene is tunable by an electrostatic gate all the way from the hole regime through zero density to the electron regime. This allows one to reach the real *quantum* Hall regime with filling factors down to ± 2 , ± 6 , etc. Combining all these properties, namely, a gate tunable graphene transistor with high H_{c2} superconducting contacts in a high magnetic field, one could study how two, six or more edge channels interact with a superconductor.

For the work described in this chapter, we fabricate graphene transistors with two NbTiN contacts. The carrier density in graphene is controlled by the back gate. The devices behave as Josephson junctions with tunable supercurrent in the low field regime and show QHE in high fields. The magneto-transport properties of the device are studied as a function of carrier density and temperature in an external perpendicular magnetic field of up to 11 T. This work represents an important step towards further study of AR in the quantum Hall regime in graphene.

7.2 Fabrication and device characterization

The devices are fabricated on monolayer graphene flakes deposited on a substrate by mechanical exfoliation of natural graphite [14] as described in chapter 3 of this thesis.

²We found that graphene can be contacted by Ti, Au, Pd, Cr, Co, Pt. Only Al does not make contact to graphene, but that could be due to the morphology of the Al film.

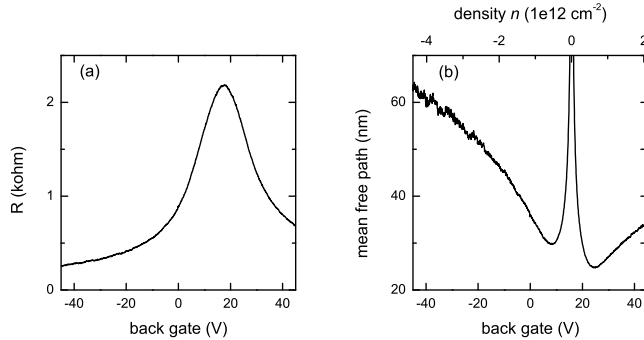


Figure 7.2: (a) Two terminal resistance as a function back gate voltage measured with 100 nA current bias at room temperature and zero magnetic field. A series resistance of 18.3 k Ω is subtracted for the plot as described in the text. (b) Calculated mean free path as a function of back gate voltage using the data from (a). The corresponding carrier densities at different back gate voltages are indicated in the top axis using a back gate capacitance of $7 \times 10^{10} e \text{ cm}^{-2}/V$, where negative (positive) values represent hole (electron) densities.

The substrates consist of highly p-doped Si, capped by 285 nm thermally grown silicon dioxide. The substrates thus act as a back gate (BG). We spun a thin layer of HMDS on the substrate prior to the deposition of graphene [22]. E-beam lithography is used for patterning both superconducting and normal contacts with PMMA as a resist. We use 8/70 nm thick e-beam evaporated Ti/AuPd as normal metal contacts, whereas the fabrication of the superconducting contacts consists of mainly three steps. First a 25 nm thick Ti layer is deposited on graphene (that is selectively covered with PMMA for lithography purposes) using e-beam evaporation. This Ti layer both ensures a transparent contact to graphene and protects graphene from being damaged by the subsequent processing steps. The sample is then taken out of the evaporator and moved to a sputtering system. In the second step, the substrate is cleaned for 450 seconds using an Ar plasma to remove any oxides or contaminations on the surface. Approximately 20 nm thick Ti is left after this sputter-cleaning step. In the last step, 15 nm NbTiN is sputtered from a Nb_{0.7}Ti_{0.3} target in an environment of Ar/N plasma [23], without breaking the vacuum (sputtering time 17 seconds). Only after this last sputtering step, all samples with multiple layers (PMMA, Ti, and NbTiN) crack significantly, which however does not show discernible influence on the device performance, probably because the area where the electrodes will be consists of only the Ti/NbTiN layer (no PMMA layer) and usually shows no cracks. We notice that there are also no cracks within the regions with only PMMA and NbTiN (no Ti layer). A similar behavior was found with Ti/Al protecting layers or with ZEP as a resist, where actually more severe cracks were found. The cracks are likely to be caused by stress.

A two terminal device-layout is adopted for this work, with both contacts going across the entire flake. We investigated six devices with both contacts superconduct-

Label	<i>A</i>	<i>B</i>	<i>C</i>	<i>D</i>	<i>E</i>	<i>F</i>
width w (μm)	3	3	3	1.8	1.8	0.8
length L (μm)	0.4	0.4	0.4	0.7	0.5	0.4

Table 7.1: The dimensions of six SGS devices. All superconducting contacts are 400 nm wide.

ing (SGS), three devices with both contacts normal (NGN), and six devices with one superconducting and one normal metal contact (SGN) on several monolayer graphene flakes. All SGN devices are 3 μm in width and 500 nm in length (the spacing between the N and S contacts), which are all fabricated on the same flake. The dimensions of the SGS devices (*A* to *F*) are summarized in Table 7.1. Most measurements presented in this chapter are taken from device *F* which is shown in Fig. 7.1).

All measurements are performed in a dilution refrigerator with a base temperature of 50 mK. Each measurement wire of the fridge goes through a room temperature (RT) π filter, a two stage RC filter at low temperature, and a copper powder filter at low temperature before reaching the device. The DC resistance of each wire is around 2.53 k Ω and the electron temperature is around 150 mK [24]. For device *F*, we measure either the two-terminal resistance or a quasi-three-terminal resistance using current bias as illustrated in Fig. 7.1.

The RT resistance of graphene R as a function of the back gate voltage for device *F* is shown in Fig. 7.2a. A series resistance $R_{series} = 18.3$ k Ω is subtracted from the raw data (two-terminal resistance) to generate the plot. The series resistance is a sum of the DC resistance of the filters (2×2.53 k Ω for the two wires, extracted from the supercurrent measurements as described in Sec. 7.3), contact resistance, and the resistance of the NbTiN leads. The resistance of the two NbTiN leads are taken to be 13.2 k Ω in total, obtained from comparing the RT resistance with the resistance at $T = 50$ mK where the NbTiN leads are superconducting. The contact resistance is small for this device as indicated by the observation of the supercurrent. The charge neutrality point is around $V_{CNP} = 16$ V at RT and the carrier mobility is around 3000 $\text{cm}^2/\text{V}\cdot\text{s}$ for this device. When cooled down to base temperature, the charge neutrality point shifts to around 12 V. The reason for this shift is unclear.

For the high carrier density regime, the mean free path l_{MFP} can be calculated using the relation $l_{MFP} = (\sigma h/2e^2)/\sqrt{\pi n}$ where $\sigma = L/wR$ is the conductivity of graphene and n is the carrier density of graphene. In Fig. 7.2b, we plot the estimated mean free path as a function of the back gate voltage (which is proportional to the carrier density of graphene n as indicated by the top axis) using data from Fig. 7.2a. We see that the mean free path is in the range of 30 nm to 60 nm depending on the back gate voltage, which is about one tenth of the device length $L = 400$ nm. The device is thus in the diffusive transport regime. Note that the divergence close to the charge neutrality point occurs because the relation that we used for estimating the mean free path is no longer valid in the low density regime.

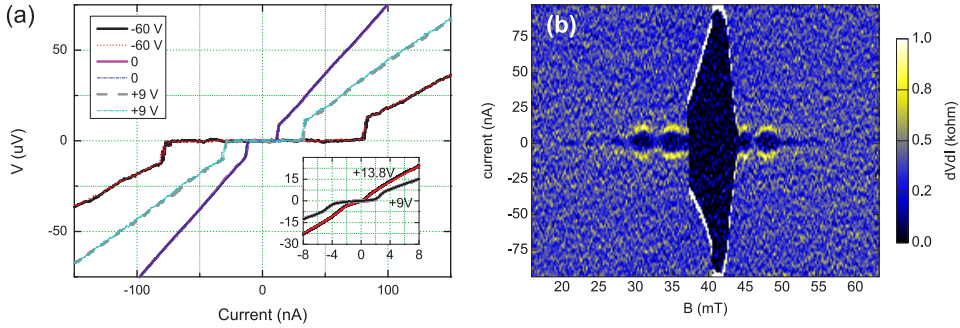


Figure 7.3: Characterization of the Josephson junction. (a) Voltage (V) versus current (I) characteristics at several back gate voltages for both sweeping up (thick solid lines) and down (thin broken lines) at zero field and 50 mK. Inset: IV characteristics around V_{CNP} . The back gate voltages corresponding to each curve are indicated in the graph. (b) Fraunhofer pattern at $V_{BG} = -60\text{ V}$ and $T = 50\text{ mK}$. The zero of the magnet power supply is offset by 40 mT. A three-terminal geometry as illustrated in Fig. 7.1a is used for both measurements. And a series resistance of 2.53 k Ω is subtracted from the raw data to generate the plot.

7.3 Josephson junctions in graphene

At base temperature $T = 50\text{ mK}$ and at temperatures up to $T = 1\text{ K}$, we measured proximity induced Josephson current through the device. Fig. 7.3a shows the IV characteristics at several back gate voltages. (Note that for the three-terminal measurements, we routinely subtract from the raw data a series resistance of 2.53 k Ω due to the filters from each measurement wire.) Clear signs of supercurrents are observed up to a critical current of around 100 nA at $V_{BG} = -60\text{ V}$ where the hole density is $5 \times 10^{12}\text{ cm}^{-2}$, corresponding to a critical current density of 110 nA/ μm at 50 mK. The IV characteristic is non-hysteretic with respect to the sweeping directions and is symmetric for positive and negative bias current. Similar behavior is observed in devices A , B , C , and E . Device D does not show supercurrent.

When a magnetic field is applied perpendicular to the plane, the critical current exhibits an oscillatory Fraunhofer-like pattern as shown in Fig. 7.3b. This confirms that a Josephson current flows through the device. The Josephson current also provides us with a tool to calibrate the zero voltage of the system. The critical current as a function of perpendicular magnetic field as shown in Fig. 7.3b deviates from the standard Fraunhofer diffraction pattern [25]. In addition, sharp jumps in the critical current such as those at $B = 37\text{ mT}$ and $B = 40\text{ mT}$ occur at random fields for different measurement runs. Both are indications of the influence from the trapped fluxes near the junction. We can nevertheless extract a junction area of around $0.24\text{ }\mu\text{m}^2$ from the magnetic field dependence, which is slightly smaller but similar to the actual junction area of $0.34\text{ }\mu\text{m}^2$.

Fig. 7.3a also clearly shows that the critical current depends strongly on the back

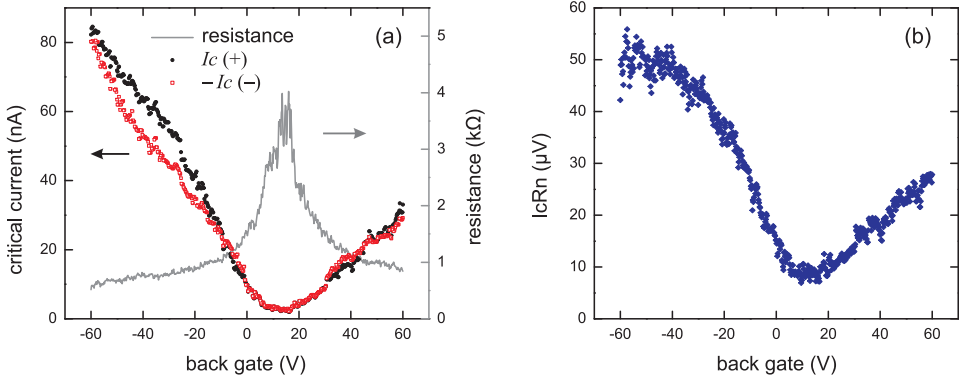


Figure 7.4: (a) The critical current for positive ($I_c(+)$, black filled circles) and negative ($I_c(-)$, gray open squares) bias as a function of the back gate voltages. The gray solid line shows the normal state resistance measured using the three-terminal geometry with 10 nA current bias at 50 mK. A magnetic field of 100 mT is applied to suppress the supercurrent. A series resistance of 2.53 kΩ is subtracted from the raw data for the plot. (b) The $I_c R_n$ product of the junction as a function of the back gate voltage, calculated using the data from (a), where $I_c = I_c(+)$.

gate voltages and decreases when the electron or hole density decreases. This verifies that the observed Josephson current flows through graphene. For device *B*, *E*, and *F*, the differential resistance of the device close to the charge neutrality point is nonzero at all bias values as shown in the inset of Fig. 7.3a. This is not the case for devices *A* and *C* where a dissipationless Josephson current is observed at all back gate voltages. The absence of supercurrent close to the charge neutrality point for some devices is likely to be a result of the noise level of the fridge or trapped flux.

The observation of the Josephson current through graphene proves that at low field, Andreev reflection takes places at the NS interface of our devices. In these SGS devices we do not observe multiple Andreev reflections [26] such as reported by refs. [17, 19].

The critical currents $I_c(\pm)$ of our Josephson junction device as a function of the back gate voltage are summarized in Fig. 7.4a. The values for the critical current are taken to be the current bias where the differential resistances dV/dI show peaks. Note that for the low density regime close to V_{CNP} , even though the differential resistance does not vanish at low bias, we still observe clear "kinks" in the IV characteristics as shown in the inset of Fig. 7.3a, which give rise to peaks in the dV/dI versus bias curves. The critical current in Fig. 7.4a is thus finite for all back gate voltages. The strong dependence of the critical current on the back gate voltage is clearly shown. We observe that the critical currents at positive and negative bias are very similar or identical for the same back gate voltage.

We next estimate the $I_c R_n$ product of our junction. The normal state resistance R_n is measured after applying an external magnetic field of 100 mT to suppress the

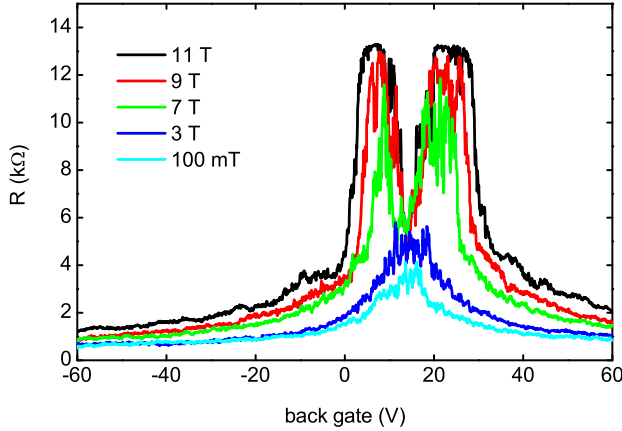


Figure 7.5: Resistance as a function of the back gate voltage for different magnetic field as indicated in the graph, at temperature $T = 50$ mK. A quasi-three-terminal geometry (see Fig. 7.1) with a current bias of 10 nA is used for this measurement. A series resistance of 2.53 k Ω is subtracted from the raw data as usual.

superconductivity. The three terminal resistance is shown in Fig. 7.4a with the gray solid line where 2.53 k Ω series resistance is subtracted as usual. Using the measured critical current at positive bias $I_c(+)$ to approximate the critical current I_c , we obtain the $I_c R_n$ values at different back gate voltage, as plotted in Fig. 7.4b. We see that the $I_c R_n$ product is strongly back gate dependent and is rather low (in the range of 10 μ V to 40 μ V) compared to the expectations for a diffusive junction [25, 27]. The former is related to the change in mean free path as a function of the back gate voltage [19]. The later is partially because the critical current extracted from the measurements is much lower than the actual critical current of the junction due to the presence of trapped flux near the junction [28] and / or the noise level of our experimental setup [19]. Further investigation is needed in order to clarify this result.

7.4 Two terminal quantum Hall effect in the presence of superconductors

Having established that Andreev reflections take place in the low magnetic field regime for our device, we next investigate the quantum Hall effect (QHE) in the high magnetic field regime. Fig. 7.5 shows the quasi-three-terminal resistance of our device as a function of the back gate voltage (density) measured at different magnetic fields. At $B = 11$ T, the two plateaus at filling factors $\nu = \pm 2$ are clearly developed at resistance $h/2e^2 =$

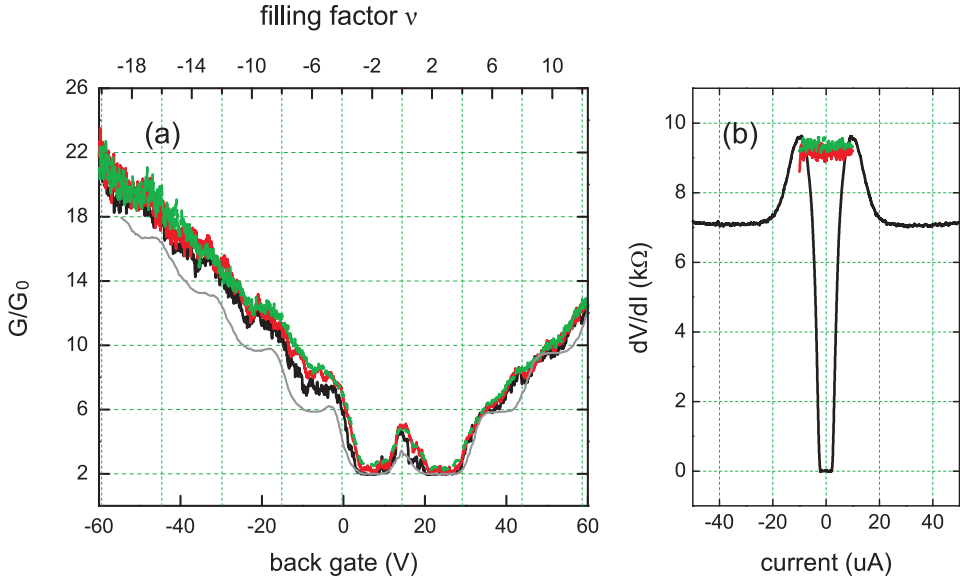


Figure 7.6: Temperature dependence of the quantum Hall effect (a) and the resistance of the superconducting leads (b). (a) Three-terminal conductance of graphene as a function of the back gate voltage measured at temperature $T = 50$ mK (black solid line), 4.8 K (red solid line), and 31 K (green dashed line), with an applied magnetic field of 11 T and bias current of 10 nA. The top axis shows also the filling factor ν . A series resistance of 2.53 k Ω is subtracted from all curves. In addition, the resistance of one superconducting leads, 4.6 k Ω , is subtracted from the data measured at 4.8 K and 31 K where the leads have switched to normal. The conductance of a different device with two normal contacts (NGN) is shown with the thin gray line, in order to indicate the expected positions of the Hall plateaus. (b) Two terminal differential resistance dV/dI of the superconducting wire as a function of the bias current at temperature $T = 50$ mK (black solid line), 5 K (red solid line), and 28 K (green dashed line). A series resistance of 5.06 k Ω from the filters is subtracted from each curve.

13 k Ω . A third plateau at filling factor $\nu = -6$ is also discernible at resistance $h/6e^2 \approx 4.3$ k Ω . The plateaus are more clearly shown in Fig. 7.6a where the conductance of the device at 11 T is plotted versus carrier density for three different temperatures. Again we see that the $\nu = \pm 2$ plateaus are well developed and are quantized at the right value, whereas the $\nu = -6$ plateau shows higher conductance than a NGN device or the expected value of $6e^2/h$. As the magnetic field is lowered, the width of the plateaus decreases and the resistance becomes lower than the quantization values (Fig. 7.5). Large amplitude fluctuations of the resistance are clearly shown on the plateaus. These fluctuations are reproducible and will be discussed further in section 7.5. In summary, we observe clear signatures of QHE characteristic for monolayer graphene in our device at various magnetic fields and temperatures.

At the base temperature of 50 mK, the critical field H_{c2} of the superconducting leads

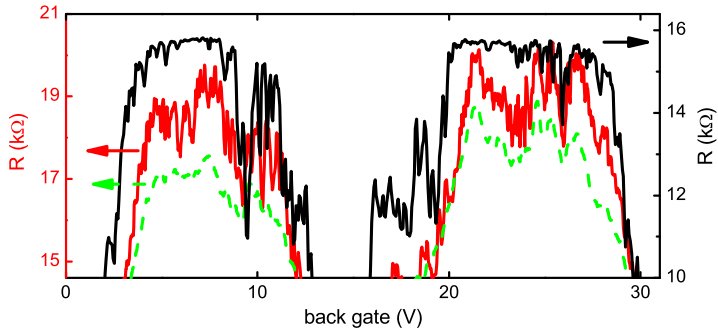


Figure 7.7: Three-terminal resistance of graphene as a function of the back gate voltage measured at temperature $T = 50$ mK (black solid line), 4.8 K (dark gray solid line), and 31 K (gray dashed line), with an applied magnetic field of 11 T and bias current of 10 nA. This is the same data as that shown in Fig. 7.6a, except that here we plot the resistance and no series resistance has been subtracted.

is higher than 11 T. This is shown in Fig. 7.6b where the two-terminal differential resistance of the superconducting leads is plotted versus the bias current at $B = 11$ T. We see that the critical current of the NbTiN electrodes is around $2 \mu\text{A}$ at 11 T and 50 mK. As the temperature of the cryostat is raised to 5 K and above, the NbTiN electrodes become normal as indicated by the constant dV/dI values versus the bias current (Fig. 7.6b, red solid and light green dashed lines). We obtain that the normal state resistance of our superconducting leads is 9.2 k Ω for two wires. At $B = 11$ T, the critical temperature of the NbTiN leads is in the range between 2 K and 4 K, which makes it a very suitable material for this experiment.

However, both below and above the critical temperature of the NbTiN leads, the $\nu = \pm 2$ or $\nu = -6$ plateaus at 11 T show the correct quantized conductance of $2e^2/h$ or $6e^2/h$, and show little dependence on the temperature³ (see Fig. 7.6a). Both observations suggest that the superconducting contacts act as normal reservoirs for the electrons at 11 T. This is possible since at high magnetic field, the NbTiN electrodes contain a high density of vortices. At $B = 11$ T, the average spacing between two neighbouring vortices is about 20 nm, which is close to the coherence length of the superconductor. The electrons (quasi-particles) can thus be trapped into the vortices. Alternatively, it is possible that at $B = 11$ T, the superconductor is in a gapless state [29–31]. At present we

³Using the three-terminal geometry as shown in Fig. 7.1, the resistance of one lead are included in the raw data. Therefore when the temperature is increased from below T_c of the NbTiN leads to above, the measured resistance increase by around 4.6 k Ω (Fig. 7.7) which is approximately equal to the normal state resistance of one NbTiN lead. This resistance is subtracted to generate the plot in Fig. 7.6a.

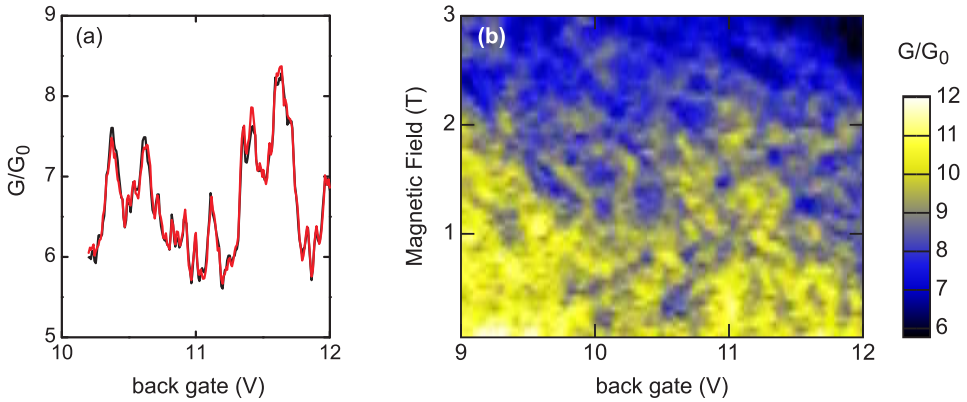


Figure 7.8: (a) Three-terminal conductance G of graphene as a function the back gate voltage measured at $T = 50$ mK and $B = 3$ T using a bias current of 10 nA. The black and gray (red) curves are the results of two identical measurements. (b) Three-terminal conductance G as a function of both the back gate voltage and the perpendicular magnetic field measured at $T = 50$ mK using a bias current of 100 nA. For both (a) and (b), a series resistance of 2.53 k Ω is subtracted from the raw data in order to obtain the conductance. $G_0 = e^2/h$.

find no evidence for Andreev reflections in the high magnetic field regime.

In addition to the qualitative similarities between the conductance curves at different temperatures as mentioned above, we also notice that the conductance at the plateaus increases to become slightly higher than the expected quantization values as the temperature increases. This is also clearly shown in Fig. 7.7 where the resistance of the $\nu = \pm 2$ plateaus is plotted for three different temperatures. This is likely to be because the temperature approaches the activation energy of the bulk insulating states in the quantum Hall regime.

7.5 Quantum Hall fluctuations

In this section we focus on the observed fluctuations in resistance at the quantum Hall plateaus. We argue that it is different from the universal conductance fluctuations (UCF) present in the low field regime, but is similar to the so-called *quantum Hall fluctuations*. Within the framework of Coulomb blockade, we discuss that electron-electron interactions play a role in this regime.

Universal conductance fluctuations have been observed routinely on graphene [17, 32], because the phase coherence length of graphene is typically a few micrometers long at low temperatures [18, 33, 34], which is larger than the typical length of our devices. In Fig. 7.8a, we show the reproducible conductance fluctuations as a function of the back gate voltage (density) measured at a low field. The conductance fluctuations as a function of both the density and an external magnetic field are represented by the

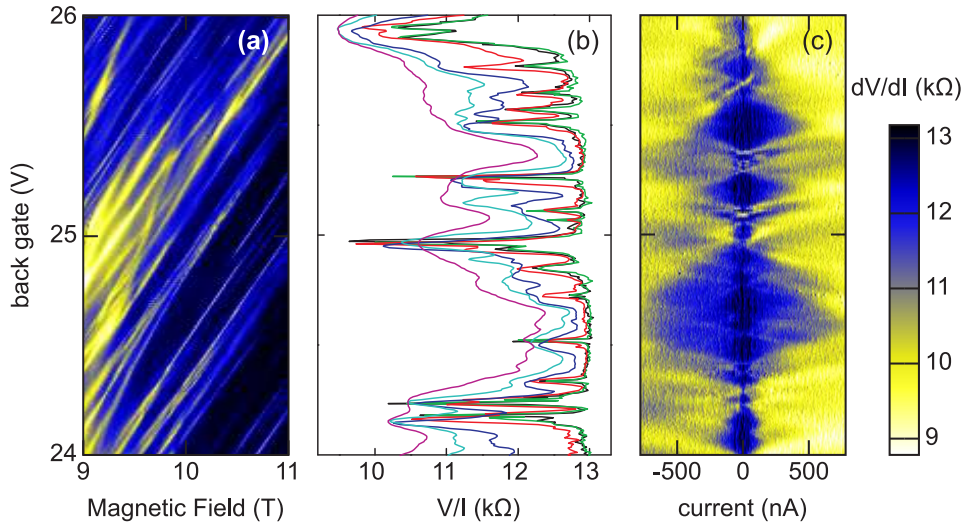


Figure 7.9: Quantum Hall fluctuations around the $\nu = 2$ plateau at $T = 50$ mK. (a) Three-terminal resistance as a function of both back gate voltage and magnetic field measured using a bias current of 10 nA. (b) The measured voltage V divided by the applied bias current I as a function of the back gate voltage at $B = 11$ T. A three-terminal geometry is used for this measurement. The curves from left to right are measured using bias current of 450 nA, 250 nA, 150 nA, 50 nA, 10 nA and 10 nA. (c) Differential resistance dV/dI (color scale) as a function of the bias current and back gate voltage at $B = 11$ T. A series resistance of 2.53 k Ω is subtracted from the raw data for all three panels.

color plot in Fig. 7.8b. A change in carrier density and thereby in the Fermi energy E_F , or a change in magnetic field modifies the interference pattern [35], and causes the observed reproducible fluctuations in the conductance. When phase coherence is maintained over the entire sample, the magnitude of the conductance fluctuations δG is predicted to be of the order e^2/h for a diffusive sample, regardless of the device dimensions or disorder strength [35]. This is clearly shown in Fig. 7.8a.

The behavior in the quantum Hall regime (high magnetic field) is however different from UCF. As already mentioned in the previous section, at $B = 11$ T, we observe strong fluctuations in resistance on the Hall plateaus which appear as resistance dips below the plateau value (see for instance Fig. 7.7). In Fig. 7.9a, the resistance on the $\nu = 2$ plateau is shown as a function of both the density n and the magnetic field B . In contrast to the case of UCF (Fig. 7.8b), here the dips evolve along roughly parallel diagonal lines on the n - B plane, and the slope $\delta n/\delta B$ is approximately proportional to the filling factor as $\delta n/\delta B \approx \nu e/h$. Similar behaviors are observed on the $\nu = -2$ and $\nu = -6$ plateaus. The rightmost line of Fig. 7.9b shows a line cut from Fig. 7.9a along the density direction. The standard deviation for the depth of the resistance dips is $\delta R \approx 1$ k Ω , or $\delta G = \delta R/R^2 \approx 0.1e^2/h$, much smaller than that of UCF.

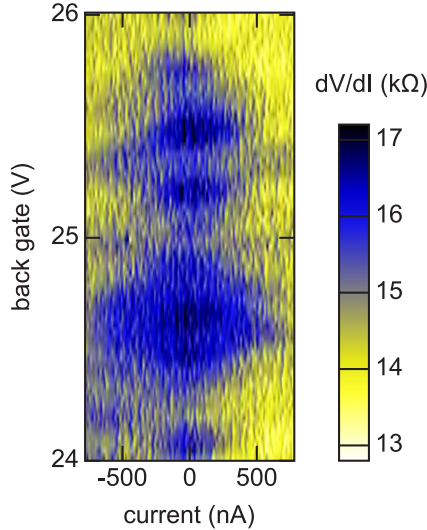


Figure 7.10: Differential resistance dV/dI as a function of the bias current and back gate voltage measured in the same regime as that of Fig. 7.9c ($B = 11$ T), but at temperature $T = 6.3$ K. A series resistance of 2.53 k Ω is subtracted from the raw data.

From Fig. 7.9b, we can already notice that away from the resistance dips, the resistance is not constant for different bias currents. Stated differently, the IV characteristics are nonlinear away from the resistance dips. This nonlinearity becomes clearer in Fig. 7.9c where the differential resistance dV/dI , represented by the color scale, is plotted as a function of both bias current and back gate voltage. The result resembles Coulomb blockade [36] with a charging energy of around 2 meV. Within each "Coulomb diamond", the resistance is equal to the expected plateau value of $h/2e^2 = 13$ k Ω . When the Coulomb blockade is lifted, resistance dips appear below the plateau value. Similar behavior is also observed on the $\nu = -2$ and $\nu = -6$ plateaus.

When the temperature is raised to above the critical temperature of the NbTiN leads (in the range of 2 K to 4 K at $B = 11$ T), a qualitatively similar behavior as that in Fig. 7.9 is still observed. For instance, Fig. 7.10 shows the measured "Coulomb diamonds" at $T = 6$ K. Compared to Fig. 7.9c, the Coulomb diamonds are much more blurred, but are still visible. The temperature independence suggests that the observed nonlinearity is not related to the superconductivity of the NbTiN leads.

The observed resistance fluctuation on the Hall plateaus can be attributed to quantum Hall fluctuations (QHF) [37–41] as illustrated in Fig. 7.11. Within a quantum Hall plateau, the Fermi energy lies between two Landau levels in the bulk where the states are localized due to disorder. Along the edges of the sample however, the current-carrying edge states extend throughout the entire system. When the dimensions of the

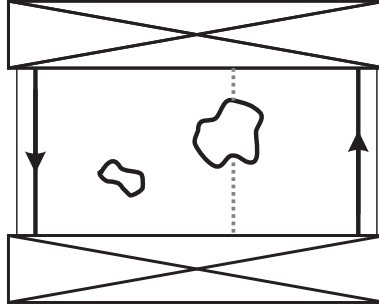


Figure 7.11: Schematic illustration of the resonant tunneling through the bulk insulating states in the quantum Hall regime. The arrows on the left and right edges of the sample represent the current-carrying edge states. The thick solid lines illustrate two possible isolated islands in the bulk, and the gray dotted lines indicate a possible tunneling path that connects the two reservoirs via one island.

samples are small, resonant tunneling can occur through the bulk insulating states of the quantum Hall regime, giving rise to fluctuations in resistance. Previously, the quantum Hall fluctuations are studied in devices consisting of long and narrow channels, where resonant tunneling is most likely to occur between edge channels from the two opposite edges and the resistance fluctuations are most apparent at the transition regions between two successive Hall plateaus [37, 38].

In our device however, the separation between the two edges is larger than the spacing between the two reservoirs. As a result, it is more likely for the electrons from one reservoir to tunnel through the bulk insulating states and reach the second reservoir. Such resonant tunneling events open up new conducting paths in addition to the edge states, resulting in the observed dips (rather than peaks) in resistance. This also explains the observed Coulomb blockade, which can be a result of the charging effect from the isolated islands in the bulk.

We next discuss the (a-)periodicity of the observed resistance dips. The spacing between two neighbouring dips shows large variations as the back gate voltage is changed. This is different from the charging effect of a single island [36] (see also section 2.4 of this thesis), where the oscillations are highly periodic. The aperiodicity of the quantum Hall fluctuations can be due to tunneling through multiple islands or through islands of different size, which are likely as the islands are induced by disorder in this case. Nevertheless, we can estimate the average size of such islands within the framework of Coulomb blockade. From Fig. 7.9b, the average spacing between two neighbouring resistance dips in the back gate voltage is $\Delta V_{BG} = 0.08 \pm 0.05$ V. The capacitance between the island and the back gate $C_{BG} = e/\Delta V_{BG}$ is therefore in the range of 1 to 5 aF. Using the expression for the capacitance of a disk in an infinite space $C = 4\epsilon_0(\epsilon_r + 1)D$ where $\epsilon_r = 3.9$ is the dielectric constant of SiO₂⁴ and D is the diameter of the island, we can

⁴This expression is a good approximation as the disk diameter is much smaller than the distance between the

roughly estimate that the average size of the islands is in the range of 60 nm to 15 nm. This is comparable to the estimate of 60 nm using a scanning probe technique [39].

7.6 Summary and outlook

In summary, we have fabricated two-terminal graphene devices using a high H_{c2} superconductor, NbTiN, as contacts. The transport properties of the devices are investigated both in the low field and high field regimes. At low magnetic fields, we observe Josephson supercurrent through our device, which demonstrates the high transparency of our contacts as well as the presence of Andreev reflections in this regime. In the high magnetic field regime, the device shows two-terminal quantum Hall effect which is independent on temperature for both below and above the critical temperature of the superconducting leads, indicating that the presence of the superconducting leads does not play an important role in this regime. In addition, we observe resistance dips and nonlinearity in IV characteristics on the Hall plateaus in the high field regime. The results are analyzed within the framework of quantum Hall fluctuations and Coulomb blockade, from which the localization area is estimated to be a few tens of nanometers for our device at a magnetic field of 11 T.

At present we do not observe signs of Andreev reflections in the high field regime. This is likely due to the high density of vortices that are present in the superconducting leads at high magnetic fields. In order to study the effects of Andreev reflections in the quantum Hall regime for the next step, we need to improve the mobility of the graphene in order to reduce the threshold field needed for observing quantum Hall effect. In addition, the resistance fluctuations observed in our devices with two-terminal geometry might obscure the expected resistance change due to Andreev reflections in the high magnetic field regime. Further analysis and experiments are underway to test different device layouts.

References

- [1] H. Takayanagi and T. Kawakami, *Superconducting Proximity Effect in the Native Inversion Layer on InAs*, Physical Review Letters **54**, 2449 (1985).
- [2] A. F. Morpurgo, S. Holl, B. J. van Wees, T. M. Klapwijk, and G. Borghs, *Phase Conjugated Andreev Backscattering in Two-Dimensional Ballistic Cavities*, Physical Review Letters **78**, 2636 (1997).

disk and the back gate (285 nm). On the other hand, the dielectric environment below the disk is different from that above, the effective dielectric constant is smaller than 3.9.

-
- [3] Y.-J. Doh, J. A. van Dam, A. L. Roest, E. P. A. M. Bakkers, L. P. Kouwenhoven, and S. De Franceschi, *Tunable Supercurrent Through Semiconductor Nanowires*, *Science* **309**, 272 (2005).
- [4] Y. Takagaki, *Transport properties of semiconductor-superconductor junctions in quantizing magnetic fields*, *Physical Review B* **57**, 4009 (1998).
- [5] Y. Asano, *Magnetoconductance oscillations in ballistic semiconductor-superconductor junctions*, *Physical Review B* **61**, 1732 (2000).
- [6] Y. Asano and T. Yuito, *Effects of disorder on conductance oscillations in semiconductor-superconductor junctions in a magnetic field*, *Physical Review B* **62**, 7477 (2000).
- [7] N. M. Chtchelkatchev and I. S. Burmistrov, *Conductance oscillations with magnetic field of a two-dimensional electron gas-superconductor junction*, *Physical Review B* **75**, 214510 (2007).
- [8] H. Takayanagi, *Semiconductor-coupled superconducting junctions using NbN electrodes with high H_{c2} and T_c* , *Physica B: Condensed Matter* **249-251**, 462 (1998), ISSN 09214526.
- [9] T. D. Moore and D. A. Williams, *Andreev reflection at high magnetic fields*, *Physical Review B* **59**, 7308 (1999).
- [10] H. Takayanagi, *Superconducting junctions using AlGaAs/GaAs heterostructures with high H_{c2} NbN electrodes*, *Physica E: Low-dimensional Systems and Nanostructures* **12**, 922 (2002), ISSN 13869477.
- [11] J. Eroms, D. Weiss, J. De Boeck, G. Borghs, and U. Zülicke, *Andreev Reflection at High Magnetic Fields: Evidence for Electron and Hole Transport in Edge States*, *Physical Review Letters* **95**, 107001 (2005).
- [12] I. E. Batov, T. Schäpers, N. M. Chtchelkatchev, H. Hardtdegen, and A. V. Ustinov, *Andreev reflection and strongly enhanced magnetoresistance oscillations in $Ga_xIn_{1-x}As/InP$ heterostructures with superconducting contacts*, *Physical Review B* **76**, 115313 (2007).
- [13] Y. Zhang, Y.-W. Tan, H. L. Stormer, and P. Kim, *Experimental observation of the quantum Hall effect and Berry's phase in graphene*, *Nature* **438**, 201 (2005), ISSN 0028-0836.
- [14] K. S. Novoselov, A. K. Geim, S. V. Morozov, D. Jiang, M. I. Katsnelson, I. V. Grigorieva, S. V. Dubonos, and A. A. Firsov, *Two-dimensional gas of massless Dirac fermions in graphene*, *Nature* **438**, 197 (2005), ISSN 0028-0836.

-
- [15] K. S. Novoselov, E. McCann, S. V. Morozov, V. I. Fal'ko, M. I. Katsnelson, U. Zeitler, D. Jiang, F. Schedin, and A. K. Geim, *Unconventional quantum Hall effect and Berry's phase of 2π in bilayer graphene*, Nature Physics **2**, 177 (2006), ISSN 1745-2473.
- [16] K. S. Novoselov, Z. Jiang, Y. Zhang, S. V. Morozov, H. L. Stormer, U. Zeitler, J. C. Maan, G. S. Boebinger, P. Kim, and A. K. Geim, *Room-Temperature Quantum Hall Effect in Graphene*, Science **315**, 1379 (2007).
- [17] H. B. Heersche, P. Jarillo-Herrero, J. B. Oostinga, L. M. K. Vandersypen, and A. F. Morpurgo, *Bipolar supercurrent in graphene*, Nature **446**, 56 (2007), ISSN 0028-0836.
- [18] F. Miao, S. Wijeratne, Y. Zhang, U. C. Coskun, W. Bao, and C. N. Lau, *Phase-Coherent Transport in Graphene Quantum Billiards*, Science **317**, 1530 (2007).
- [19] X. Du, I. Skachko, and E. Y. Andrei, *Josephson current and multiple Andreev reflections in graphene SNS junctions*, Physical Review B **77**, 184507 (2008).
- [20] C. O. Aristizabal, M. Ferrier, S. Guéron, and H. Bouchiat, *Tuning the proximity effect in a superconductor-graphene-superconductor junction*, Physical Review B **79**, 165436 (2009).
- [21] B. M. Kessler, C. O. Girit, A. Zettl, and V. Bouchiat, *Tunable Superconducting Phase Transition in Metal-Decorated Graphene Sheets* (2009), arXiv:0907.3661.
- [22] M. Lafkioti, B. Krauss, T. Lohmann, U. Zschieschang, H. Klauk, K. von Klitzing, and J. H. Smet, *Graphene on a Hydrophobic Substrate: Doping Reduction and Hysteresis Suppression under Ambient Conditions*, Nano Letters **10**, 1149 (2010).
- [23] N. N. Iosad, N. M. van der Pers, S. Grachev, V. V. Roddatis, B. D. Jackson, S. N. Polyakov, P. N. Dmitriev, and T. M. Klapwijk, *Texture formation in sputter-deposited (Nb_{0.7}Ti_{0.3})N thin films*, Journal of Applied Physics **92**, 4999 (2002).
- [24] X. L. Liu, D. Hug, and L. M. K. Vandersypen, *Gate-defined graphene double quantum dot and excited state spectroscopy*, Nano Letters **10**, 1623 (2010).
- [25] M. Tinkham, *Introduction to superconductivity* (Dover Publications, Mineola, USA, 1996).
- [26] F. Rohlfing, G. Tkachov, F. Otto, K. Richter, D. Weiss, G. Borghs, and C. Strunk, *Doppler shift in Andreev reflection from a moving superconducting condensate in Nb/InAs Josephson junctions*, Physical Review B **80**, 220507 (2009).

- [27] P. Dubos, H. Courtois, B. Pannetier, F. K. Wilhelm, A. D. Zaikin, and G. Schön, *Josephson critical current in a long mesoscopic S-N-S junction*, Physical Review B **63**, 064502 (2001).
- [28] After sweeping magnetic field, we always observe a decrease in the switching current up to a factor 2 lower. The switching current can increase again after we deliberately perturb the device. This indicates the presence and partial removal of the trapped flux.
- [29] K. Maki, *Gapless superconductivity* (1969), edited by R. D. Parks.
- [30] A. Anthore, H. Pothier, and D. Esteve, *Density of States in a Superconductor Carrying a Supercurrent*, Physical Review Letters **90**, 127001+ (2003).
- [31] J. E. Mooij, private communication.
- [32] M. B. Lundeberg and J. A. Folk, *Spin-resolved quantum interference in graphene*, Nature Physics **5**, 894 (2009), ISSN 1745-2473.
- [33] D. Graf, F. Molitor, T. Ihn, and K. Ensslin, *Phase-coherent transport measured in a side-gated mesoscopic graphite wire*, Physical Review B **75**, 245429 (2007).
- [34] S. Russo, J. B. Oostinga, D. Wehenkel, H. B. Heersche, S. S. Sobhani, L. M. K. Vandersypen, and A. F. Morpurgo, *Observation of Aharonov-Bohm conductance oscillations in a graphene ring*, Physical Review B **77**, 085413 (2008).
- [35] C. W. J. Beenakker and H. van Houten, *Quantum Transport in Semiconductor Nanostructures* (Elsevier, 1991), vol. 44, pp. 1–228, ISBN 9780126077445, URL [http://dx.doi.org/10.1016/S0081-1947\(08\)60091-0](http://dx.doi.org/10.1016/S0081-1947(08)60091-0).
- [36] L. P. Kouwenhoven, C. M. Marcus, P. L. McEuen, S. Tarucha, R. M. Westervelt, and N. S. Wingreen, *Electron transport in quantum dots* (Kluwer, Alphen aan den Rijn, the Netherlands, 1997).
- [37] P. C. Main, A. K. Geim, H. A. Carmona, C. V. Brown, T. J. Foster, R. Taboryski, and P. E. Lindelof, *Resistance fluctuations in the quantum Hall regime*, Physical Review B **50**, 4450 (1994).
- [38] D. H. Cobden, C. H. W. Barnes, and C. J. B. Ford, *Fluctuations and Evidence for Charging in the Quantum Hall Effect*, Physical Review Letters **82**, 4695 (1999).
- [39] J. Martin, N. Akerman, G. Ulbricht, T. Lohmann, K. von Klitzing, J. H. Smet, and A. Yacoby, *The nature of localization in graphene under quantum Hall conditions*, Nature Physics **5**, 669 (2009), ISSN 1745-2473.

-
- [40] S. Branchaud, A. Kam, P. Zawadzki, F. M. Peeters, and A. S. Sachrajda, *Transport detection of quantum Hall fluctuations in graphene*, Physical Review B **81**, 121406 (2010).
- [41] J. Velasco, G. Liu, L. Jing, P. Kratz, H. Zhang, W. Bao, M. Bockrath, and C. N. Lau, *Probing charging and localization in the quantum Hall regime by graphene $p-n-p$ junctions*, Physical Review B **81**, 121407 (2010).

Chapter 8

Conclusions and outlook

In this chapter an overview is given on the research works discussed in this thesis, along with the related works elsewhere. We analyze the main results achieved so far as well as the major limitations. Attempts are made to suggest future directions based on such analysis.

8.1 Current status

8.1.1 Band gap engineering and quantum dots on graphene

For the first part of this thesis, considerable efforts are made to build quantum dots on graphene. As graphene is a zero-gap semiconductor, it is difficult to confine electrons electrostatically. The road map we planned to follow then is to (1) create a band gap in graphene; (2) confine electrons in a graphene quantum dot using electrostatic gating effects; (3) search and identify a single spin in a graphene dot. And perhaps as a long term goal, we expect to realize coherent control of the single spin in a graphene dot. So far we have realized the first two steps.

Two directions are taken in order to achieve the first step of creating a band gap in graphene. One way is to induce a band gap on bilayer graphene using an electric field perpendicular to the plane. The other direction is to etch graphene into a nanoribbon and thereby create a confinement gap. Experimentally, we observe transport gap in graphene using both methods. However, the nature of the transport gap appears to be more complex than a simple and clean band gap in both cases.

Recently, significant progresses have been made in understanding the experimentally observed transport gap both for the dual-gated bilayer graphene [1], and for graphene nanoribbons [2]. By studying the temperature dependence, it is identified that disorder plays a dominating role in the electronic properties of both systems. The charge

transport is described by variable range hopping in the low temperature range and by a thermally activated behavior in the high temperature range.

For the second step on the road map, we have fabricated local top gates on the gapped graphene nanoribbons and subsequently confined electrons in a single quantum dot (chapter 5) and a double quantum dot (chapter 6) with these local gates. For both cases, the device properties such as the tunability and the degree of control suffer from strong disorder.

In attempt of the third step, we have observed transport through excited states both in our single quantum dot and double quantum dot devices. However, we are not yet able to observe the spin states. Recently, J. Güttinger *et al.* have identified spin filling in an etched quantum dot device [3].

8.1.2 Andreev reflections and quantum Hall effect on graphene

In addition to the device applications of graphene, we are also interested in its fundamental aspects. The absence of a band gap becomes an advantage from the perspective of making a transparent contact to a superconductor. Meanwhile, the unusual quantum Hall effect is also a very tempting subject. In Chapter 7 of this thesis, we try to combine these two properties using a graphene Josephson junction device with a high H_{c2} superconductor as contacts. The goal is to study the interplay between the quantum Hall edge states of graphene and Andreev reflections at the graphene-superconductor interface.

Currently, we have observed Josephson current and thereby Andreev reflections at low magnetic field, as well as quantum Hall effect at high field. However, we are not yet able to identify Andreev reflections in the quantum Hall regime. The probability for Andreev reflection is probably reduced in the high field regime by the high density of vortices in the superconductor. For the next step, one needs to improve the mobility of our graphene device in order to reduce the threshold magnetic field needed for observing quantum Hall effect in graphene.

8.2 Future experiments

8.2.1 Improving the mobility

In all four experiments that we worked on so far, disorder is a major limiting factor for our graphene devices. Thus one urgent issue is to improve the mobility of graphene and reduce disorder. Many research groups are working on identifying the origin of the disorder [4, 5] as well as suppressing it.

One way to reduce the disorder can be learned from earlier works on carbon nanotubes, where suspended nanotubes are found to be ultraclean [6, 7]. Indeed ultrahigh mobility is found in suspended graphene [8–10] along with new physics in such clean

systems [11, 12]. These works also indicate that the underlying SiO₂ substrate is one of the major sources for disorder.

However, not all suspended graphene sheets shown high mobility. It is found that suspended graphene membranes tends to wrinkle after being subjected to temperature changes. Such wrinkled devices show rather low mobility [13]. In addition, suspended devices need to be handled with great care, and are incompatible with some lithography steps. Therefore, other research is carried out meanwhile to study the quality of graphene on different substrates [14–16] than the commonly used amorphous SiO₂. Recently, it is found that graphene deposited on boron nitride substrate shows exceptionally high quality [17]. This result marks an important progress in the quest for improving the mobility of graphene.

Another source of disorder can be induced during the lithography processing, which can play an as important role as the underlying substrate [18]. A current annealing step is found to be able to clean away some of the resist residue and thereby improve the mobility of graphene [8, 19]. Furthermore, one can also again follow the footsteps of carbon nanotubes [7, 20] and devise fabrication procedures that are fully lithography-free after the deposition of graphene. There are still plenty of room and opportunities along this line.

8.2.2 Quantum dots in bilayer graphene

Following the line of research described in the first part of this thesis on *Band gap engineering and quantum dots on graphene*, one arrives naturally at the conclusion that we need to proceed to build quantum dot devices on gapped bilayer graphene using only electrostatic gates.

A bilayer graphene dot has also two obvious advantages over quantum dots on graphene nanoribbons. First of all, the rough edges of most experimental graphene nanoribbons are additional sources for disorder in the system and are highly undesirable. A bilayer graphene dot formed by electrostatic gates, in contrast, has boundaries defined by smooth electrostatic potential and thereby surpasses this problem. Secondly, quantum dots based on graphene nanoribbons do not take advantage of the two-dimensionality of graphene, whereas in a bilayer graphene dot, one can conveniently build complex device structures similar to those on GaAs 2DEG systems [21].

8.2.3 Cooper pair detection using spin valves

Cooper pairs are natural sources for entangled spins. When a superconductor is in contact with a normal conductor, Cooper pairs can "leak" into the normal conductor, a phenomenon known as the proximity effect. Proximity effect has been observed in Josephson junctions based on graphene [22, 23].

The spin polarization can be detected using a spin valve device which has also been demonstrated on graphene [24]. Combining the two type of devices, one can build

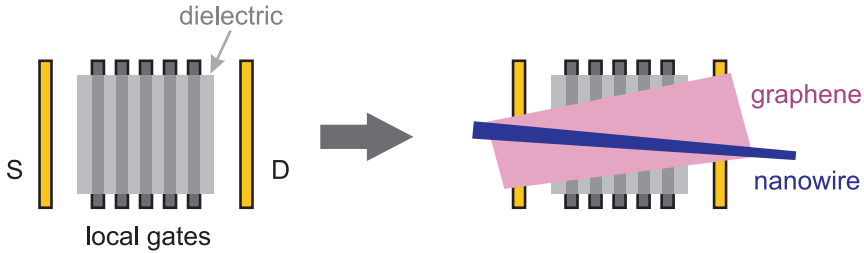


Figure 8.1: Illustration of the fabrication procedures for a graphene nanoribbon using a nanowire as an etching mask. Five local gates are shown as an example. The source and drain contacts are labeled as **S** and **D**, respectively.

a Cooper pair beam splitter on graphene, using one or two spin valves as detectors for verifying the spin orientation and correlations of the Cooper pairs injected into graphene from the superconductor.

8.2.4 Hybrid systems of graphene nanoribbon and nanowires

A hybrid system that combines the advantages of its components and avoids or compensates for each other's weakness is highly desirable. A clean graphene nanoribbon and a nanowire form one such advantageous hybrid system. Below we discuss in detail the fabrication and the envisioned experiments based on such a system.

First we discuss a possible fabrication procedure for making a clean quantum dot device on a graphene nanoribbon using a nanowire as an etching mask. The goal for the design of this process is that there should be no lithography steps after the deposition of graphene. As discussed in section 8.2.1, a *lithography-free* fabrication recipe can lead to highly clean devices. A graphene quantum dot device needs three ingredients, the local gates, the source and drain contacts, and a graphene nanoribbon. In order to achieve this goal, the plan is to deposit graphene only after the entire device architecture (local gates, contacts) has been built on the substrates. Below we describe the fabrication process in detail.

We first pattern several narrow metallic electrodes on an empty substrate, using a similar method as that described in ref. [25], followed by selectively covering the middle section of the electrodes with a dielectric layer, e.g. silicon oxide, silicon nitride or boron nitride. The two electrodes on the sides are left uncovered, as illustrated in the left panel of Fig. 8.1. Graphene flakes are then deposited on the gates and contacts. In step four, we deposit a thin nanowire on graphene, roughly perpendicular to the pre-patterned electrodes (see Fig. 8.1, right panel). A graphene nanoribbon device is formed below the nanowire after the substrate is subsequently exposed to a plasma. For the last step, we now need to do one lithography step on graphene, in order to contact the narrow gates and contacts to larger contact pads. However, we believe that this step will not have a

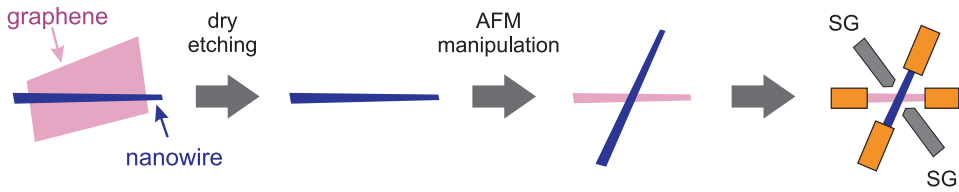


Figure 8.2: Illustration of the fabrication procedures for a two-quantum-dot system, with one dot in the graphene nanoribbon and another dot in the nanowire. The side gates are labeled as **SG** in the graph.

large influence on the properties of graphene nanoribbon as it is still protected by the nanowire etching mask. With the six steps described above, one obtains a quantum dot device on a clean graphene nanoribbon. We notice that the nanowire can still remain on the nanoribbon. However, if it is desirable, one can also remove the nanowire using AFM [26].

With small variations, we can devise even more interesting devices. In the following, we discuss the option of building a two-quantum-dot system with one dot in the graphene nanoribbon and another dot in the nanowire. For this purpose, we relax the requirement on being lithography-free after the graphene deposition. We first deposit graphene flakes on an empty substrate as usual, followed by dropping a nanowire on a flake. Similar to the previous case, we subsequently expose the substrate to a plasma, and obtain a graphene nanoribbon which is covered by a nanowire. Using an AFM tip [26], we can then rotate the nanowire until it is at an angle with the nanoribbon, as illustrated in Fig. 8.2. After the rotation, electric contacts are made to both the nanowire and the nanoribbon in the last step.

At least two interesting experiments can be envisioned in this hybrid system. First, one can use a highly conductive nanowire for the etching mask. With the final device, this nanowire can act as a narrow top gate for the nanoribbon to form a graphene dot on the nanoribbon [27]. Conversely, if a nanowire dot is of interest, one can also use the graphene nanoribbon as a narrow bottom gate for the nanowire dot. In a second experiment, one can form two dots, one on the nanoribbon and another on the nanowire, by placing all four contacts close to the crossing. In this case, metal side gates close to the dots can be added in the last step in order to gain extra tunability. In this two-dot system, one can use one dot as a charge sensor for the other dot [28, 29].

One severe disadvantage of the methods described above, however, is that they rely largely on coincidence of small chance events, and are therefore likely to be of very low yield. For instance, a randomly deposited graphene flake needs to lie exactly on the pre-patterned electrodes, and another randomly deposited nanowire needs to lie exactly on the first graphene flake.

This disadvantage can be overcome if one uses a graphene wafer which is now possible to grow in a lab [30], or if one uses some of the recently developed transfer tech-

niques [17, 31].

References

- [1] K. Zou and J. Zhu, *Transport in gapped bilayer graphene: the role of potential fluctuations* (2010), [arXiv:1008.0783](#).
- [2] M. Y. Han, J. C. Brant, and P. Kim, *Electron Transport in Disordered Graphene Nanoribbons*, *Physical Review Letters* **104**, 056801 (2010).
- [3] J. Guettinger, T. Frey, C. Stampfer, T. Ihn, and K. Ensslin, *Spin States in Graphene Quantum Dots* (2010), [arXiv:1002.3771](#).
- [4] E. H. Hwang, S. Adam, and S. D. Sarma, *Carrier Transport in Two-Dimensional Graphene Layers*, *Physical Review Letters* **98**, 186806 (2007).
- [5] J. H. Chen, C. Jang, S. Adam, M. S. Fuhrer, E. D. Williams, and M. Ishigami, *Charged-impurity scattering in graphene*, *Nature Physics* **4**, 377 (2008), ISSN 1745-2473.
- [6] P. Jarillo-Herrero, S. Sapmaz, C. Dekker, L. P. Kouwenhoven, and H. S. J. van der Zant, *Electron-hole symmetry in a semiconducting carbon nanotube quantum dot*, *Nature* **429**, 389 (2004), ISSN 0028-0836.
- [7] J. Cao, Q. Wang, and H. Dai, *Electron transport in very clean, as-grown suspended carbon nanotubes*, *Nature Materials* **4**, 745 (2005), ISSN 1476-1122.
- [8] K. Bolotin, K. Sikes, Z. Jiang, M. Klima, G. Fudenberg, J. Hone, P. Kim, and H. Stormer, *Ultra-high electron mobility in suspended graphene*, *Solid State Communications* **146**, 351 (2008), ISSN 00381098.
- [9] K. I. Bolotin, K. J. Sikes, J. Hone, H. L. Stormer, and P. Kim, *Temperature-Dependent Transport in Suspended Graphene*, *Physical Review Letters* **101**, 096802 (2008), ISSN 0031-9007.
- [10] X. Du, I. Skachko, A. Barker, and E. Y. Andrei, *Approaching ballistic transport in suspended graphene*, *Nature Nanotechnology* **3**, 491 (2008), ISSN 1748-3387.
- [11] X. Du, I. Skachko, F. Duerr, A. Luican, and E. Y. Andrei, *Fractional quantum Hall effect and insulating phase of Dirac electrons in graphene*, *Nature* **462**, 192 (2009), ISSN 0028-0836, [arXiv:0910.2532](#).
- [12] K. I. Bolotin, F. Ghahari, M. D. Shulman, H. L. Stormer, and P. Kim, *Observation of the fractional quantum Hall effect in graphene*, *Nature* **462**, 196 (2009), ISSN 0028-0836.

-
- [13] W. Bao, F. Miao, Z. Chen, H. Zhang, W. Jang, C. Dames, and C. N. Lau, *Controlled ripple texturing of suspended graphene and ultrathin graphite membranes*, Nature Nanotechnology **4**, 562 (2009), ISSN 1748-3387, [arXiv:0903.0414](#).
- [14] U. Stöberl, U. Wurstbauer, W. Wegscheider, D. Weiss, and J. Eroms, *Morphology and flexibility of graphene and few-layer graphene on various substrates*, Applied Physics Letters **93**, 051906 (2008).
- [15] L. A. Ponomarenko, R. Yang, T. M. Mohiuddin, M. I. Katsnelson, K. S. Novoselov, S. V. Morozov, A. A. Zhukov, F. Schedin, E. W. Hill, and A. K. Geim, *Effect of a High- k Environment on Charge Carrier Mobility in Graphene*, Physical Review Letters **102**, 206603 (2009).
- [16] M. Lafkioti, B. Krauss, T. Lohmann, U. Zschieschang, H. Klauk, K. von Klitzing, and J. H. Smet, *Graphene on a Hydrophobic Substrate: Doping Reduction and Hysteresis Suppression under Ambient Conditions*, Nano Letters **10**, 1149 (2010).
- [17] C. R. Dean, A. F. Young, I. Meric, C. Lee, L. Wang, S. Sorgenfrei, K. Watanabe, T. Taniguchi, P. Kim, K. L. Shepard, et al., *Boron nitride substrates for high-quality graphene electronics* (2010), [arXiv:1005.4917](#).
- [18] G. Goetz, Ph.D. thesis, Technische Universiteit Delft (2010).
- [19] J. Moser, A. Barreiro, and A. Bachtold, *Current-induced cleaning of graphene*, Applied Physics Letters **91**, 163513 (2007).
- [20] G. A. Steele, G. Gotz, and L. P. Kouwenhoven, *Tunable few-electron double quantum dots and Klein tunnelling in ultraclean carbon nanotubes*, Nature Nanotechnology **4**, 363 (2009), ISSN 1748-3387, [arXiv:0907.2321](#).
- [21] R. Hanson, L. P. Kouwenhoven, J. R. Petta, S. Tarucha, and L. M. K. Vandersypen, *Spins in few-electron quantum dots*, Reviews of Modern Physics **79**, 1217 (2007).
- [22] H. B. Heersche, P. Jarillo-Herrero, J. B. Oostinga, L. M. K. Vandersypen, and A. F. Morpurgo, *Bipolar supercurrent in graphene*, Nature **446**, 56 (2007), ISSN 0028-0836.
- [23] X. Du, I. Skachko, and E. Y. Andrei, *Josephson current and multiple Andreev reflections in graphene SNS junctions*, Physical Review B **77**, 184507 (2008).
- [24] N. Tombros, C. Jozsa, M. Popinciuc, H. T. Jonkman, and B. J. van Wees, *Electronic spin transport and spin precession in single graphene layers at room temperature*, Nature **448**, 571 (2007), ISSN 0028-0836.

-
- [25] S. N. Perge, S. M. Frolov, J. W. W. van Tilburg, J. Danon, Yu, R. Algra, E. P. A. M. Bakkers, and L. P. Kouwenhoven, *Disentangling the effects of spin-orbit and hyperfine interactions on spin blockade*, Physical Review B **81**, 201305 (2010).
- [26] B. Gao, Y. F. Chen, M. S. Fuhrer, D. C. Glatli, and A. Bachtold, *Four-Point Resistance of Individual Single-Wall Carbon Nanotubes*, Physical Review Letters **95**, 196802 (2005).
- [27] X. Liu, J. B. Oostinga, A. F. Morpurgo, and L. M. K. Vandersypen, *Electrostatic confinement of electrons in graphene nanoribbons*, Physical Review B **80**, 121407 (2009), arXiv:0812.4038.
- [28] I. Shorubalko, R. Leturcq, A. Pfund, D. Tyndall, R. Krischek, S. Schon, and K. Ensslin, *Self-Aligned Charge Read-Out for InAs Nanowire Quantum Dots*, Nano Letters **8**, 382 (2008).
- [29] J. Güttinger, C. Stampfer, S. Hellmüller, F. Molitor, T. Ihn, and K. Ensslin, *Charge detection in graphene quantum dots*, Applied Physics Letters **93**, 212102 (2008).
- [30] A. Reina, X. Jia, J. Ho, D. Nezich, H. Son, V. Bulovic, M. S. Dresselhaus, and J. Kong, *Large Area, Few-Layer Graphene Films on Arbitrary Substrates by Chemical Vapor Deposition*, Nano Letters **9**, 30 (2009).
- [31] G. F. Schneider, V. E. Calado, H. Zandbergen, L. M. K. Vandersypen, and C. Dekker, *Wedging Transfer of Nanostructures*, Nano Letters **10**, 1912 (2010).

Appendix A

Useful numbers and relations in graphene

- $\epsilon_0 = 1/\mu_0 c^2 = 8.85e-12$ F/m ($C^2/J\cdot m$) (vacuum permittivity)
- $a = 2.46$ Å (lattice constant of graphene)
- $a_0 = 1.42$ Å (bond length of graphene)
- $c_0 = 3.4$ Å (inter layer distance for graphite)
- $t = 3.1$ eV (nearest neighbour hopping integral)
- $t' = -0.1t$ (next nearest neighbour hopping integral)
- $v_F = \sqrt{3}ta/2\hbar = 1 \times 10^6$ m/s (Fermi velocity)
- $\hbar v_F = 0.66$ eV·nm
- coordinates of K point: $(\pm 4\pi/3a, 0)$ and $(\pm 2\pi/3a, \pm 2\pi/\sqrt{3}a)$
- density of states $DOS(E) = fE/2\pi(\hbar v_F)^2$
 $k_F = \sqrt{\pi n}$ and $E_F = \hbar v_F \sqrt{\pi n}$
- conversion from gate voltage to Fermi energy
 $V_{BG} = 1V \Rightarrow n = 7.2 \times 10^{10}$ cm⁻² (300 nm SiO₂)
 $\Rightarrow E_F/\text{meV} = 31 \sqrt{V_{BG}/V}$

- mobility

$$\begin{aligned}\mu &= \sigma / ne \\ &= (1/C_g) d\sigma / dV_g \\ &= \frac{1}{1.152e-4} \frac{d\sigma(S)}{dV_g(V)} m^2/Vs\end{aligned}$$

- cyclotron radius:

$$\begin{aligned}2R_c &= (\hbar/eB)\sqrt{\pi n} \\ &= 2E_F/e v_F B \\ &= 62 \text{ nm} \frac{\sqrt{V_{BG}/V}}{B/T}\end{aligned}$$

example: $B = 6 \text{ T}$ and $V_{BG} = 16 \text{ V}$, $2R_c = 41 \text{ nm}$

- mean free path (MFP)

$$\begin{aligned}l_{MFP} &= \mu \frac{\hbar}{e} \sqrt{\pi n} \\ &= \sigma \frac{\hbar}{2e^2} \frac{1}{\sqrt{\pi n}}\end{aligned}$$

- magnetic length $l_B = \sqrt{\frac{\hbar}{eB}} = 25 \text{ nm}/\sqrt{B}$
- Landau level for monolayer graphene $(\hbar v_F/l_B) \cdot \sqrt{2|n|} = 26 \text{ meV} \cdot \sqrt{2|n|B}$

Appendix B

Estimate of level spacing in graphene dots

We approximate the average level spacing in a quantum dot as $\delta E = \delta E_{1D}/4N$, where δE_{1D} is the dot level spacing per 1D subband, N is the total number of occupied 1D subbands, and the factor 4 in the denominator accounts for the valley and spin degeneracy. Fig. B.1 illustrates this idea. A rough estimate for δE_{1D} is $\pi\hbar v_F/l$, with l the top gate width as defined in the main text. A very rough estimate of N is E_F divided by the subband spacing, where an upper bound on the subband spacing is roughly half the band gap $E_g \approx 1eV \times nm/w$ [1].

In equations:

1D subband spacing $\Delta_{1D} = E_g/2$
band gap

$$E_g = 2\pi\hbar v_F/w \quad (\text{B.1})$$

$$= 4eV \cdot nm/w \quad (\text{B.2})$$

or $E_g = 0.2 - 0.8eV \cdot nm/w$ or $E_g = 1eV \cdot nm/w$ [1]
number of 1D channels in a 2D system $N_{1D} = E_F/\Delta_{1D}$
level spacing for 1D $\delta_{1D} = \pi\hbar v_F/l = 2eV \cdot nm/l$
thus, level spacing in a 2D system

$$\delta E = \frac{\delta E_{1D}}{fN_{1D}} \quad (\text{B.3})$$

$$= \frac{\pi}{2} \frac{2\pi(\hbar v_F)^2}{fE_F} \frac{1}{lw} \quad (\text{B.4})$$

or

$$\delta E = \alpha \frac{\pi}{2} \frac{1}{DOS(E_F)} \frac{1}{lw}$$

where the density of state $DOS(E) = fE/2\pi(\hbar v_F)^2$, and α is a parameter that can be used to adjust the theory to fit experiment :) **importantly, level spacing is inversely proportional to density of state at E_F .**

or $\delta E = \frac{2 \times (0.2 - 0.8) eV^2 \cdot nm^2}{2wl f E_F}$ (using Geim's empirical formula, so here $\alpha = 0.05 - 0.2$)

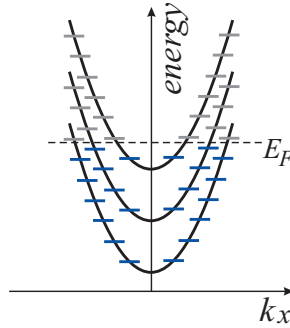


Figure B.1: illustration of the 1D sub-bands in a quantum dot. The blue and gray bars on the sub-bands represent the discrete occupied and unoccupied dot states, respectively. The x axis is along the length of the ribbon.

example:

$$\delta E(E_F) = 168 (8 - 34) \mu eV \cdot eV / E_F$$

References

- [1] A. K. Geim and K. S. Novoselov, *The rise of graphene*, Nature Materials **6**, 183 (2007), ISSN 1476-1122.

Appendix C

A cleaning recipe for Si/SiO₂ wafers

Step 1: Piranha / SPM (Removing organic contaminants)

- 80 ml 40% H₂SO₄
- 20 ml 30% H₂O₂
- Au-bain-marie at 90°C for 15 minutes

Step 2: Rinsing in DI water

Step 3: SC-1 / APM (Removes particular contaminants. Desorbs trace metals, like Au, Ag, Cu, Ni, etc.)

- 15 ml 29% NH₄OH
- 15 ml 30% H₂O₂
- 70 ml H₂O
- Au-bain-marie at 70°C for 10 minutes

Step 4: Rinsing in DI water

Step 5: SC-2 (Dissolves alkali ions and hydroxides of Al³⁺, Fe³⁺, Mg³⁺. Desorbs by complexing residual metals)

- 15 ml 30% HCl
- 15 ml 30% H₂O₂
- 70 ml H₂O
- Au-bain-marie at 70°C for 10 minutes

Step 6: Rinsing in DI water

Note: Mix solutions just prior to sample cleaning

Summary

Graphene is an exceptionally thin gapless semiconductor that consists of only one atomic layer of carbon atoms. The electrons in graphene live in a strictly two-dimensional (2D) world. In addition to this remarkable 2Dness, it is also peculiar that the behavior of the electrons in graphene is governed by the Dirac equation rather than the well known Schrödinger's equation, leading to the discovery of several new physics phenomena. Such unusual properties of graphene have stirred up great excitements since it was first isolated in the lab about five years ago.

In this thesis, we investigate the low temperature transport properties of the electrons and holes in several graphene based nano-devices. Overall, two topics are explored in this thesis. First we engineer an energy gap in graphene, which is naturally a zero-gap semiconductor, and further form quantum dot devices on the gapped graphene. The low temperature electronic transport properties of the confined electrons are then studied experimentally in such graphene dots. In a second project, we fabricated Josephson junction devices on graphene using a high H_{c2} superconductor as leads. Here the goal is to research on the interactions between the electrons from graphene and the Cooper pairs from the superconductor.

Two approaches are employed in order to create an energy gap in graphene. First, a band gap is predicted for a bilayer graphene which is subjected to an electric field which is perpendicular to the plane. A perpendicular electric field renders asymmetry between the top and the bottom layer of a bilayer graphene, which is equivalent to a difference in the on-site potential for the two pairs of the atoms within one unit cell. A spectral gap is induced as a result. Experimentally we created the asymmetry between the top and bottom layers using a dual-gated transistor geometry. At a non-zero electric field, the resistance increases by 2 to 3 orders of magnitude as the temperature is lowered, indicating the presence of an insulating state. This is in stark contrast to the case of monolayer graphene, where the resistance is much lower and is temperature independent. Further studies however suggest that the nature of the observed insulating state deviates from the expectation for a pure spectral gap. Rather it is found that disorder plays an important role in understanding the observed insulating states.

In a second approach, we investigate on the energy gap in a narrow graphene nanoribbon etched into a 2D graphene sheet. A graphene nanoribbon is a quasi-1D system where the confinement can generate a spectral gap. Experimentally, a transport gap is observed in graphene nanoribbons where the conductance is suppressed by 3 to 4 orders of magnitude comparing to that outside of the gap. The origin for the occurrence of such transport gap in a graphene nanoribbon is current of intense interests within the field.

Even though the nature for the observed transport gap in a graphene nanoribbon system is still elusive, we can nevertheless use its properties to induce confinement for the electrons. A single quantum dot device was first realized in a graphene nanoribbon device sandwiched between a narrow top gate and a back gate. Two different regimes, bipolar and unipolar were explored. In the bipolar regime, we demonstrated electrostatic confinement of charge carriers by $p-n$ junctions. In the unipolar regime, electrons are still confined, now as a result of strong disorder.

Following the work on top-gated single quantum dots, we next form a double quantum dot in a graphene nanoribbon device using three top gates. These gates independently change the number of electrons on each dot and tune the inter-dot coupling. In the weakly coupled double dot regime, transport through excited states is observed for the first time in a graphene double quantum dot system.

In addition to our interests on confined electrons, we also carried out research on studying fundamental aspects of condensed matter physics. One curious subject is to study the hybrid system of a superconductor and a semiconductor in the quantum Hall regime. It is well known that the electric transport at a superconductor-normal-conductor (SN) interface is described by Andreev reflections. In the quantum Hall regime, an electron wave that travels in skipping orbits is expected to experience multiple Andreev reflections along the SN interface. At the exit of the SN interface, the state is of both electron and hole characters. Such microscopic processes modify the magnetoresistance of the sample. Chapter 7 of this thesis describes an experiments where we wish to study this effect at a graphene-superconductor interface, using a Josephson junction device with a high H_{c2} superconductor as contacts. Currently, we have observed Josephson current and thereby Andreev reflections at low magnetic field, as well as quantum Hall effect at high field. However, we are not yet able to identify Andreev reflections in the quantum Hall regime. The probability for Andreev reflection is probably reduced in the high field regime by the high density of vortices in the superconductor. Further tests and analysis are underway in order to surpass this problem.

Samenvatting

Grafeen is een uitzonderlijk dunne halfgeleider, die bestaat uit slechts één atomaire laag koolstofatomen. De elektronen in grafeen leven in een strikt twee-dimensionale (2D) wereld. Naast deze opmerkelijke 2D-heid, is het ook bijzonder dat het gedrag van de elektronen in grafeen wordt bepaald door de Dirac-vergelijking, en niet de bekende Schrödinger-vergelijking, wat tot de ontdekking van verschillende nieuwe fysische fenomenen resulteerde. Deze ongebruikelijke eigenschappen van grafeen hebben voor veel opwinding gezorgd sinds de eerste keer dat grafeen succesvol was geïsoleerd in het laboratorium.

In dit proefschrift onderzoeken we de transport eigenschappen van de elektronen en gaten in verschillende grafeen gebaseerde nano-structuren bij lage-temperatuur. Twee onderwerpen worden onderzocht. Ten eerste creëren wij een *energie gap* (verboden zone) in grafeen, wat overeenkomt met een intrinsieke zero-gap halfgeleider, en vormen daarna quantum dot structuren op dit grafeen met gap. De transport eigenschappen van de opgesloten elektronen in de grafeen quantum dot worden vervolgens experimenteel bestudeerd op lage temperatuur. In een tweede project, fabriceerden we Josephson junctie structuren op grafeen met hoge H_{c2} supergeleider als reservoirs. Hier is het doel het onderzoek naar de interacties tussen de elektronen van het grafeen en de Cooper-paren van de supergeleider.

Twee benaderingen worden gebruikt om een energie gap in grafeen te creëren. Als eerste wordt een transport gap voorspeld voor bilayer (twee-laags) grafeen dat wordt onderworpen aan een elektrisch veld loodrecht op het vlak. Een loodrecht elektrisch veld zorgt voor asymmetrie tussen de bovenste en de onderste laag van bilayer grafeen, wat gelijkwaardig is aan een verschil in de on-site potentiaal voor de twee paren van de atomen binnen een eenheidscel. Als gevolg wordt een spectrale zone geïnduceerd. Experimenteel creëerden we de asymmetrie tussen de bovenste en de onderste laag met een duaal-gated transistor geometrie. Met een elektrisch veld, wordt een aanzienlijke toename van de weerstand van de geometrie waargenomen als de temperatuur wordt verlaagd, een indicatie voor de aanwezigheid van een isolerende toestand. Dit is in sterk contrast met het geval van monolaags grafeen, waar de weerstand veel lager en

temperatuur onafhankelijk is. Echter verdere studies wijzen erop dat het gedrag van de waargenomen isolerende toestand afwijkt van de verwachting voor een zuivere spectrale gap. Eerder vonden wij dat de wanorde een belangrijke rol speelt bij het verklaren van de waargenomen isolerende toestanden.

In een tweede benadering onderzoeken we de energie gap in een smalle grafeen nanoribbon, die is geëetst in een 2D grafeen vel. Een grafeen nanoribbon is een quasi-1D systeem waar de opsluiting kan leiden tot een spectrale gap. Experimenteel is een transport gap geconstateerd in grafeen nanoribbons, waar de geleiding 3 tot 4 orders van grote minder is in vergelijking met die geleiding buiten de gap. De oorzaak van het optreden van deze transport gap in een grafeen nanoribbon is momenteel van grote interesse in dit onderzoeksgebied.

Hoewel de reden van de gemeten transport gap in een grafeen nanoribbon iets onbegrijpbaar is, kunnen we toch gebruik maken van zijn eigenschappen om de elektronen op te sluiten. Een single quantum dot werd voor het eerst gerealiseerd in een grafeen nanoribbon tussen een smalle top gate en een back gate. Twee verschillende regimes, bipolair en unipolair, worden onderzocht. In het bipolaire regime hebben we elektrostatische opsluiting van de ladingsdragers door $p-n$ overgang aangetoond. In het unipolaire regime, blijken elektronen te worden beperkt als gevolg van grote wanorde.

Na het werk aan de top-gated single quantum dots, creëren wij vervolgens een dubbele quantum dot in een grafeen nanoribbon met behulp van drie top gates. Deze gates veranderen onafhankelijk het aantal elektronen in elke dot en stemmen de inter-dot koppeling af. In de zwak gekoppelde dubbele dot regime was voor het eerst transport door de aangeslagen toestanden in een grafeen dubbele quantum dot systeem geobserveerd.

Als aanvulling op onze interesse in opgeslotene elektronen hebben we ook onderzoek gedaan naar een aantal fundamentele aspecten van de vastestoffysica. Een interessant onderwerp is de studie van hybride systemen van een supergeleider en een halfgeleider in het quantum Hall regime. Het is wel bekend dat het elektrische transport op een supergeleider- normale geleider (SN) interface wordt beschreven door Andreev reflecties. In het quantum Hall regime wordt verwacht dat een elektronengolf in verspringende cirkelbanen reist meerdere Andreev reflecties langs de SN-interface ondergaat. Bij de uitgang van de SN-interface is de toestand door zowel elektronen als gaten gekarakteriseerd. Deze microscopische processen wijzigen de magnetische weerstand van het monster. Hoofdstuk 7 van dit proefschrift beschrijft een experiment waar we dit effect bestuderen aan een grafeen-supergeleider interface, met behulp van een Josephson junctie met een hoge H_{c2} supergeleider als contacten. Momenteel hebben wij Josephson stroom en daardoor Andreev reflecties bij een laag magnetisch veld aangetoond, evenals een quantum Hall-effect bij een hoog veld. Maar wij kunnen nog geen Andreev reflecties identificeren in het quantum Hall regime. Waarschijnlijk is de kans voor Andreev reflectie verlaagd in het hoog magnetisch veld regime door de hoge dichtheid van vortexen in de supergeleider. Verdere tests en analyses zijn aan de gang om dit probleem op te lossen.

Curriculum Vitae

Xing Lan LIU

19-10-1980 Born in Gansu, China.

Education

1995–1998 High School
Zhuanglang First High School, Gansu, China

1998–2002 Undergraduate in Materials Science and Engineering
Tsinghua University, Beijing, China

2004–2006 M. Sc. in physics (*cum laude*)
University of Groningen, Groningen, The Netherlands

2006 Ph.D. thesis *Quantum transport in graphene*
Delft University of Technology
under supervision of prof. dr. ir. L. M. K. Vandersypen

List of Publications

1. X. L. Liu, D. Hug, and L. M. K. Vandersypen,
Gate-defined graphene double quantum dot and excited state spectroscopy,
Nano Letters **10**, 1623 (2010)
2. X. L. Liu, J. B. Oostinga, A. F. Morpurgo, and L. M. K. Vandersypen,
Electrostatic confinement of electrons in graphene nanoribbons,
Phys. Rev. B **80**, 121407R (2009).
3. J. B. Oostinga, H. B. Heersche, X. L. Liu, A. F. Morpurgo, and L. M. K. Vandersypen,
Gate-induced insulating state in bilayer graphene devices,
Nature Materials **7**, 151 (2008).
4. Y. He, X. L. Liu, J. Y. Feng, and Q. L. Wu,
Effects of a Ge interlayer on the high-temperature behavior of NiSi films,
J. Appl. Phys. **96**, 6928 (2004)